Characterization of the Widescale Reversible Sliding Mechanism in California Red Abalone Nacre Structure

by

Hayden Price

A dissertation submitted to the Graduate Faculty of
Auburn University
in partial fulfillment of the
requirements for the Degree of
Doctor of Philosophy

Auburn University, Auburn, AL
December 10, 2022

Keywords: Nacre, Abalone,
Reversible Sliding, Deformation Mechanics

Approved by

Dr. Bart Prorok, Chair, Program Chair, Materials Engineering
Dr. Pengyu Chen, Associate Professor, Materials Engineering
Dr. Xiaoyuan Lou, Associate Professor, Materials Engineering
Dr. Jeffrey Suhling, Department Chair, Mechanical Engineering
Dr. Kyle Schulz, Assistant Professor, Mechanical Engineering

Abstract

The precise and ordered microstructures produced through the bottom-up process of self-assembly is a matter of much interest to many research teams, with many applications in the fields of engineering and technology. In the realm of biology, many organisms have developed some form of a self-assembly process to fit a physiological need over millions of years of evolution. One such example of this is the growth of the nacreous shell of the abalone. This research focuses on the abalone nacre and the mechanical properties of the structure.

Nacre, commonly referred to as "mother of pearl", makes up the iridescent inner portion of the abalone's shell and is an integral component. The nacre is comprised of nanoscale aragonite calcium carbonate tablets arranged in a "coin stack" manner. These tablets are grown through the self-assembly process known as biomineralization, in which a colloidal organic liquid is secreted from the epithelial cells of the abalone between their body and the outer wall of their shell. As the tablets grow, the organic liquid become the organic matrix that is interlocked throughout the entire tablet structure, creating a unique composite material with fascinating properties. These properties have been researched extensively, including the excellent strength provided by the material as well as the deformation mechanism of tablet sliding. But one aspect which has had little to no attention paid to it is the potential for a self-recovery mechanism that may be present in the nacre structure.

The goal of this work is to observe the presence of and characterize this widescale reversible sliding mechanism in the nacre structure of the California wild red abalone. To test for the presence of this mechanism, rectangular nacre beams were sectioned from shells of California red abalone. These nacre beams were polished along the cross-sectional side to reveal the tablet structure. The

beams were then placed into a scanning electron microscope and subjected to an *in situ* three-point bending experiments in an attempt to reveal this mechanism. Further analysis of this mechanism was performed by applying a nano scale speckle pattern and performing digital image correlation, to view the mechanism on a local level.

Table of Contents

List of Figures

List of Equations

Equation 1 – Flexural strain for the outermost surface of a rectangular cross section under three-point bending

$$\boldsymbol{\varepsilon = \frac{6\delta h}{L^2}}$$

ε – Maximum strain at the outer surface, nm/nm

δ – Mid-span deflection, nm

h – Thickness of the beam, nm

L – Support span, nm

Equation 2 – Strain at varying distances (x) from the neutral axis

$$\boldsymbol{\varepsilon_x = \varepsilon \frac{x}{d}}$$

ε_x – Flexural strain at varying distance from neutral axis, nm/nm

ε – Maximum strain at outer surface of the sample, nm/nm

x – Distance of tablet away from neutral axis, nm

d – Distance from neutral axis to outer surface, nm

Equation 3 – Line of best fit, generated from scatter plot data in **Figure 69**.

$$\boldsymbol{y = 0.314\,x + 1.2155}$$

y- Precent local strain (%)

x-Measured tablet gap (nm)

1. Introduction and Research Motivation

1.1 Self-assembly and biomineralization

The self-assembly mechanism is a bottom-up process which allows for the autonomous production of highly ordered structures with precision in the nanoscale range, which makes it an extremely attractive field for many researchers. The high degree of order allows for structures to be formed with a set of unique and exceptional properties that may even lend to a strengthening of a material if it is oriented in a specific way. The most vital components needed for a self-assembly process to occur are a suitable environment for the components to move freely in and a method or template to control the interactions necessary to promote the assembling of particles [1]. Many mechanisms exist which can facilitate self-assembly including the use of functional polymers [2,3], surface modification [4-6], external fields [7,8], and even DNA [9-11].

Using these mechanisms of self-assembly, researchers can produce highly ordered structures on the nanoscale to fit many applications. The degree of precision offered by self-assembly is much greater than what can be offered by artificial methods. There are even products which can be produced through self-assembly that are not achievable through artificial means. With greater control over the self-assembly process, even more precise structures can be produced on the nanoscale. This allows products that can be used in a wide variety of scientific fields by more and more researchers, from photovoltaics to drug delivery systems. Thus, knowledge of these mechanisms is crucial to their advancement.

The process of self-assembly is common throughout the biological world. Through millions and millions of years of evolution many organisms have developed a self-assembly process known as biomineralization, a crucial mechanism for their survival. The mechanism of biomineralization is how mammals and birds produce bone and how invertebrates produce their shells. It not only produces highly ordered, intricate structures, but biomineralization facilitates a self-assembly process in a non-toxic biological environment. One intriguing instance of biomineralization is the growth of nacre in the shell of the abalone facilitated by a self-produced colloidal organic liquid with a complex composition [12,13].

1.2 Abalone nacre

Nacre, commonly referred to as "mother of pearl", is an inorganic-organic composite material produced from the epithelial cells of several mollusks including oysters, mussels, and abalone. The iridescent appearance of nacre makes it very popular with people and is used in jewelry and decorations. But much more lies beneath the surface of this material. There are two types of nacre both of which are comprised of nanoscale calcium carbonate ($CaCO_3$) tablets but differ in both orientation and growth mechanism. The first is sheet nacre, in which the tablets are oriented and distributed randomly throughout the structure. The second is columnar nacre, in which the tablets are oriented very uniformly with fairly similar sizes [14]. Abalone nacre belongs in the class of columnar nacre, and it is due to the intriguing mechanical properties inherent to this structure that the abalone nacre has been heavily studied to attempt to better understand the mechanisms within and even mimicked to attain complex structures using different materials [15,16].

1.2.1 Mineral components of nacre

When viewing the shell of the abalone, it can visibly be divided into two separate parts. There is the rough exterior surface of the shell which faces the seawater (**Figure 1 A**), as well as the smooth, iridescent surface which faces the animal (**Figure 1 B**). While both parts of the shell are composed of calcium carbonate, the differ in their phase structure. The calcium carbonate in the exterior portion of the shell is in the stable trigonal calcite phase whereas the interior portion contains the metastable orthorhombic aragonite phase [17].

The abalone shell is recognized by many researchers in science and engineering due in part to the aragonite component of its shell. The inner portion of the shell is referred to as nacre, or "mother of pearl", and is made up of roughly 95wt% aragonite and 5wt% organic composition [18]. Normally, aragonite is a fairly brittle material. However, nacre has been found to have a toughness 1000 times greater than that of mineral aragonite [19].

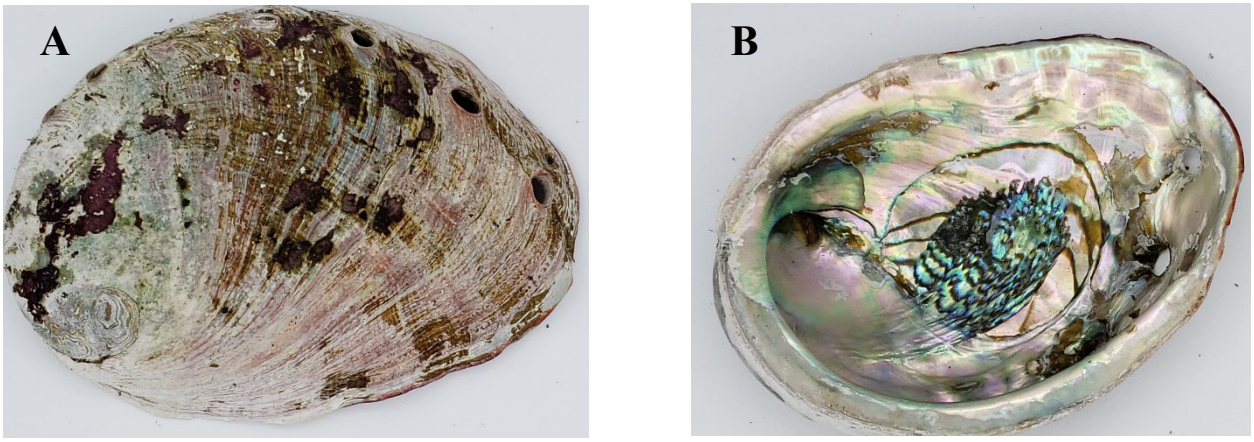

Figure 1: Camera images of California red abalone shell. (A) The exterior calcite portion of the abalone shell which faces the sea water. (B) The interior portion of the shell that faces the abalone's body and is completely coated in nacre.

The microstructure of nacre can be seen in SEM images taken of the cross-sectional side of a piece of cleaved abalone shell (**Figure 2**). The nanoscale aragonite tablets that make up the nacre are all of approximately equivalent size and interconnected by an organic thin film. The tablets are stacked in a columnar pattern with a crystal orientation that shows a preference towards the faster tablet growth rate [20,21]. The microstructure has been extensively explored and many different components have been discovered. Mineral bridges have been found to connect stacked tablets to one another in the vertical direction [14,18]. Another feature of abalone nacre that has been explored is the numerous nano-asperities that coat the surface of the tablets [19,22]. Both of these features are believed to contribute to the mechanical behavior of nacre in different ways.

1.2.2 Organic components of abalone nacre

While it may only make up 5wt% of the abalone nacre, the organic matrix is a vital component of the composite material. In the body of the abalone, there is a layer known as the mantle which makes contact directly with the nacre side of the shell. A colloidal organic liquid is produced by the epithelial cells of the mantle and is used as the environment in which nacre growth is promoted. When a layer of nacre tablet's growth is complete, the organic composition is remains within the structure forming an organic matrix. Mature nacre has been treated with a demineralizing agent to remove all but the organic matrix and TEM images were taken which reveals that the organic matrix forms a framework for the tablets [23].

The composition of the organic matrix has been heavily investigated and many components have been discovered, chief among them being chitin [18]. Chitin, consisting of 2-acetamido-2-deoxy-β-

D-glucose through a β (1→4) linkage, is a common type of natural structural polysaccharide and heteropolymer that is highly insoluble in water and most organic solvents and acts as a chemically stable component which helps to build structures in organisms [24]. The organic matrix an influencing factor in the nacre growth process. In the confined space between the mantle of the abalone and its shell, the organic composition in the colloidal liquid is thought to act as a template for the nacre and assist in the self-assembly process of its formation [25,26]. Aside from acting as the framework for the nacre, the organic matrix is also believed to make contributions to the mechanical properties of nacre in acting as a strengthening mechanism [22,27].

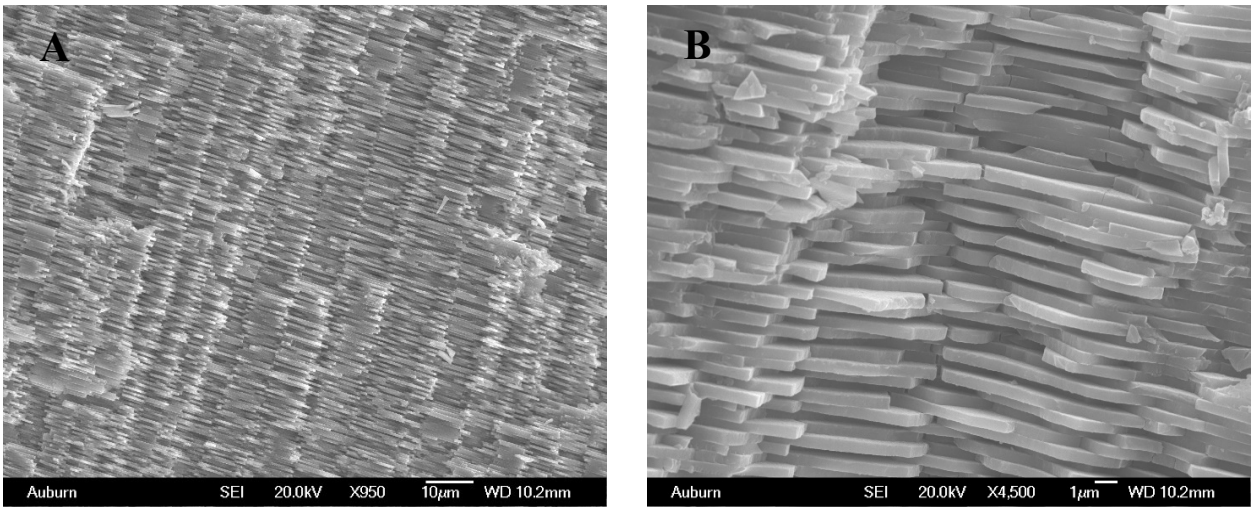

Figure 2: Nacre tablet structure (A) extended structure and (B) further magnified.

1.2.3 Growth of abalone nacre

Nacre's growth process has long been a point of interest and has been attempted to be interpreted and understood by many researchers. Knowledge of this process has led to a greater understanding of the self-assembly process involved in nacre growth and the relationship between the mineral and organic components. Since its first reporting [28], many images have been taken of the growth front in the "Christmas tree" pattern (**Figure 3**) to aide in understanding the growth steps. Several different assumptions have been developed for explaining this process [29,30]. The prevailing explanation for this process is that for each new layer of tablets, the aragonite first grows along the c-axis until they approach a height of 300~500 nm (the average thickness of aragonite tablets).

They then extend their growth in the a- and b-axes until they approach the growth front of a neighboring tablet. The "Christmas tree" images seem to support this as the tablets appear to grow vertically first, and then outwards from the nucleation site.

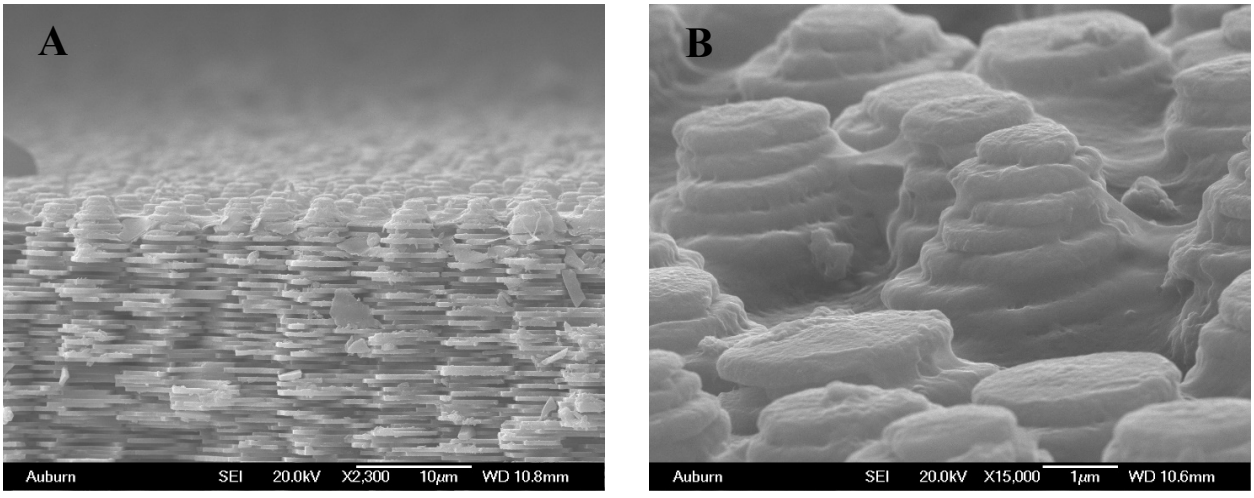

Figure 3: Images of the "Christmas Tree" structure of the nacre growth front.

1.3 Mechanical properties of abalone nacre

The soft bodied abalone has survived through millions of years of planetary change and evolution, protected from predators beneath its nacreous shell. Ever since it was first reported [31], the excellent mechanical properties of nacre have been the subject of numerous investigations. This has led the shell to undergo various types of mechanical property testing such as tensile testing [32], 3-point bending [33], 4-point bending [34], nanoindentation testing [35], compression testing [36], and shear testing [37]. The high toughness that the nacre exhibits is phenomenal considering that it is a composite material comprised mostly of a brittle material.

As previously mentioned, the essential component to explaining the fantastic mechanical behavior of the abalone nacre is its precise and unique nanostructure. The common consensus on the deformation mechanism which occurs in abalone nacre is referred to as tablet sliding. As the name suggests, the tablets of the nacre structure slide apart from one another leaving gaps in between. When the strain is increased on the tablet structure, more and more tablets in a column will begin to slide, forming discrete dilation bands along the column. Multiple dilation bands can form throughout the nacre structure, blunting any cracks that form in the outer aragonite structure of the shell. The exact nature of this mechanism is the center of much debate and research in order to determine the true cause of the increase in strength.

There are several factors that are believed to aide and facilitate the sliding mechanism in abalone nacre including the presence of nano-asperities on the surface of tablets, the existence of mineral bridges between adjunct tablets, the level of hydration of the organic matrix throughout the tablet structure, and even the waviness of the tablets [38]. However, the exact nature and influence of these factors remains a point of debate due in part to the difficulty of observing the deformation process

at its immediate onset. While some researchers believe that nano-asperities have an effect on the mechanical properties of the nacre structure [39], others have cast doubt on its effect through modeling and analysis [40]. This continued debate over the origin and nature of the deformation mechanism in nacre is precisely why more research is needed. As the knowledge of nacre's behavior and how its deformation mechanism occurs advances, so too does the development and enhancement of complex artificial materials based on its remarkable structure and properties.

One aspect of the deformation mechanism that has received little to no attention is the potential presence of an elastic recovery system. The organic matrix that is interwoven throughout the nacre tablet structure consists of biopolymers, and as such should behave in an elastic manner when a force is applied to it. Some have theorized that if the strain in the structure were to be below some critical value, then the biopolymer would assist in bringing the separated tablets back together through a strain relaxation and refolding of the biopolymer. Unfortunately, little to no research has been devoted to exploring this feature of the deformation mechanism.

Through a literature review, only two instances of research mentioning the potential of reversible sliding could be found. The first was the work of Sumitomo et al.[41] in which the team tested rectangular samples of nacre with a notch pre-cut into the cross-sectional portion of the sample. Deformations were performed inside a transmission electron microscope (TEM) so as to observe the effects of the deformation on the organic matrix. During the deformation, the organic matrix was shown to stretch and fail. After failure, the ligaments of the biopolymer recoiled in a viscoelastic pattern. In **Figure 4**, the ligaments of the biopolymer can be seen recoiling and thickening as they reform after they fracture from one another. This was further explored in an atomic-force microscope (AFM). Inside the AFM, as the sample was deformed, a "sawtooth" shaped force extension plot formed, demonstrating the presence of sequential energy absorbing

events. These observations have led to the hypothesis that there may be the presence of reversible deformation in the matrix, acting as a strengthening mechanism in the overall nacre structure.

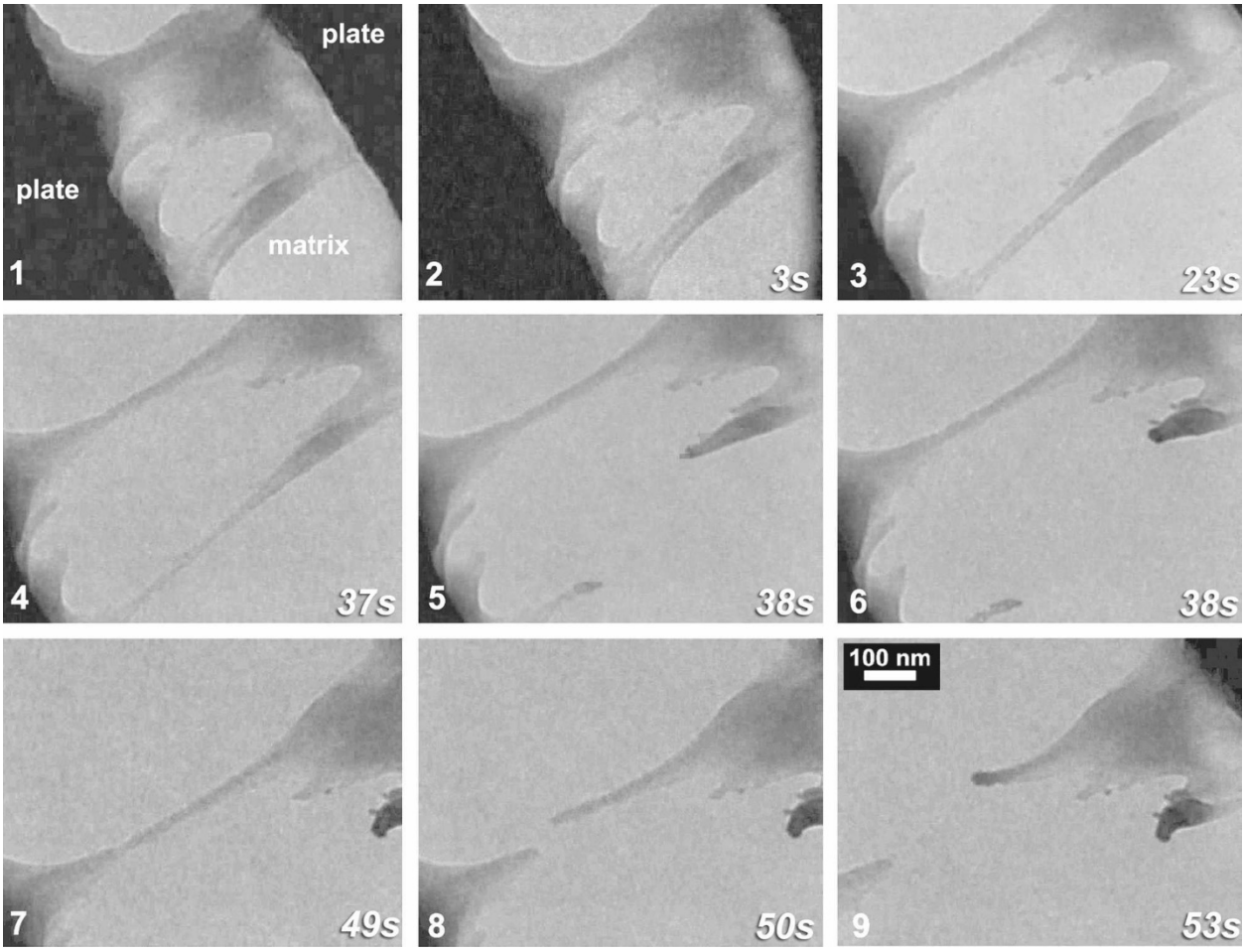

Figure 4: TEM images of *in situ* deformation of organic matrix. The sequential images show the separation of the tablets, deformation of the matrix, its failure, and its recoiling. While recoiling the tips thicken as they reform.

Espinosa et al.[42] also happened upon reversible sliding during experiments with the abalone nacre structure. The team was testing pre-notched nacre bars under three-point bending conditions. AFM images of the samples were taken before loading, during loading, and failure after. The images were taken inside the failure process zone, roughly 1 mm away from the pre-notch. The images

were then put through post processing Digital Image Correlation (DIC) in order to see the effects of the crack as it passed the imaging area. As the crack initiates and approaches the scan area in **Figure 5**, the tablets can be seen sliding apart from one another as shown by the increasing darkness of the DIC image overlayed on the AFM images. When the crack passes the scanning area, the coloration of the DIC image begins to lighten. This would appear to indicate that a partial reversal of the sliding occurred in the scanning area of the nacre structure. While this was observed, not much more attention was paid to this as it was not the main goal of the paper at the time.

This research will seek to explore the possibility of reversible sliding further through mechanical testing, specifically through the use of three-point bend testing. This testing method was chosen for its ease of use and ability to control the deformation process within a reasonable degree. As the tablets are on the nanoscale, testing was performed *in-situ* within the scanning electron microscope (SEM), allowing for dilation bands of tablet sliding to be discovered, tracked, and imaged as they evolve through the bending process.

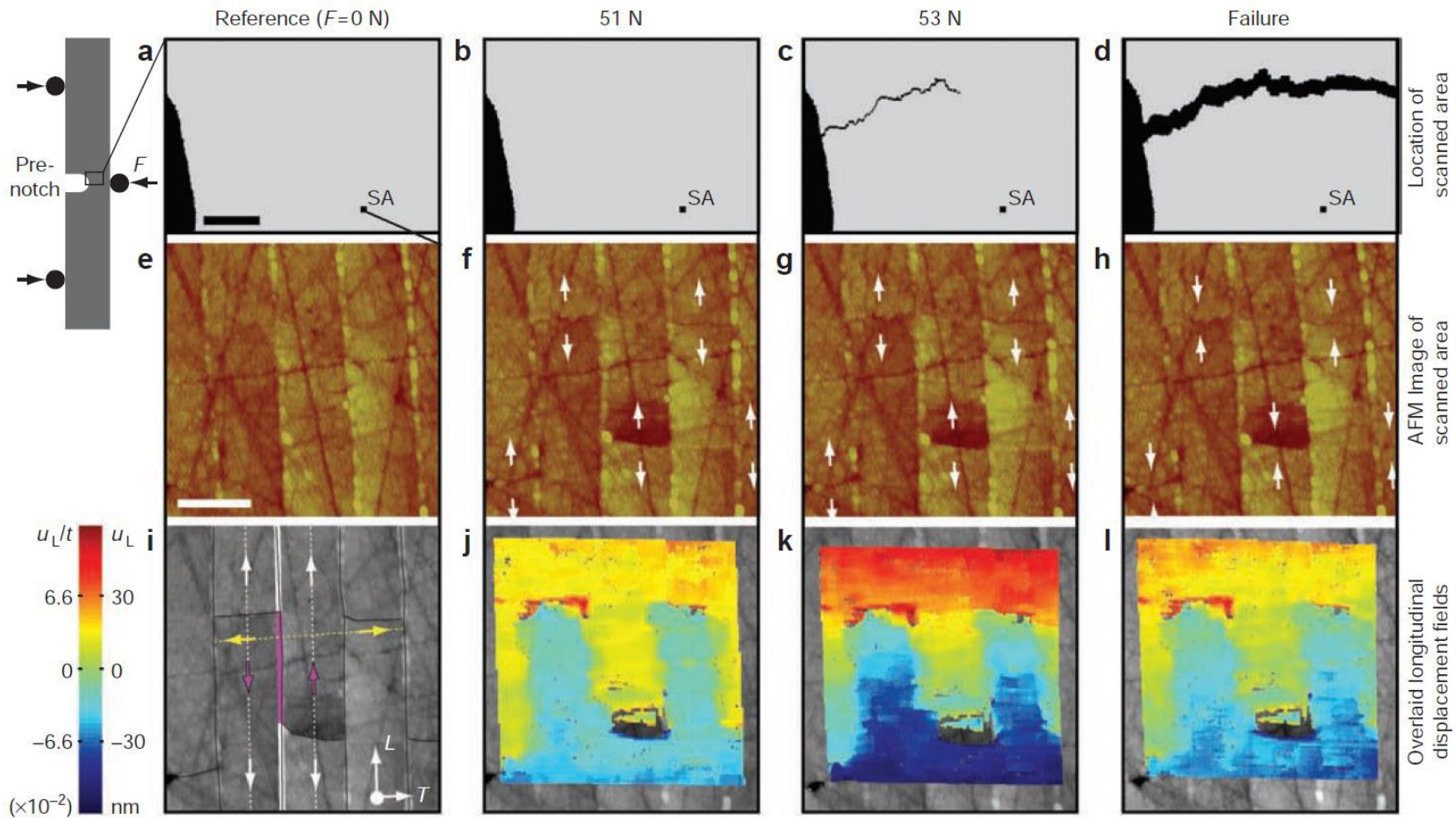

Figure 5: *In situ* AFM fracture test of abalone nacre. (a-d) Images of the scanned area relative to the pre-notch and subsequent crack. (e-h) AFM images of the nacre structure before deformation (e), during deformation (f), as the crack approaches (g), and after the crack passes (h). (i-j) The same AFM images (e-h) with the DIC longitudinal displacement overlaid.

2. Materials and methods

2.1 Materials

The main material that was utilized for these experiments were sample beams consisting of the nacre structure sectioned and removed from the shells of the California Wild Red Abalone, *Haliotis Rufescens*. The shells of the abalone were procured from the The Abalone Farm, Inc. in Cayucos, California. The shells of the abalone were roughly 15 cm in length and 12 cm in width. The outer portions of these shell were roughly removed, and section beams were made from these shells to be used for experimental testing of the nacre structure.

2.2 Sample Preparation Methods

To prepare the samples, first the abalone shells were thoroughly dried for at least seven days. Then, portions of the shell were cleaved from it in its entirety using a Dremel® 4000 tool with a diamond tip cutoff wheel (**Figure 6**). The section removed from the shell was roughly a 2 cm x 2 cm square (**Figure 7 A**). At this point the section still had the outer portion of the shell as well as a slight curvature to it. The section was then taken to a 320-grit grinding pad on a Buehler Supermet grinding stage (**Figure 8 A**) to rapidly remove the outer portion so that only the nacreous portion of the shell is left. This section is then taken to a 600-grit grinding pad using a Leco VP-160 grinding stage, (**Figure 8 B**) until it has reached a desired thickness of ~350μm. The Dremel® tool

was again utilized to section off beams for further grinding and polishing to be tested later (**Figure 7 B-C**).

Figure 6: Dremel 4000 tool.

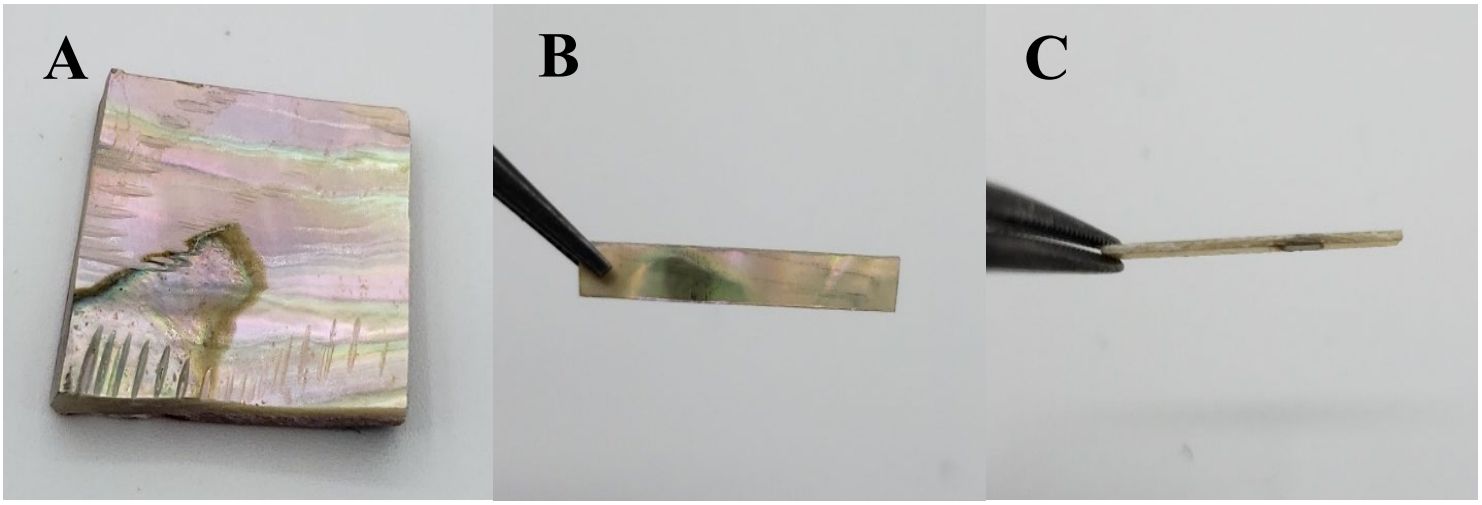

Figure 7: (A) A 2cm x 2cm square of the abalone shell sectioned off using the Dremel tool. (B) An unprocessed nacre beam viewed from the front, facing the abalone body. (C) Unprocessed nacre beam viewed from cross-sectional side.

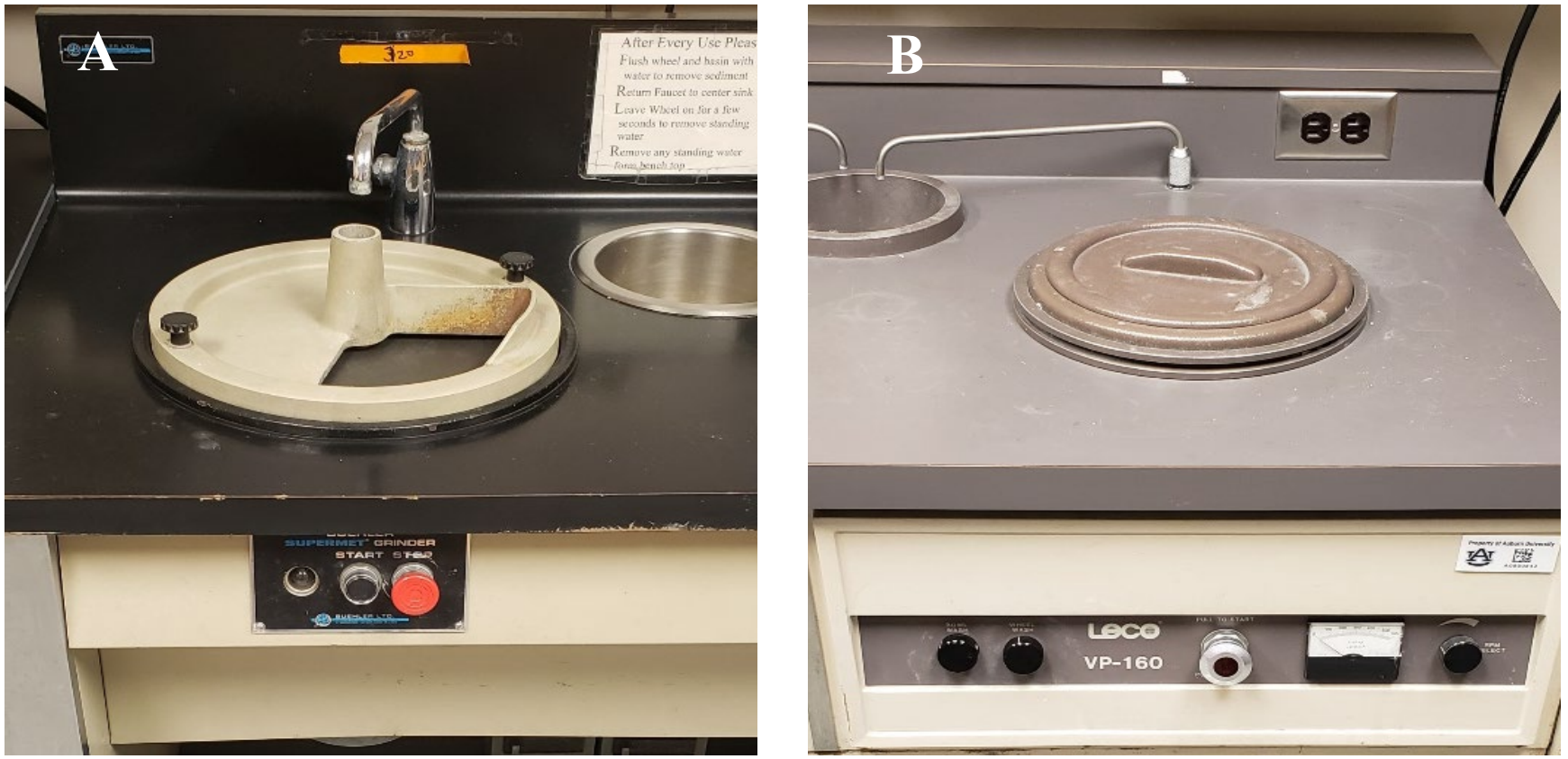

Figure 8: (A) Buehler Supermet grinder. (B) Leco VP-160 grinding stage.

A modified polishing stage (**Figure 9**) was designed and printed using 316L stainless steel for ease-of-use during the polishing process as the beams were fairly small by this time. The stage consists of a hollowed-out puck with a groove and a steel bar. The beam was placed in between the inner wall of the groove and the metal bar, with a portion of the cross-sectional side of the beam exposed. Two set screws were tightened to hold the bar and beam in place to allow for additional processing without damaging both the polishing systems and the beams. The stage and beam were printed using Concept Laser MLab 100R additive manufacturing machine (**Figure 10**).

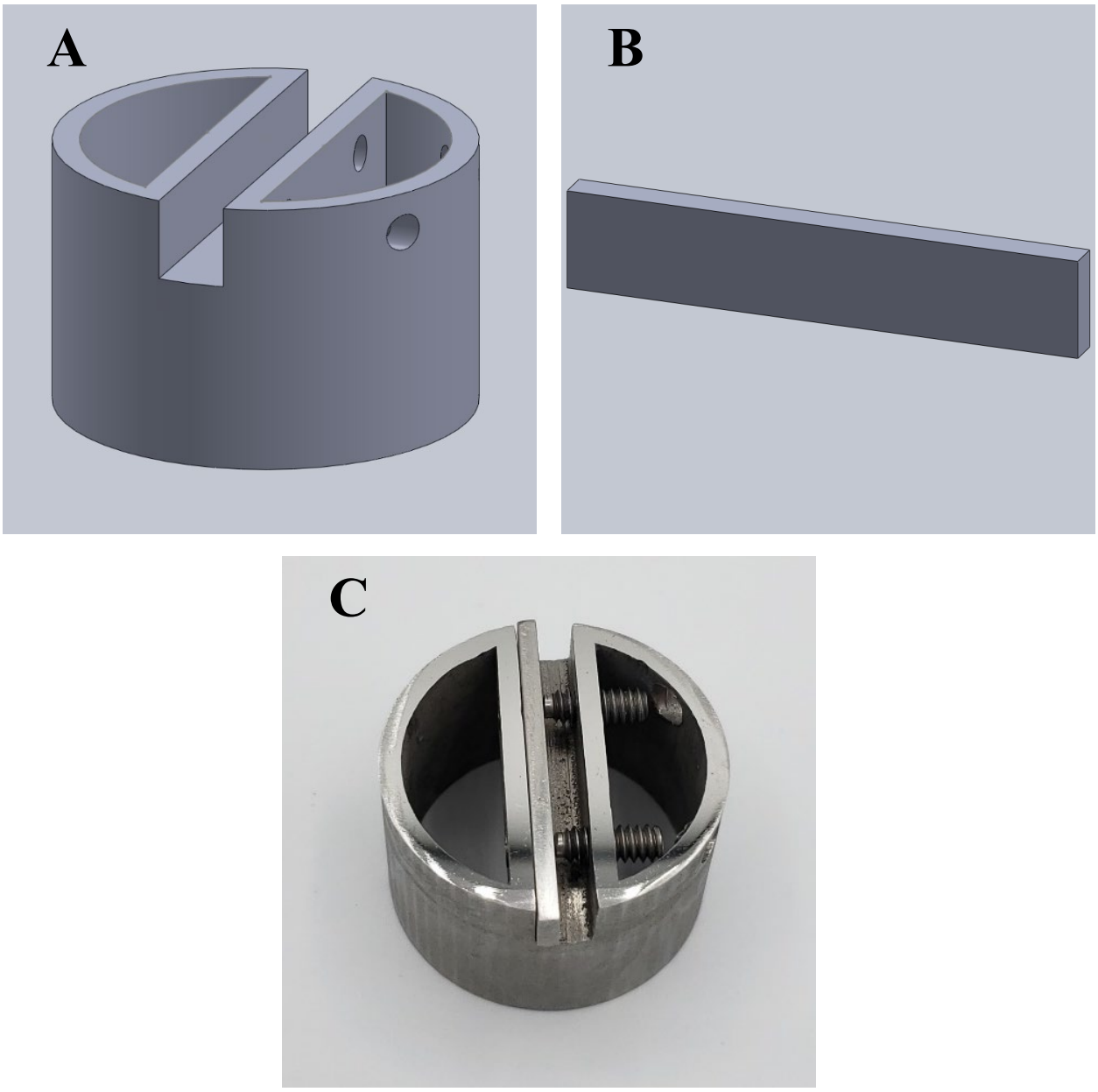

Figure 9: (A) Part design for a mounting stage used to polish the cross-sectional side of the nacre beam sample. (B). Part design for a simple bar used to hold the nacre beam to the inner wall of the mounting stage. (C) As printed mounting stage using 316 stainless steel metal powder in Concept Laser MLab 100R additive manufacturing machine.

Figure 10: Concept Laser MLab 100R additive manufacturing machine.

To begin the polishing procedure, the beams were ground along the cross-sectional side using increasing grit sizes starting a 400-grit, continuing to 600-grit, and finally moving on to 800-grit. This was again performed using the Leco VP-160 grinding stage (**Figure 8 B**). The beams then received a final grinding/initial polish stage with a 30-micron diamond grinding pad with a water rinse. The 30-micron diamond grinding pad was secured on a Leco SS-200 polishing stage (**Figure 11 A**) for ease of use. Following this, the beams underwent a cleaning process. The beam was rinsed with water, and then simultaneously dried and wiped using an air dryer and a KimTek wipe, respectfully. The beam was then rinsed with acetone to insure any and all polishing medium and debris were removed from the surface of the beam. The beams were again dried and wiped simultaneously. The beams were inspected under optical microscope using a Mitutoyo optical microscope (**Figure 12 C**) to confirm the grinding process and initial polishing had been performed appropriately.

Next, the beams were polished on Struers RotoPol-11 polishing stage (**Figure 11 B**) using a GOLD PAD polishing pad with a 6 μm diamond suspension, both purchased from Pace Technologies, for 5 minutes. Following the polishing, the sample beam was again rinsed and dried and wiped using the same method as previously stated and inspected under optical microscopy. The sample beam was then polished again on a separate Struers RotoPol-11 with a new GOLD PAD, this time using a 1 μm diamond suspension for 5 minutes. Again, the sample beam was rinsed, dried, and wiped as previously indicated and inspected under optical microscopy.

Lastly, final polishing was performed on a Leco SS-200 polishing stage using a MICROPAD polishing cloth with a 0.06 μm colloidal silica suspension, both purchased from Pace Technologies, for 5 minutes. Following the 5 minutes of polishing, the water was turned on and the sample beam was run on the polishing pad for 1 minute to remove any and all excess polishing

medium and debris. The sample beam was then rinsed, dried, and wiped as previously stated, and inspected once more under optical microscopy. Once the grinding and polishing was complete, the sample beams were complete and at their final dimensions of 13 mm long, 1 mm high, and ~350 μm thick.

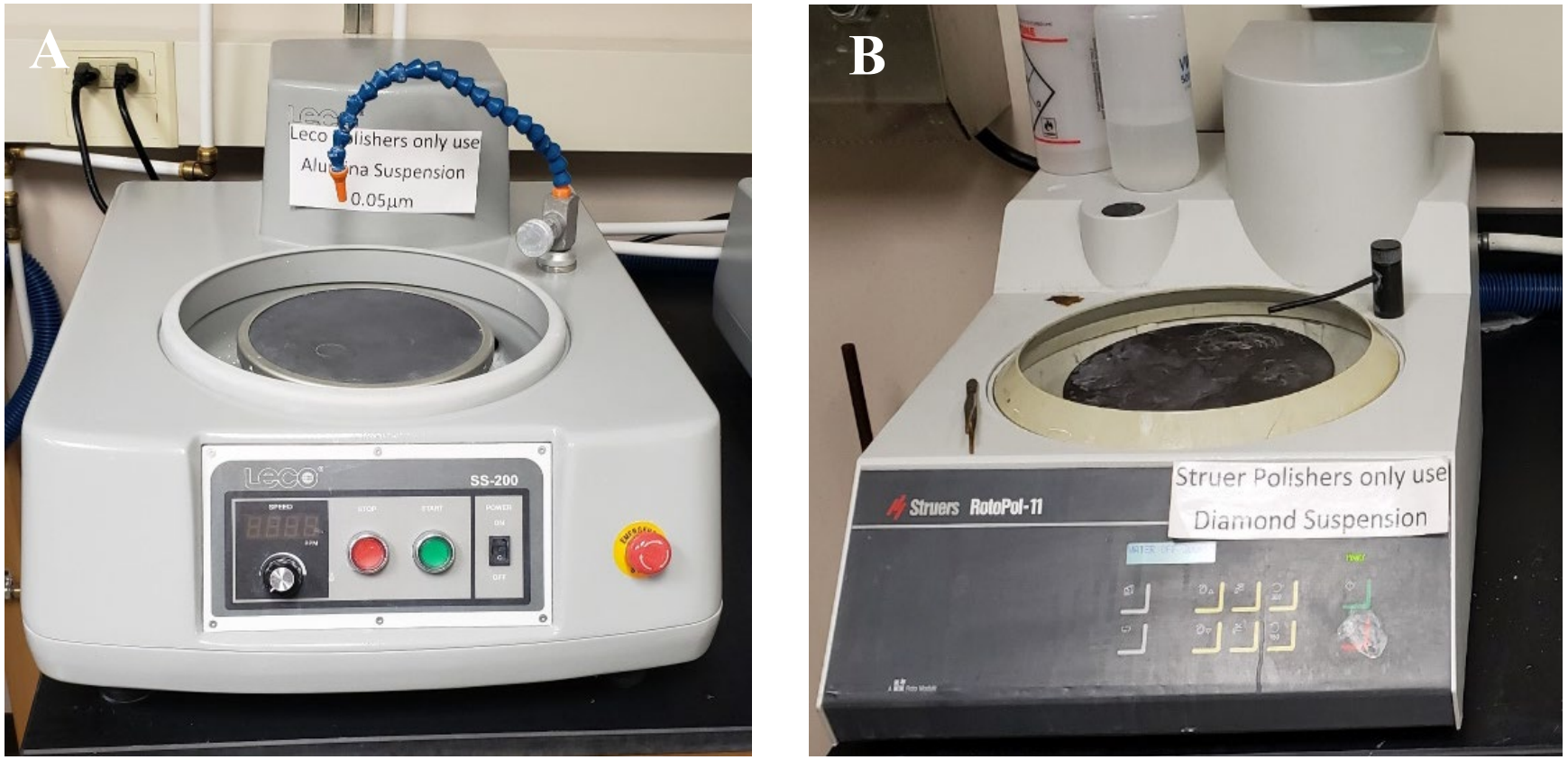

Figure 11: (A) Leco SS-200 polishing stage. (B). Struers RotoPol-11 polishing stage.

2.3 Characterization Methods

In characterizing the nacre sample beams, one of the first methods used was optical microscopy. During the polishing process, a Mitutoyo optical microscope (**Figure 12 C**) was utilized to determine the effectiveness of the polishing process. The ideal result of each successive polishing stage was to remove debris and scratches from the surface of the sample beam in order to arrive at a mirror-like surface that would reveal the nacre structure for further characterization and testing. Following each of the polishing stages, the samples were inspected for a reduction in the degree of scratches on the surface. If the degree of scratches had not been reduced during any particular polishing stage, that stage was then repeated in full and inspected under optical microscopy once again. If the scratches were reduced, the next polishing stage would proceed. Upon completion of the final polishing stage, the sample was allowed to thoroughly dry for 24 hours before continuing to the next stage of characterization.

Due to the nacre structure being on the nanoscopic scale, the tablet structure cannot be viewed through optical microscopy, as it lacks the amount of resolution necessary for this. In order for the nacre tablet structure to be imaged, a more powerful imaging tool such as a scanning electron microscope (SEM) is necessary. But before the nacre beam samples can be imaged in this way, a protective and conductive material layer must be applied to the cross section of the sample beam to aid in imaging in the SEM. To perform this, the sample beams were placed inside of a Pelco SC-6 sputter coater with a gold (Au) target (**Figure 12 B**). The beams were placed with the polished cross section facing the gold target. The sputter coater chamber is then evacuated and placed under a vacuum. Once a minimum working pressure is achieved, the chamber is then filled with a small amount of Argon gas, to clear out the rest of the air and to act as conduit for

transferring the gold onto the surface of the sample. After bringing the chamber back to the working pressure, a charge is applied to the gold target, exciting the gold and with the aid of the Argon gas, allows the gold to travel to the surface of the sample, coating the sample in a thin film of gold.

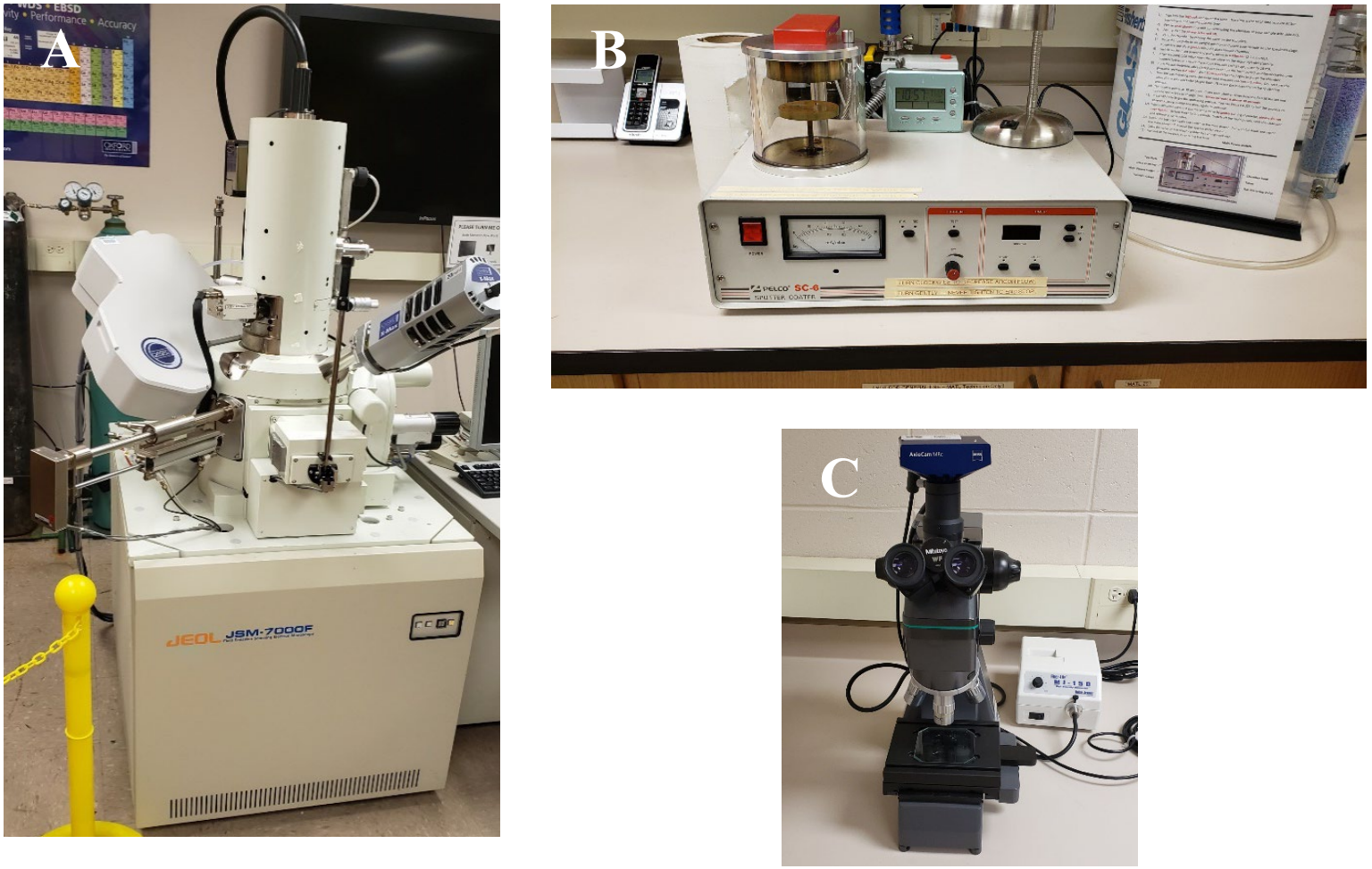

Figure 12: (A) JEOL JSM-7000F field emission electron microscope. (B) Pelco SC-6 sputter coater with gold (Au) target. (C) Mitutoyo optical microscope.

Once the sample beams had been coated in a thin film of gold, the beams could then be placed in a scanning electron microscope for additional characterization and testing. The SEM used for these purposes was the JEOL JSM-7000F field emission electron microscope (**Figure 12 A**) with and operating pressure of 7.74 e^{-4} Torr. The imaging was performed at 20 keV to ensure maximum quality and information could be gathered from these images. The freshly coated sample beams were placed inside the SEM to inspect the results of the polishing process. Once placed into the SEM and operating pressure had been achieved, the samples were inspected for quality of polishing to see if the polishing process had revealed the nacre tablet structure appropriately so that experiments on the nacre sample could be performed.

Three criteria were considered when inspecting these samples to determine if they were viable for experimentation. The first was the removal of debris, scratches, and medium on the surface of the sample beam. The ideal samples would be free of any large-scale scratches and debris caused by the grinding and polishing process as well as any medium that was used during these processes that would obscure the tablet structure of the nacre sample. Knowing that removal of all debris would be near impossible, and that some debris may be helpful in identifying certain areas in the sample at such a small scale, this criteria had the most amount of leniency baked into it. The second criteria was the angle of the tablets with respect to the outer surface of the sample beam. The ideal sample would have a nacre tablet structured that was aligned parallel to the sample beams outer surface. If the angle of the tablets was too far off from parallel, this may affect any tests performed on the nacre structure too greatly. Lastly, sample beams were then inspected for any large-scale defects in the nacre structure such as preformed cracks, holes in the architecture, or anything else which may cause a loss in integrity of the sample beam.

2.4 Digital Image Correlation Software

There are several DIC software capable of performing the characterization. Some are open sourced and easily accessed, however require a knowledge of the source code and the programing language in which it is written. Then there are all-in-one software packages that are easy to use, but the cost of entry for this software may be prohibitive for some. The pros and cons of these different software options were weighed and eventually the software that was selected for continuing with this characterization method is the digital image correlating software from GOM Correlate.

The GOM Correlate software (**Figure *13***) is an all-in-one DIC software that comes with everything necessary to preform digital image correlation in a free to use version. GOM Correlate also provides a set of helpful tutorials to learn how to use the software. This made it a great selection for my work with the abalone nacre.

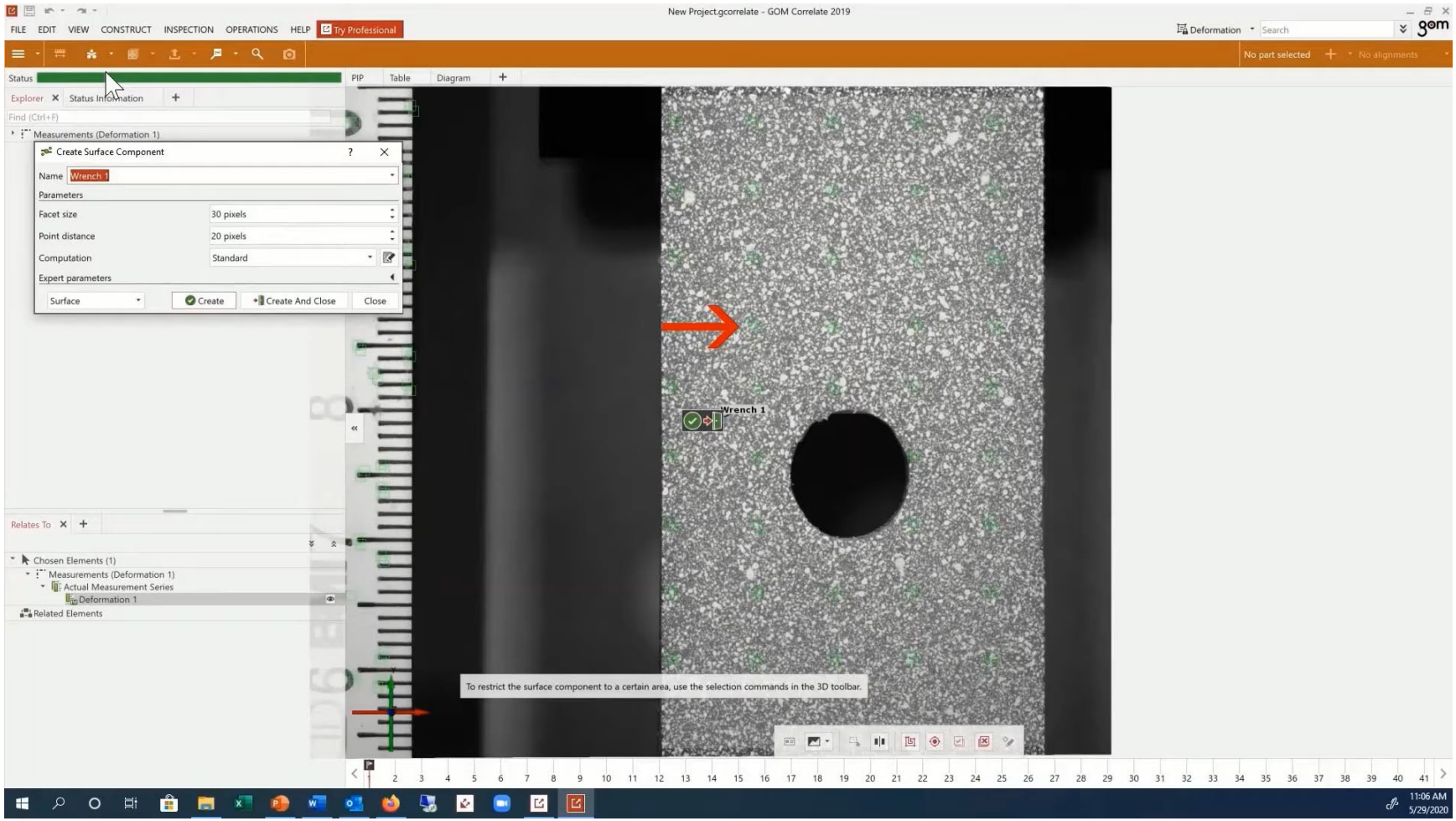

Figure 13: Depiction of a set of deformation images undergoing surface component production using the GOM Correlate software. [51]

GOM Correlate's DIC software relies on the stochastic pattern method, in which the software analyzes the random speckle pattern on the surface of the sample image at some reference stage and compares the stochastic pattern on subsequent stage images as it undergoes some form of deformation [47]. This comparison of the stochastic pattern on the subsequent deformation images allows for all manner of characterization information to be obtained.

To begin with the software, first a collection of deformation images of a sample with a sufficient speckle pattern applied must be obtained. These images are then imported into the software to allow for the inspection process. Next, a type of surface component must be created on the surface of the images. The GOM Correlate software will find an array of square facets on the surface of the image and place them in areas where there is a sufficient amount of speckling that matches the stochastic pattern method. The software will then place two overlapping facets at a location where it has deemed a sufficient pattern has been applied.

The facet size can be altered with the selection tool during the surface component formation step in the software. When a larger facet size is selected the amount of computational time is increased drastically. There is also a decrease in the ability to detect the local effects on the surface of the sample. However, the accuracy of performing coordinate measurements is increased. The opposite is true for smaller facet sizes. The computational time for producing the surface component is decreased, and the component is better at detecting the effects on the local level of the sample. But the coordinate measuring accuracy is sacrificed for this. A balance of these features must be achieved, tested, and accessed in order to discern the information needed for each individual sample set.

The next asset that can be controlled by selection tool during the surface component formation is the point distance. The point distance is a measurement of the distance placed between the center points of a set of adjacent facets. One of the first things that this affects is the point density of the surface component. When the point distance is smaller, there is a larger measurement point density providing a higher spatial resolution. A larger point distance will decrease both the point density and the spatial resolution. This change in spatial resolution effects the ability to detect the local effects of the deformation. With smaller point distance and higher spatial resolution, a greater view of the local effects of deformation become visible. Subsequently, the larger point distance and lower spatial resolution create a worse view of these local effects. The smaller point distance also causes an increase in the computational time and vice versa for the larger point distance. The software recommends that for accurate and useful computation and representation of the measuring results, the point distance should be set anywhere between 20% and at a maximum 50% of the selected facet size. Again, a balance of these features must be achieved, tested, and accessed in order to discern the information needed for each individual sample set.

After these variables are selected and set to a desirable level, the surface component can be formed on the surface of the sample. The measurements created from these surface components tracking the stochastic pattern on the samples can allow for many different evaluations to be performed on the set of deformation images. These include both strain and strain rate in multiple directions, displacement of the surface, and even the velocity of the deformation if you have the given time frame in which the deformation was taking part in. But as stated previously, for this software to work properly, an appropriate speckle pattern must first be placed on the surface of the sample, as without it there will be nothing for the software to track.

2.5 Experimental Testing Methods

2.5.1 Selection of Deformation Testing Method

The abalone nacre architecture is a complex composite microstructure, the analysis of which can be difficult due in part to this complex nature. When attempting to narrow down the most appropriate method to allow for large scale tablet sliding to be imaged, several testing methods were considered and the pros and cons of each were assessed and measured to determine which method would be most effective in providing a way of viewing the wide scale reversible sliding necessary for these experiments. One of the first methods considered was to use a simple tensile testing method.

The tensile testing method was the method of choice for many research teams when working with the abalone nacre. This method was used in many previous experiments, including experiments to initially calculate the strength of the nacre architecture. While the test method is a standard throughout the world of mechanical testing of materials, several draw backs presented themselves when evaluating this testing method. Firstly, this method was used to bring the samples to its failure point on multiple occasions but hadn't previously been used to evaluate the nacre architecture. For this method to work, the tensile testing rig would need to be very precise, operating on the order of microns of strain applied to the sample. This precision is needed as to allow wide scale sliding to be located without bringing the architecture to a failure point, thus preventing imaging from occurring.

Secondly, the tablet structure of the nacre architecture is on the order of hundreds of nanometers in size. The gaps that form during the sliding process are on the order of tens of nanometers. The only way to properly image these gaps as they form in the architecture is inside a Scanning Electron

Microscope (SEM). The commercially available tensile testing apparatus that could be purchased that would allow for micron level precision while still allowing for *in situ* experimentation within the SEM came with estimated quotes of tens of thousands of dollars, making this method of testing with these instruments slightly cost prohibitive.

Lastly, one of the major drawbacks to this method is the shear immensity of the area that would need to be searched on this scale. For the tensile testing method, nacre sample bars would be made on the scale of several millimeters in dimensions. As stated earlier, both the gaps formed between them, and the nacre tablets themselves are on the order of tens and hundreds of nanometers respectively. Due to the stochastic nature of the nacre architecture, during the tensile testing process, the tablets that begin to slide first could potentially be found anywhere along the width and length of the nacre samples. Searching for these gaps would be tantamount to searching for a needle in a haystack the size of a football field. The enormous amount of time that would be expended in the scanning of these samples at this scale along with the cost of operation of an SEM for that amount of time would again be operationally prohibitive. Given the cost of operation, in the cost of the tensile testing rig needed to perform these tests and the cost of operating an SEM for an extensive amount of time, the precision of the instruments needed to perform these tests, and the immense area that would need to be scanned and the time necessary to preform said scanning, the tensile testing method was deemed inefficient for the purposes of these experiments.

The second testing method that was evaluated was a simple four-point bend mechanical testing method. With the four-point mechanical bending method, the amount of area needed to be searched for the purpose of witnessing and imaging wide scale reversible sliding in the nacre architecture is reduced dramatically when compared to the tensile testing method. As opposed to searching the entire width and length of the abalone nacre sample, the location of the tablet sliding would first

occur in the outer most free surface of the sample beam. At the outer most surface of the sample beam between the two loading pins, the stress and strains applied to the beam are at their greatest, so as the beam is bent further and further this will be the area where sliding will likely occur first. There were a few draw backs to this method, however, that still made other methods a bit more desirable.

One of these draw backs was again the monetary factor as commercially available four-point bending rigs with both the precision necessary for minute bending to be performed on the sample sand the ability to be placed and operated within the scanning electron microscope were vastly expensive also reaching upwards of tens of thousands of dollars. There were attempts at designing a four-point bending apparatus that would be more cost effective and allow for precise motion to still be performed. These efforts ran into some difficulties when attempting to design a mechanism that would allow for forward actuation of the two central bollards (or pins) that didn't cause slipping between the screw or actuator or that didn't cause the component acting as the pins to rotate in early tests.

Another drawback was still the area in which the search for the wide scale reversible sliding could be occurring. As stated earlier, the search area in question for the four-point bending method would be the outer most free surface of the sample beam between the two loading pins. Depending on the specific method of four-point bending that was chosen, the span between the loading pins is between one third and one half that of the support span. When working on designs for the four-point bending apparatus that would be cost effective and functional inside the SEM, support spans for the apparatus were between 15 and 20 millimeters in length. These support spans still led to several millimeters of length to be scanned in search of wide scale reversible sliding. While still less than the amount of area that would be required to search for the tensile testing method, the

search area for the four-point bending method would still be fairly extensive and would require a substantial amount of time in order to search for the initial instances of tablet sliding. This expansive search area coupled with the design difficulties and cost of operations made this method slightly less desirable than the final option that was explored.

The third and final testing method that was explored was three-point bend mechanical testing. This method simplified many of the drawbacks that were presented with both the four-point bending and tensile testing methods. As with the other two methods, commercially available testing apparatuses that could be purchased were upwards of tens of thousands of dollars. Alternatively, a more cost-effective testing apparatus could be designed that would allow for testing of the nacre architecture with the precision necessary to allow for minute changes in load being applied to the samples while the testing apparatus can be placed within the SEM. **Figure 14 A** shows a schematic of the three-point bend testing methodology. In this method, the sample specimen is loaded onto a support span consisting of two pins or rollers. A third pin or roller is then used to apply the force to the sample beam, causing the bending of the beam. The simple nature of this testing method allows for a low-cost alternative to be constructed that would allow for effective testing of the nacre architecture.

The other major benefit to this testing method was the significant reduction in the amount of area needed to be searched for wide scale reversible sliding. With the previous methods the amount of area that needed to be searched for the first signs of tablet sliding occurring during testing was anywhere between a few millimeters and the entire width and length of the nacre beam sample, both of which would take a substantial amount of time to perform these scans. Alternatively, with the three-point bending test method, the area in which the search for wide scale reversible sliding would occur would be at the apex of the loading on the nacre sample beam at the outer free surface.

Unlike with the four-point bending test method where the maximum load applied would be even across the entire span of the loading pins, the location of the maximum strain for three-point bending occurs at the center of the sample beam along the outer free surface opposite that of the side on which the loading pin sits, as this is the point of greatest tension as seen in **Figure 14 B**. However, given the stochastic nature of the nacre architecture, the tablets which may begin sliding initially may not be at the exact center of the beam, so the area of search would still need to be somewhere within a few hundred microns on either side of the loading pin. Even with this fact, the search area is still significantly smaller than that of the four-point bending of the tensile testing methods. With the significantly reduced search area and the ability to design a simple and cost-effective testing apparatus with advanced precision that would allow *in situ* testing to be performed within the SEM.

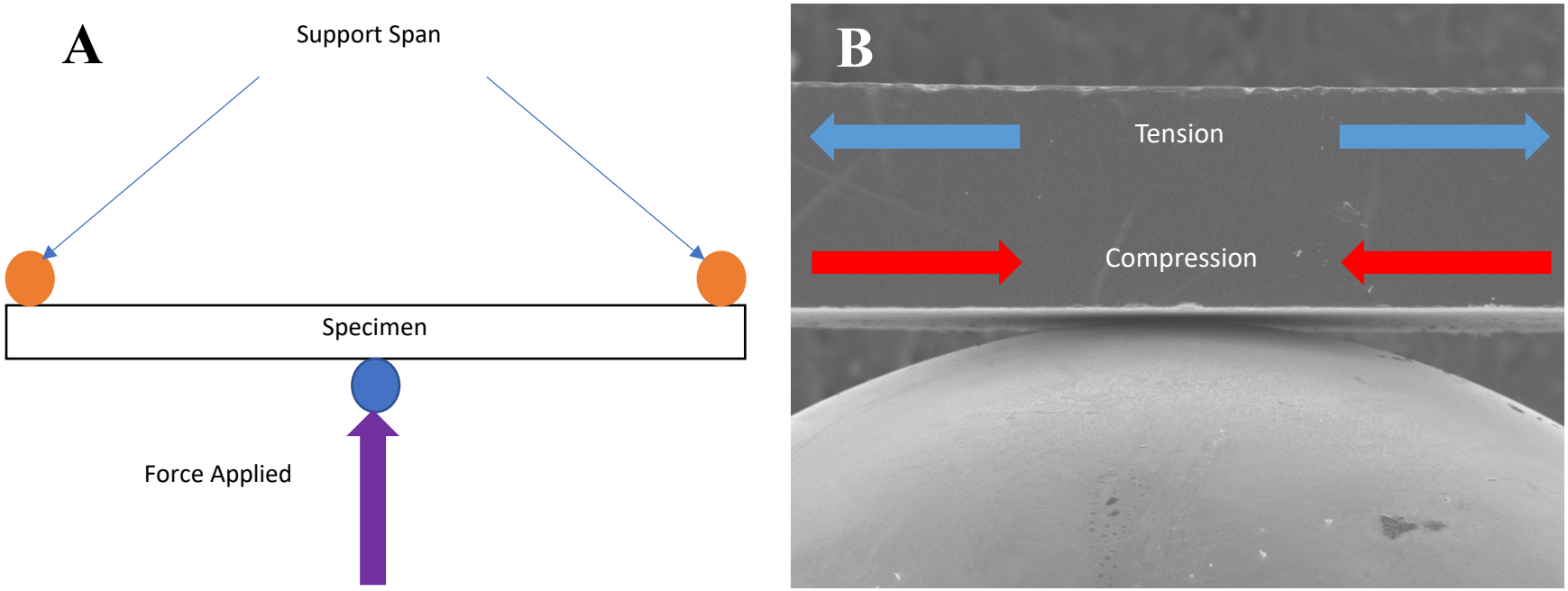

Figure 14: (A) A schematic of the three-point bend beam deflection technique. (B) Image of sample beam in contact with loading pin in a three-point bending mechanism.

2.5.2 Development of in situ Three-Point Bend Testing Method

In order to perform the *in situ* the testing, a proper testing apparatus must be procured in order that would allow for this test to be performed with in the SEM. There do exist some commercially available three-point bending stages that can be purchased for use within the SEM that would address these concerns. These three-point bending stages are capable of performing *in situ* experiments within the SEM while withstanding the ultra-high vacuum conditions that are present inside the SEM. The stages are also capable of applying bending to sample beams at minute increments with micron level precision. These loads would be applied through linear actuation to prevent any slipping between the loading pin and the sample beam, as well as prevent the loading pin from scratching or cutting the sample beam. They also have a whole host of analytical tools for measuring the load applied to the sample, the stress and strain, and can perform several different testing methods including anything from cyclic loading and complete sample failure. The downside to these stages is that they are not cost effective and reach upwards of twenty-five thousand dollars in price. This price range made this stage an almost immediate rejection from consideration. However, the extreme price point led to considering the potential of designing a more cost-effective alternative to these stages that would allow for micron precision control of the load applied to the sample beams and could be placed inside the SEM to perform *in situ* experimentation.

In the quest for a more cost-effective three-point bending apparatus, it was determined that building upon the initial simple design and creating a more upgraded version of this three-point bending stage would be the most advantageous route. One of the first updates that was considered was the loading pin. With the initial loading pin being a simple mechanical screw, several of the

challenges to centered around updating this component of the apparatus. In doing so, an actuator was purchased from Newport Corporation to act as the loading pin for the upgraded three-point bending apparatus. The actuator in question is the NSA12V6 (**Figure *15***) which has an 11-millimeter travel length, linear actuation, a minimum incremental motion of 0.2 microns, and a vacuum compatibility of 10^{-6} hectopascals or $7.5 \cdot 10^{-7}$ torr.

Figure 15: (A) NSA12-V6 High Vacuum safe actuator with CONEX-PP control modem attached from Newport Corporation. (B) Purchased NSA12-V6 with CONEX-PP controller removed and a 9-pin plug attached to allow the actuator to be connected to the electrical feedthrough on the shell of the SEM, to allow for in-situ testing. (C) The actuator mounted on the three-point bending stage to allow for placement in the SEM.

The minimum incremental motion of the actuator of 0.2 microns provides the precision control necessary to apply the load at small increments, allows for effective control of the bend of the nacre beam samples. The more control over the bending of the beams, the easier it will be to capture images of tablet gaps forming in the nacre architecture. The compatibility with the high vacuum pressures also means that the actuator can be placed inside the SEM to perform *in situ* testing. A minor speed bump was encountered with this though. Initially, the actuator was attached directly to the control module, which needed to be connected to a computer via a USB port in order to control the actuator.

A simple remedy was proposed and implemented in order to overcome this hurdle. First, a nine-pin electrical feedthrough was purchased from Kurt J. Lesker Company and affixed to an open port on the SEM. Next, the cable connecting the actuator and the control module was severed at a point nearer to the actuator. The wiring for each side was aligned into separate nine-pin VGA port connectors. This allows for the actuator to be placed inside the SEM and have the cable connected to the inner side of the electrical feedthrough. The cable connected to the module can then be connected to the exterior portion of the electrical feedthrough so that the actuator can be powered and controlled from outside the SEM.

The next part of the three-point bending apparatus to be assessed was the mounting stage for the actuator and the sample beam. The design for the mounting stage for the three-point bending apparatus can be seen here in **Figure *16***, and was designed using SolidWorks software. The design for the mounting stage was based off of the standard 32-millimeter aluminum pucks used for mounting samples for imaging inside the SEM. The stage was designed to be cylindrical and have a diameter of 32 millimeters so as to fit inside the sample holder that was already available for holding sample specimens of the same size. Precise measurements of the actuator were made using

a caliper to determine the best method of attaching it to the mounting stage. The preference was to have the actuator fit into the mounting stage in a way that would allow the shaft of the actuator to move freely towards the nacre beam samples as they tested on the support pins. To aid in this endeavor, a notch and groove were designed in the mounting stage to help house the actuator. The notch was positioned at the opposite end of the support span and would allow for the square like outer housing of the actuator to rest comfortably inside. The notch would also assist in positioning the shaft of the actuator so that the center of the tip of the actuator would align with the center of the nacre beam samples. The groove was positioned on the top surface to hold the outer cylindrical casing of the shaft of the actuator. The groove was extended to run the entire length of the mounting stage to provide the shaft of the actuator unimpeded movement for the full range of motion. Two small pins were placed equally spaced on either side of the groove at the furthest end of the mounting stage. These would act as the support span for the three-point bending as well as a mounting point for the nacre beam samples during the transfer into the SEM.

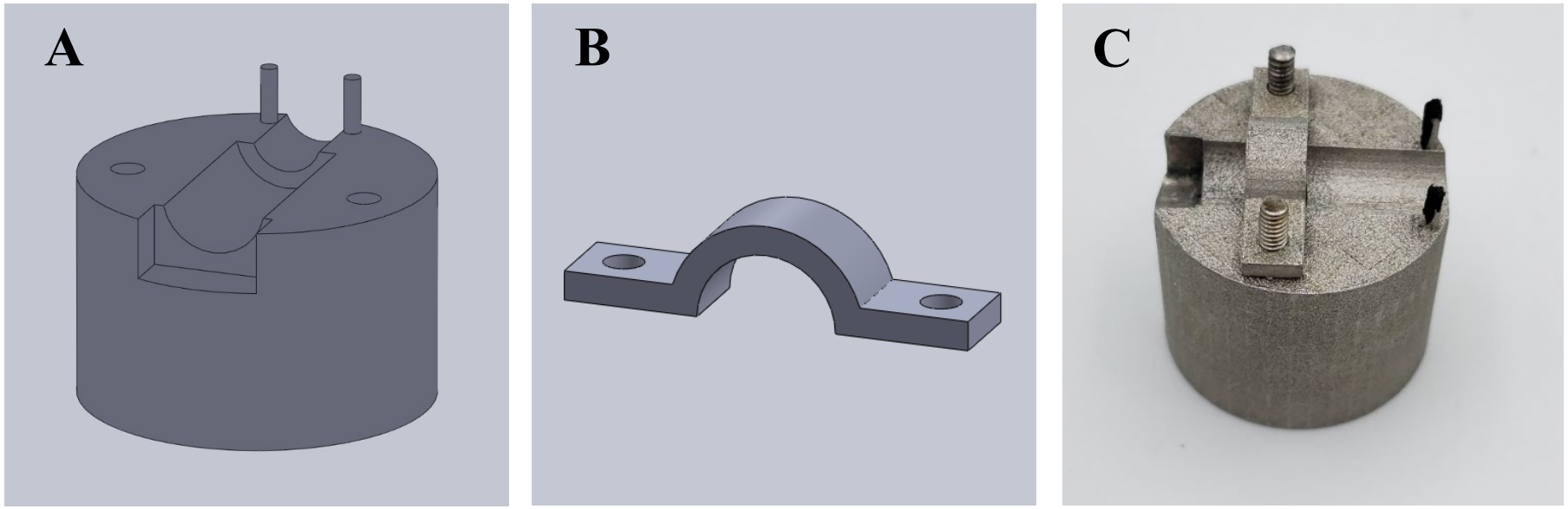

Figure 16: Images of the three-point bend mounting stage for housing the actuator and securing the sample. (A) The mounting stage part as it was designed in SolidWorks. (B) Curved bracket used for affixing the actuator to the stage as designed in SolidWorks. (C) The mounting stage and the curved clamp printed with the Concept Laser printer using 316 stainless steel powder.

Another point of consideration when designing the mounting stage was the rather large cylinder that houses the driving components of the actuator. When the components would eventually be assembled, the three-point bending apparatus would be placed into the 32-millimeter sample holder and placed inside the SEM. Given the standard dimensions for a 32-millimeter aluminum puck used for sample mounting, the outer housing of the actuator would crash into the sample holder and would prevent the three-point bending apparatus from being properly secured. To prevent this from occurring, the height of the mounting stage was increased significantly so as to allow the outer housing of the actuator and the wall of the sample holder to remain separated.

One of the final design concerns was in securing the actuator to the mounting stage. While the notch and grove would be fairly secure, any unsecured movement of the actuator during the testing process may cause inaccurate results. To remedy this concern, a method of securing the actuator fully to the mounting stage was devised. Using the measurements of the actuator, a horseshoe shaped coupling component was designed, as seen in **Figure *16* B**. The coupling component would fit over the outer housing of the shaft of the actuator to secure it to the mounting stage. Two holes were positioned on either side of the groove in an area of the mounting stage where the exterior housing of the shaft would rest. These holes would pass through the entire height of the mounting stage. Two threaded holes were aligned with the holes in the mounting stage and cut into the coupling component. A pair of set screws would be used to tighten the coupling component down onto the outer housing of the actuator shaft, thus securing the actuator to the mounting stage and completing the upgraded version of the three-point bending apparatus.

The final hurdle to leap over was in procuring or manufacturing the mounting stage for the upgraded version of the three-point bending apparatus. Initially, it was thought that the components could be machined by hand in house with equipment and components already available. However,

the intricacies of the upgraded design for the mounting stage made this a very difficult prospect. The next option was to send the design off to a company to be machined using a CNC machine. This option may have been costly due to the small order size, the small component size, and the intricacies of the components themselves. Fortunately, a third option presented itself.

A Concept Laser MLab 100R additive manufacturing machine was recently procured and made available for use in printing metal parts. This machine has the capability and precision necessary to produce small parts with ultra-fine details. The parts can also be printed using any metal powder available (provided a printable powder form of the desired material is produced), in order to produce components with the desired material properties. Fortunately, for the purposes of the components for the mounting stage, the material properties are not of vital concern and as long as they are comprised of a sturdy enough metal, any available metal powder would satisfy the material requirements for this particular print job.

The powder chosen to print the components for the three-point bending apparatus was 316 stainless steel. This decision to use 316 stainless steel was attributed to both the strength of the metal and the excess availability of the powder. Once the powder was procured, the design files were converted into build files and printed using the Concept Laser 3-D printer. After removing the components from the build plate, they were placed into an ultra-sonic vibratory bath to perform an initial cleaning. During initial construction of the advanced three-point bending apparatus, it was found that the notch on the mounting stage and the inner wall of the coupling component were slightly too narrow for the actuator to fit in properly. Using a grinding and polishing attachment for a Dremel tool, the sharp edges of the mounting stage were rounded off and the inner walls of the notch and the coupling component were slowly polished and ground until they were widened enough. This allowed the actuator to appropriately fit into the notch of the mounting stage and be

secured to the mounting stage by the coupling component. With the three-point bending apparatus finally assembled, the testing of nacre beam samples in pursuit of observing and characterizing wide scale reversible tablet sliding could begin.

2.5.3 Use of Equations in Calculating the Global Flexural Strains

In performing three-point bend testing, calculations for the global flexural strain were performed using a set of equations. **Equation 1** is an equation for flexural strain that occurs on the outermost surface of the rectangular cross-section undergoing three-point bending. This equation is derived from the bending moment of a rectangular beam. In this equation, **ε** is the maximum strain at the outer surface of the rectangular beam; δ is the amount of deflection, in nanometers, applied to the mid-span of the beam; h is the thickness of the rectangular sample beam, in nanometers; L is the support span of the three-point bending stage, in nanometers. Measurements for the thickness of the sample beams and the support span were made using the images captured using the SEM. The amount of deflection of the beam for each stage of actuation was controlled and recorded by the software that came with the actuator.

Equation 1

$$\boldsymbol{\varepsilon = \frac{6\delta h}{L^2}}$$

These measurements were then used in coordination with **Equation 1** to calculate the strain at the outer most surface of the sample beam at each stage of bending. Once these strains for each of the actuation stages were calculated and recorded, **Equation 2** was used to calculate the strain at each individual tablet pair for caps that were imaged. This equation is a measurement of the strain at varying distances from the neutral axis that exists in the middle of the rectangular beam. In this equation, ε_x is the calculated strain in relation to the distance from the neutral axis of the sample beam; ε is the maximum strain at the outer surface of the sample as calculated using **Equation 1**; x is the distance of the tablets away from the neutral axis, in nanometers; d is the overall distance of the outermost surface of the beam, in nanometers.

Equation 2

$$\boldsymbol{\varepsilon_x = \varepsilon \frac{x}{d}}$$

The measurement of the neutral axis was taken as the mid-point of the total thickness of the sample beam, as measured using images captured with the SEM. The measurements for the tablets were taken using captured images of the nacre architecture using the SEM. The position of the measurement was set as the midpoint of the nacre tablet, as this would be where the measurements for the tablet gaps were also to be made.

3. Macroscopic Three-Point Bending of Nacre Architecture

The purpose of this work was to apply some deformation to the nacre architecture of the California Red Abalone in order to understand the effects of the unloading conditions that this unique structure undergoes. As previously stated, the abalone nacre architecture had previously only been examined under failure conditions in which the structure was strained beyond any possible recovery, and thus really only providing us with information on the architecture under these specific conditions. Without knowledge of the reversible mechanism of the nacre architecture, the engineered materials that base themselves off of this structure are missing crucial information needed to properly replicate the abalone architecture. Some works has glimpsed the possibility of a reversible sliding mechanism being present in the architecture, but other than inferring its existence not much else has been done to investigate the presence of this mechanism.

This work seeks to remedy that oversight by subjecting the nacre architecture to loading and unloading conditions so as to observe and attempt to characterize the reversible sliding mechanism that may be present in the nacre architecture. In order to make this possible, samples of the abalone nacre were sectioned off and were subjected to three-point bend mechanical testing in an attempt to capture large scale reversible sliding occurring in the nacre architecture. Once images of widescale reversible sliding were captured, a way to relate what was occurring on the macroscopic level to what was occurring on the micro- and nanoscopic level to the nacre architecture was needed.

Using the geometry of bending beam to calculate the maximum strain at the apex of the beams bend and the ratio between the strain at the apex and the strain at the neutral plane of the sample,

a measurement of the strain at each individual tablet as it is strained could be calculated. The knowledge of the strain at the tablet level would allow us to understand the amount of strain needed to fracture the biopolymer which is believed to be the main driving force behind the reversible sliding mechanism that may be present in the nacre architecture.

3.1 Initial Feasibility Test

To test the feasibility of this testing method, an initial simple testing apparatus was designed, and nacre beam samples were tested with it to determine if this testing method would be appropriate for imaging wide scale reversible sliding in the nacre architecture. Initial experiments were performed by previous colleagues in the research group on nacre architecture sample beams using a simple three-point bending apparatus (**Figure 17**). In designing and constructing this apparatus, first an aluminum puck was machined to create a working surface for the apparatus. A set of pins were machined out of the puck to act as the support span for the three-point bending experiment. Next, a grooved wall was machined on the opposite side of the support span pins to act as a structure to house the loading pin. For said loading pin, a screw was threaded through the grooved wall and fitted with a coupling nut to hold the screw in place after tightening. The end of the screw was covered in a piece of carbon tape, in order to prevent the end of the screw from cutting or scraping the nacre sample beam. It should be noted that this device was only used to perform qualitative experiments.

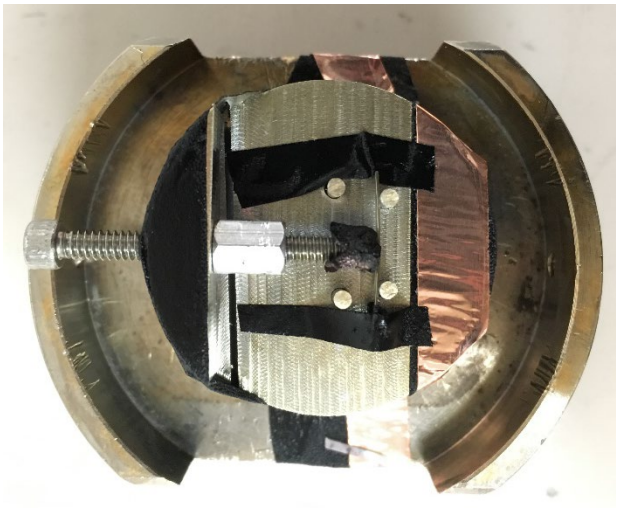

Figure 17: Simple three-point bending apparatus that was used for initial bending experiments with the abalone nacre architecture.

For these experiments, the abalone nacre was ground into thin slides of roughly 300-600 microns of thickness. The cross-sectional sides of the slides were polished thoroughly, and the slides were then separated into sample beams using a utility knife. The width of these strips was in the range of 300-500 microns. The finely polished face would act as the viewing surface for the beam bending experiment.

The nacre beams were then loaded into the apparatus with the polished surface facing upwards so as to image the nacre architecture under bending conditions. Then, the screw was rotated clockwise to apply a load to the nacre beam, causing it to be bent. This loading process needed to be performed very carefully, as due to the brittle nature of the nacre architecture, it was quite easy to bring the beams to a failure point. After placing the nacre beam under a bent condition, the apparatus was placed into the SEM to perform imaging and characterization of any wide scale tablet sliding.

First, the nacre beams were placed under a small load using the mechanical screw to create a slight bend in the beam. The testing apparatus was then placed inside the SEM. Measurements of the beam were made and images of the microstructure of the nacre architecture were captured. The apparatus was then removed from the SEM. The screw was then turned further to increase the load on the nacre beam and bring the beam under a greater bending state. The testing apparatus was placed back into the SEM and measurements of the nacre beam and images of the microstructure were captured. Once again, the apparatus was removed from the SEM and the screw was then rotated counterclockwise to remove the load from the nacre beam to bring it back to an unbent state. Finally, the apparatus was returned to the SEM and images of the microstructure were captured under the unbent state.

In **Figure 18**, we can see captured SEM images of the same location in the nacre architecture taken under the different bending conditions as well as an overall view of the bending apparatus under the different bending conditions. Circled in these images are specific residual debris left on the surface of the polished nacre architecture that was used in both identifying and confirming that each of the images were taken in the exact same location. There were some slight imperfections in this three-point bending apparatus, which caused the beam to become slightly tilted when the load was fully released. Thus, even though all of the images in **Figure 18 A-C** were taken at the same magnification, **Figure 18 C** captures a slightly different area than that of **Figure 18 A-B**. The white dotted square on **Figure 18 C** contains the same area as **Figure 18 A-B**.

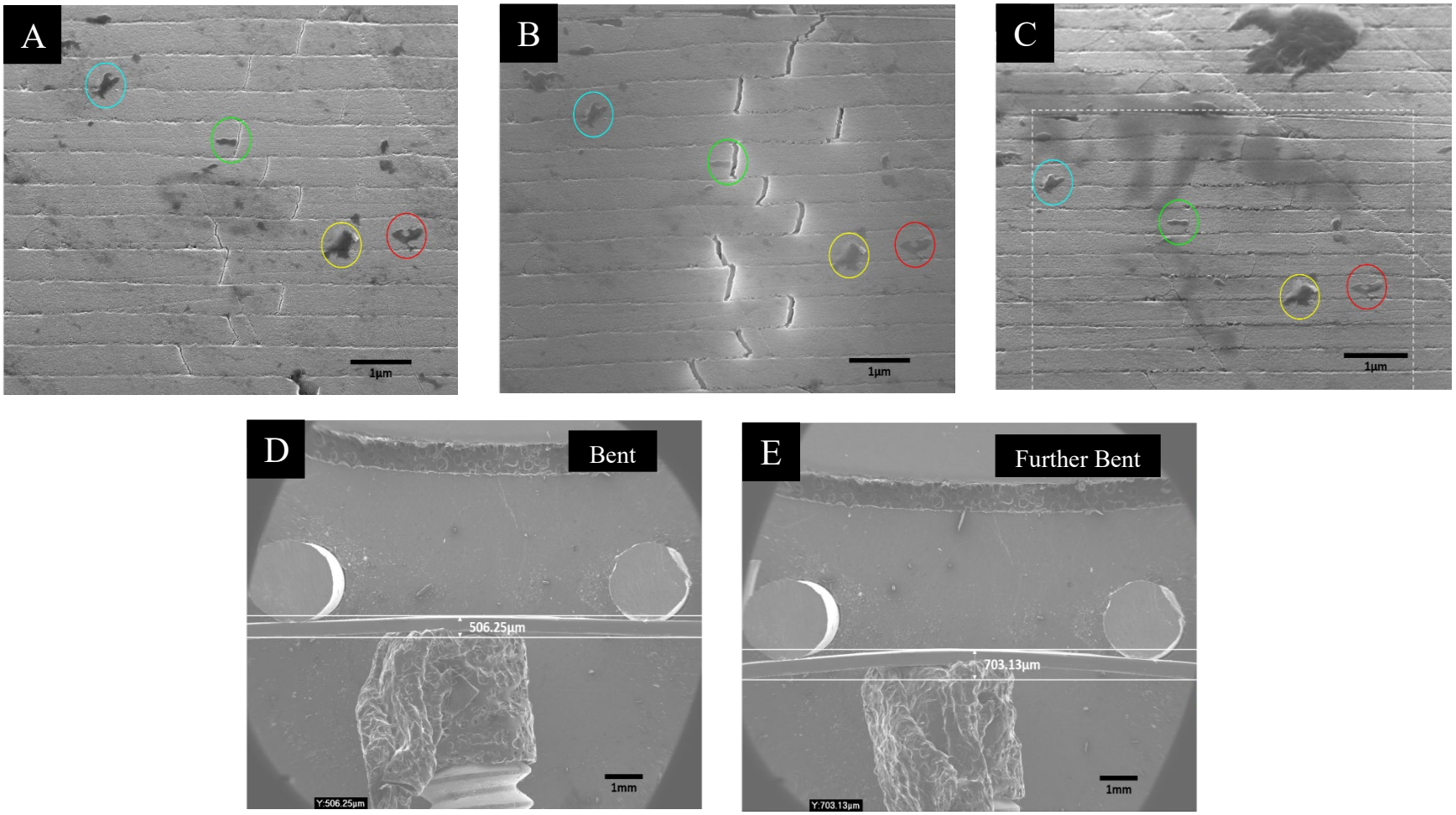

Figure 18: SEM images captured of an initial three-point bending experiment. Images of the microstructure in the same area under (A) initial bending, (B) further bending, and (C) released conditions. Overarching images of the nacre beam and the three-point bending stage were captured under (D) the bent, and (E) the further bent conditions.

These SEM images reveal some of the first instances of reversible sliding to be captured. As shown in **Figure 18 A**, as the nacre architecture is initially loaded into the slightly bent state, gaps between neighboring tablets start to form. As the nacre architecture is loaded further and the sample beam is bent even further, the gaps between the neighboring tablets expand further (**Figure 18 B**). Upon full reversal of the load on the sample beam, the gaps between the neighboring tablets appear to have fully closed (**Figure 18 C**), which indicates that some form of reversible mechanism is present in the nacre architecture. The locations of the previously observed gaps still remain distinguishable in the images due to permanent changes caused by the surface at the interface of the two neighboring tablets undergoing some degree of remodeling as they are brought back together.

Figure 19 depicts a set of images from another sample undergoing three-point bend testing. These images were taken at low magnification to show the nacre beam under both a bending condition and a fully released condition. Upon reaching the fully unloaded state, some residual displacement in the nacre beam could still be observed. SEM images of the microstructure of the nacre architecture were taken at a higher magnification under both loading and fully unloaded conditions. The location for these images were confirmed by comparing local details and artifacts in the area where the images were captured.

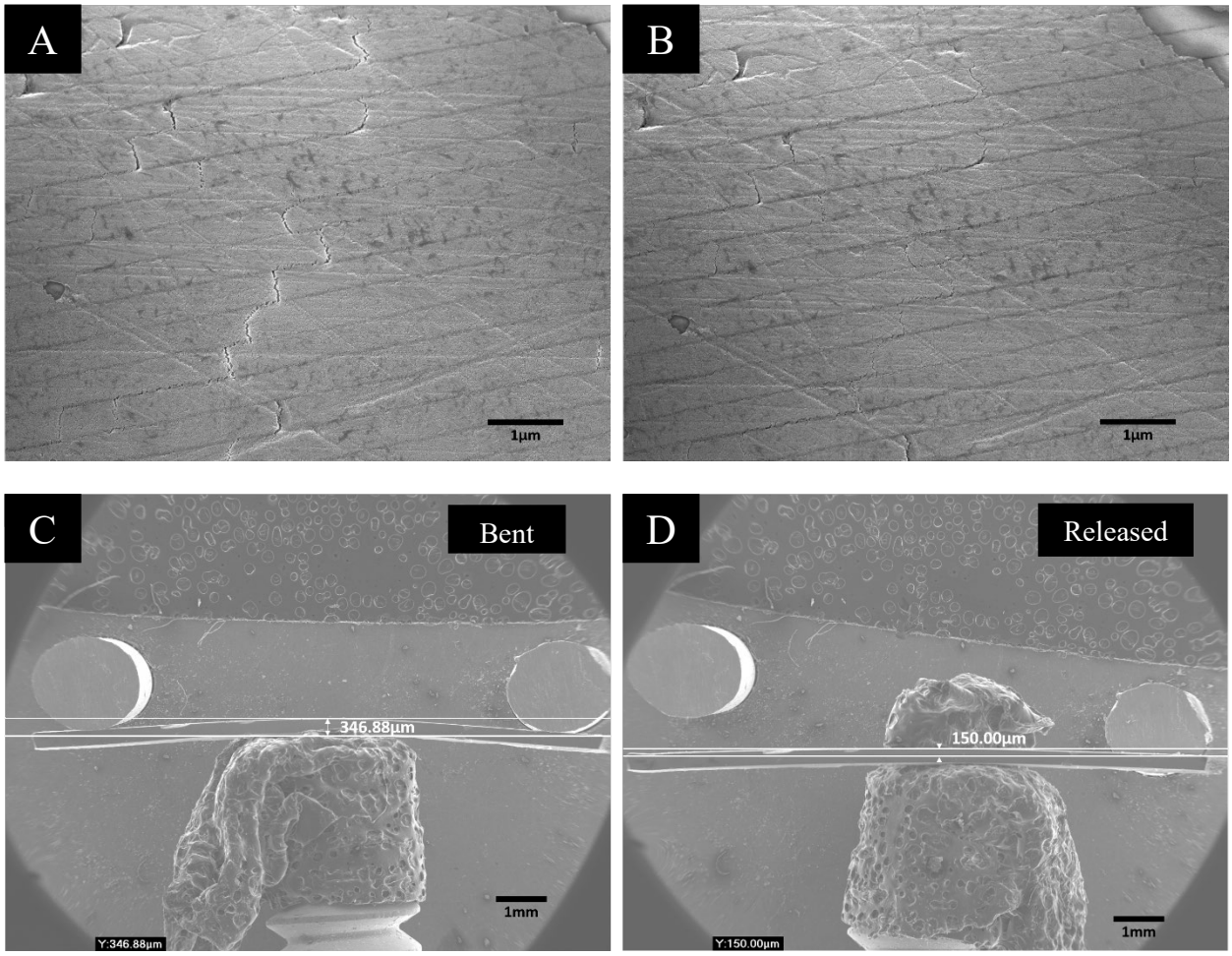

Figure 19: SEM images captured from another experiment of the nacre architecture under (A) bent and (B) released conditions. Images of the overall bending experiment were also taken under the (C) bent and (D) released conditions.

When comparing the gaps formed by the three-point bend test performed on these nacre beams, the gaps that can be seen forming between the tablets in **Figure 18** are significantly wider than the gaps that are formed between the tablets in **Figure 19**, even though both samples underwent comparable amounts of bending displacement. There are many factors and variables that may have led to variation in the degree of tablet sliding between the two beam samples. For one, these samples were taken from the shells of two different abalone, which each may have experienced different growth scenarios. The SEM images (**Figure 18 A-C and Figure 19 A-B**) taken at high

magnification also reveal that the nacre architecture of the two beam samples have a different tablet inclination angle to the surface of the samples, which may have caused the variation in the gaps that were formed between the tablets. There is also the possibility that multiple locations within the nacre architecture have tablet sliding occurring, and the areas that were imaged may not be the primary location for tablet gaps forming. All of these factors may be contributing to the difference in the gaps that formed between the nacre tablets in these two separate nacre beams.

These results however are only just the beginning of experiments with the three-point bending method applied to the nacre architecture. While these initial experiments have shown the first instances of a reversible sliding mechanism and its presence within the nacre architecture, there were many challenges that needed to be solved in order to improve this experimental process. One such issue is that with the simple three-point bending apparatus it is not possible to easily control the bending displacement of the nacre beams. It also cannot be used *in situ* within the SEM, and constant placement, removal, and subsequent replacement of the apparatus into the SEM takes time. In order to accelerate the testing method and increase the control of the bending experiment an *in situ* testing mechanism is necessary.

3.2 *In Situ* Three-Point Bend Mechanical Testing of Nacre Architecture

In order to perform the *in situ* testing method, first, samples of the nacre architecture were prepared. These samples were sectioned from the abalone shell using a diamond tipped cut off wheel. The sections of the abalone shell were then ground and polished using the method previously stated in order to reveal the nacre architecture. After polishing the cross-sectional

portion of the beams, a thin film of gold was applied to the surface to aid in capturing the images of the nacre architecture.

Once the nacre beam samples were polished and coated, they were mounted onto a 32-millimeter aluminum puck using a piece of carbon tape. Several sample beams were placed into the SEM at a time to inspect both the quality of the polish on the cross-sectional side of the beam as well as the alignment of the tablets. The preferred alignment of the tablets was parallel with or as close to parallel with the direction of the sample beam as possible. Each sample was carefully inspected for these qualities. If the polish was too poor the samples were set aside to be polished and coated again. If the tablet angle was too great in the nacre beam sample, the beam would be discarded. When a nacre beam sample had both a sufficient polish and an appropriate tablet angle, it would be placed aside to be kept for the three-point bend mechanical testing.

After selecting the nacre beam samples that would be best suited for these experiments, the sample beams were taken to undergo three-point bend mechanical testing in an endeavor to capture images of wide-scale reversible tablet sliding. The samples were placed on the mounting stage against the support span pins. The sample beams were oriented vertically so that the polished and coated cross-sectional portion of the nacre beam was visible and the point of incident for the electron beam so that imaging of this portion could take place during the testing process. To ensure the sample beams remained in position when transferring the three-point bending apparatus into the SEM, two pieces of carbon tape were placed around the support span pins to affix the sample beams to the pins.

With the new and improved three-point bending apparatus constructed, the nacre beam samples polished, coated, and mounted onto the support span pins of the mounting stage, the final challenge before testing could be performed was in getting the three-point bending apparatus into the SEM.

The nature of the apparatus meant that it could not be inserted into the SEM by traditional means as the actuator needed to be connected to the electrical feed through to allow for external control during the *in situ* experiments. In order to accomplish the task of placing the three-point bending apparatus into the SEM, first the entire system was vented and brought up to atmospheric pressure. After venting the chamber, the three-point bending apparatus was placed inside the 32-millimeter sample holder and secured with a set screw. The sample holder with the apparatus was placed inside the SEM by hand and secured on the sample stage.

Next, the nine-pin plug attached to the actuator was carefully passed towards the electrical feedthrough and inserted into the interior port of the feedthrough. The electrical feedthrough was secured back in place on the SEM and the nine-pin plug connected to the exterior port. The power indicator light on the rear housing of the actuator was observed to ensure that the actuator was properly powered before any further progress was made. After observing that the actuator was properly powered, the SEM was sealed back up and the chamber was allowed to be pumped back down to the operational pressure. While the chamber worked to reach pressure again, the shaft of the actuator was advanced slightly to a point before making contact with the sample surface to ensure that any trapped air in the actuator was removed during the pumping process. The sample stage was also raised and the three-point bending apparatus was positioned appropriately to allow for optimal image capturing of the nacre architecture during the testing process. Once the operational pressure inside the SEM was achieved, the testing of the nacre architecture could get underway.

At the outset of the testing of the abalone nacre, the shaft of the actuator was brought near to the point of contact with the nacre beam sample. The shaft of the actuator was advanced slowly by very small increments between 10 and 20 microns at a time until the head of the shaft appeared to

make contact with the surface of the nacre beam sample. Once the initial contact with the sample beam was established, the shaft of the actuator was advanced 50 microns and then the 50 microns of actuation was immediately reversed. This actuation and reversal were performed to confirm that the initial contact was the correct point and that the sample beam was firmly secured to the support span pins. If after the actuation was reversed the shaft of the actuator was no longer in contact with the surface of the sample beam, the actuator shaft was advanced slowly at an interval of 10 microns at a time until contact was reestablished. Confirmation of the contact was made visually by scanning the outer surface of the sample beam with the SEM. The magnification of the SEM was increased to 5,000x. As the shaft of the actuator was advanced incremental, the images of the nacre architecture were closely watched for any motion. When the portion of the nacre architecture that was in view advanced with the shaft of the actuator, the actuator and the sample were confirmed to be in contact with one another. The actuator was then reversed 10 microns so that the sample beam could return to an undeformed state.

From here, now that the head of the actuator was confirmed to be in contact with the sample surface, the three-point bend testing of the abalone nacre beams could begin. Beginning from the initial contact, the actuator shaft was slowly advanced 50 microns. Once the shaft had come to a rest, the outer surface of the sample beam was scanned for signs of neighboring tablets beginning to slide apart. As seen with the previous experiments (**Figure 18 and Figure 19**), as the neighboring tablets begin to pull apart from one another, a charge starts to build up alongside the edges of the interface between the two tablets. This buildup of the charge causes these edges of the tablets to appear much brighter than that of its surroundings, making them much more visible and thus easier to locate and track. Early experiments with the initial three-point bending apparatus revealed that due to the stochastic nature of the nacre architecture the main source of tablet sliding

is not always positioned at the point directly opposite the exact center of the actuator shaft acting as the loading pin. For this reason, a region having a range of roughly one millimeter (~500 microns to both the left and right of the exact center of the actuator shaft) of the outermost surface would be scanned for signs of wide scale reversible tablet sliding.

Once the range of the outer surface was scanned for signs of tablet sliding, assuming none was found, the shaft of the actuator was advanced another 50 microns, allowed to come to a rest, and the process of scanning the outer surface of the sample began again. This process was repeated until signs of wide scale tablet sliding was observed in the outermost surface of the nacre architecture. At this point, the area of interest where the tablet sliding was observed was recorded and scanned for any distinguishing or defining artifacts that would assist in recapturing the precise location going forward. The actuator shaft was then reversed slowly to the point of initial contact, allowing the nacre beam to return to an undeformed state. After allowing some time to pass to allow for the nacre architecture to respond to the release from the load that was applied, several images of the area of interest where tablet sliding was initial observed were captured and recorded as the point of undeformed nacre architecture.

Using the distinguishing artifacts in the first images taken while in search of tablet sliding, the area of interest was relocated following the reversal of the actuator shaft. Images of the area of interest were captured at various magnifications, including 5000x, 10000x, and 20000x, in an attempt to gather as much information about the nature of the reversible sliding mechanism as possible. Once these images of the initial state of the nacre architecture were captured, the shaft of the actuator was slowly advanced 50 microns to begin bending and deforming the nacre architecture. After the shaft of the actuator came to a rest, the area of interest was relocated using the defining artifacts that had previously been located. Once back in view, images of the area of interest with a now

deformed nacre architecture were captured at the various magnifications. Following the image capturing, the actuator shaft was advanced another 50 microns, allowed to come to rest, the area of interest was relocated, and images of the area were again captured at various magnifications. This process was repeated until the actuator shaft had reached a travel distance of 300 microns.

Following the image capturing at this stage, the actuator shaft was subsequently reversed 150 microns to begin the process of capturing images of the reversible sliding mechanism in the nacre architecture. After the reversal of the actuator shaft was complete and the shaft had come a rest, an amount of time was allowed to elapse to allow the nacre architecture to respond to the unloading. Once enough time had elapsed, the area of interest was relocated, and images of the sliding reversal were captured at the various magnifications. The actuator shaft was again reversed 150 microns, to return the original initial contact point to relieve the entire load applied. After allowing some time to elapse, the area of interest was relocated a final time. Images of the nacre architecture after returning from its deformed and bent state were captured at the various magnifications once again. Images of the bending process can be seen in **Figure *20*** and **Figure *21***. In **Figure *20*** the entire area of the nacre structure that was captured can be seen as it undergoes various degrees of actuation, from 150 microns (**Figure *20* A**), up to 300 microns (**Figure *20* D**), and all the way through to full reversal of the actuation (**Figure *20* F**). Here we see the nacre architecture from the outermost surface of the sample beam down through about the first forty tablets or so. The nacre architecture here is undergoing a large amount of sliding as is seen in the **Figure *20* D**, when the actuation reaches its peak. The tablets here have very large visible separations between them, the largest of which being at the top of the images near the outer most surface of the sample. As we travel further down the image, the gaps between the tablets begins to lessen the deeper into the sample the images were captured. Upon reversing the actuation

completely (**Figure *20* F**), the gaps between the tablets can be seen undergoing a recovery and reversing. The tablets near the outer most edge can still be seen with a noticeable and measurable gap between them, with the highest tablets having the greatest gaps and the gaps between the tablets diminishing as we travel further down the sample image. Highlighted in **Figure *20* F** (the highlighted area in **Figure 20 F** at the lowest portion of the captured images of the nacre architecture, we see that the gaps in the tablets in this particular area can no longer be observed. This would indicate that the nacre structure in this area had fully resolved the gaps that had formed between the tablets. This area is further highlighted in **Figure 21**.

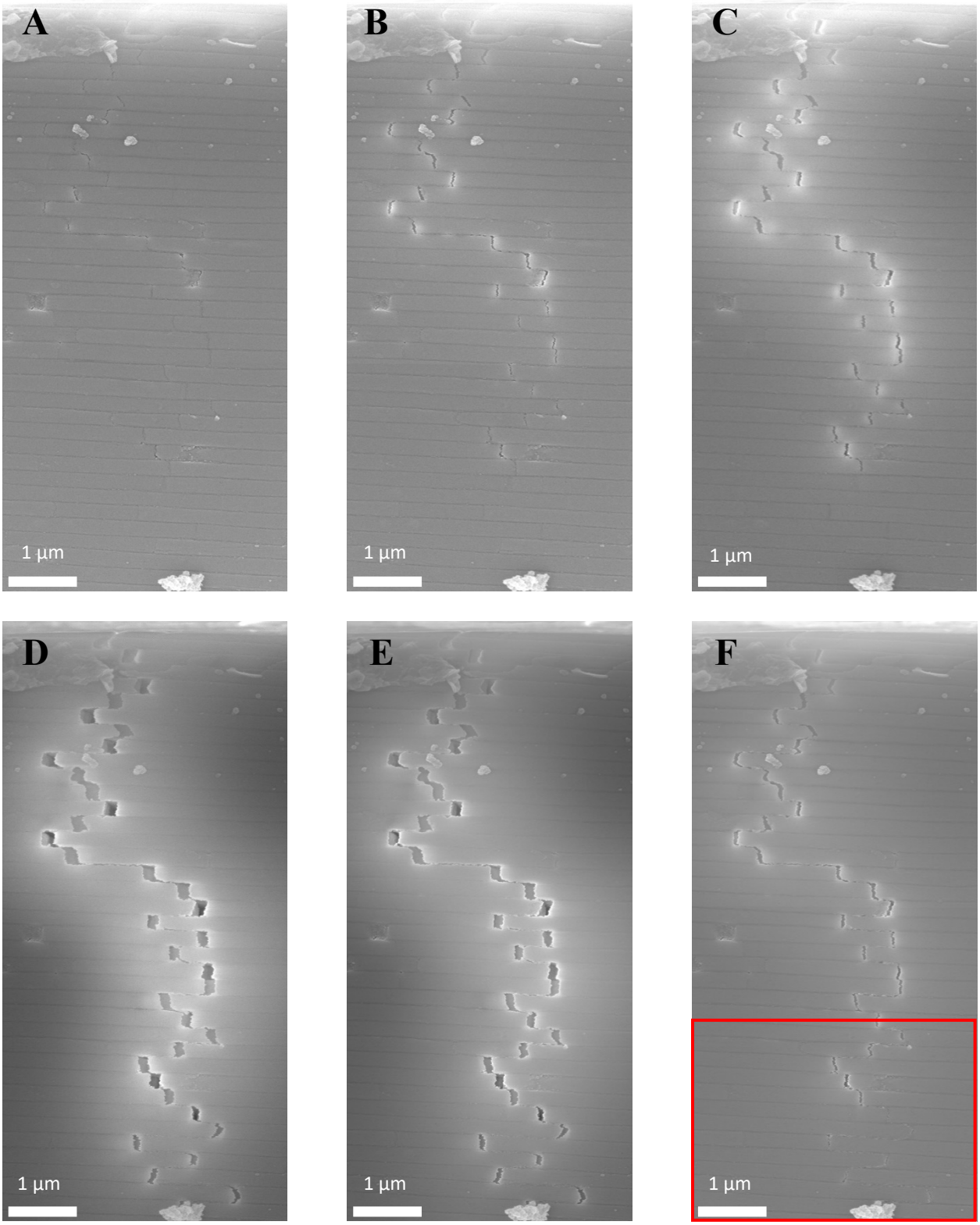

Figure 20: Images of wide scale tablet sliding captured in the nacre architecture undergoing three-point bend testing at various stages of actuation including forward actuation to (A) 150 microns, (B) 200 microns, (C) 250 microns, and (D) 300 microns as well as reversal actuation to (E) 150 microns and (F) complete reversal to 0 microns of actuation. These images were captured of the overall nacre structure and include tablets from the outer most surface of the nacre sample beam.

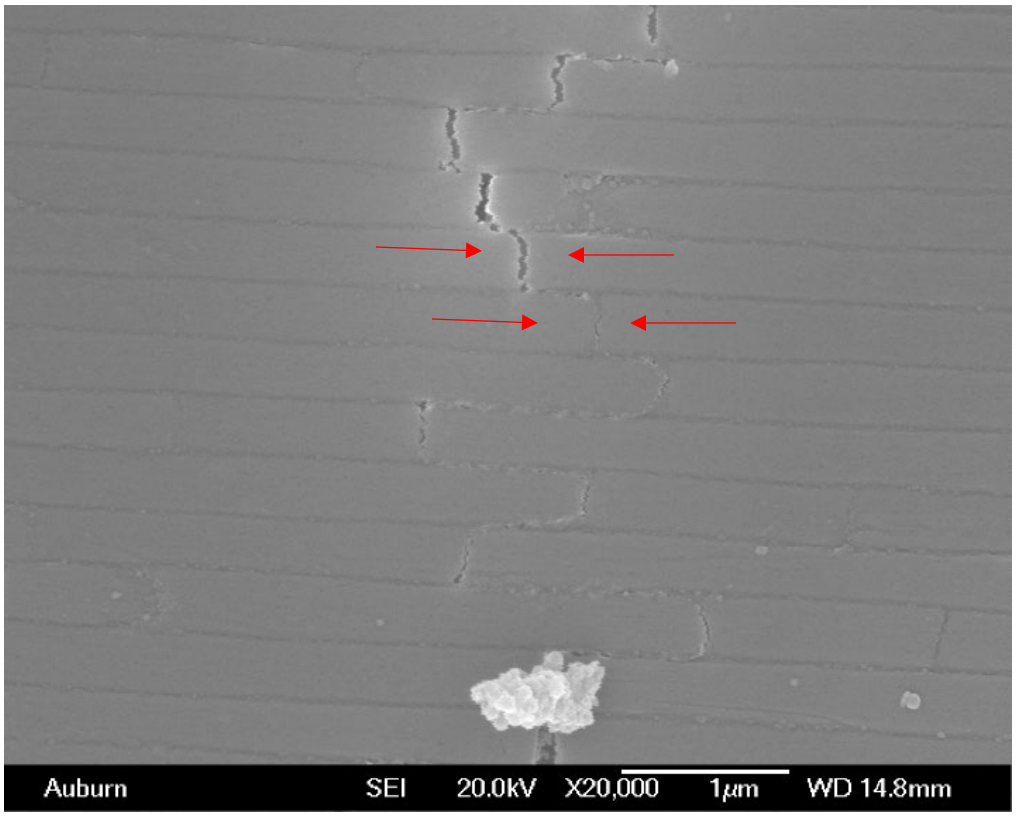

Figure 21: A magnified image of the highlighted area in the **Figure 20 F**. Here the last tablets to have an unresolved gap and the first to fully resolve its gap can be seen highlighted by the red arrows.

Focusing on this area of the captured images, the nacre architecture can be seen undergoing a large amount of localized strain as the sample beam is bent further and further. Initially, we can see that there are no visible gaps present between neighboring tablets even after the actuator shaft had been advanced 150 microns (**Figure 20 A**) and the sample beam had undergone significant bending. Upon advancing the actuator shaft to 200 microns of actuation (**Figure 20 B**), a separation between a few of the tablets begin to become apparent both by the visible gap forming between them and the increased brightness around the edges of the tablet-tablet interfaces, caused by the charge build up in this area. After advancing the shaft of the actuator to 250 microns of actuation (**Figure 20**

C), the gaps forming between the tablets begin to widen further and the interfaces begin to grow brighter. When the actuator shaft is advanced to 300 microns of actuation (**Figure 20 D**), the vast amount of local strain applied to the nacre architecture can truly be seen. At this point, all tablets in view have a visible gap formed between them and their neighboring tablet. For some of these tablet pairs, the separation between them is quite large indicated by the significant size of the gaps formed between them and the brightness of the interface between the two tablets caused by a greater amount of charge build up. The nacre architecture in this location has undergone a significant amount of localized strain, while the overall nacre structure remains intact. This depicts the overall key advantage of the tablet sliding deformation mechanism that is afforded to the abalone's nacre architecture, developed over millions of years of evolution. While this mechanism has been extensively explored, it is the subsequent imaging of this testing method that reveal the unknown of the unloading process and how it is applied to the nacre architecture.

When the shaft of the actuator is reversed to 150 microns (**Figure 20 E**), the nacre architecture undergoes a reversal in the load applied to it as well as a degree of unbending. Upon this reversal, the amount of separation between the tablets and their neighbors can be seen undergoing a reduction, while the brightness on the edges of the interface between these tablets is reduced as well. This closing of the tablet gaps reveals the early stages of the reversible sliding mechanism occurring in the nacre architecture. Once the actuator shaft is reversed fully to the initial contact point (**Figure 20 F**), the true nature of reversible sliding mechanism is revealed. At this point, most of the tablets visible in this area have had the gaps which had formed between them and their neighboring tablet completely resolved. These tablet pairs have rejoined one another and the interfaces between them have been remodeled and reformed. This interface remodeling can be caused by many factors which prevent the perfect reformation of the tablet-tablet interface,

including the formation and build-up of debris along the horizontal edges of the tablets, caused by the fracture of mineral bridges between the tablets, as well as the build-up of debris in the gap formed between the tablets. The main driving force behind the gaps between the tablets closing and reforming is believed to be the biopolymer matrix that is prevalent throughout the entirety of the nacre architecture. As the strain on the nacre architecture is increased and the tablets begin to slide further and further apart from one another, the biopolymer between them is also strained and stretched. When the load on the nacre architecture is reversed, the strain on the biopolymer is relieved and the biopolymer is able to relax. As the biopolymer relaxes, it begins to pull the tablets that it is connected to back together again. For most of the tablets in these images, the biopolymer was able to completely reform the gaps that had formed between them. However, this was not the case for all the tablets present in the nacre architecture in these images.

While some of the tablet pairs have resolved their gaps, other tablet-tablet interfaces have a gap between them that still remains even after the actuation is fully reversed. The remaining gap between tablets indicates that the organic matrix was not able to assist in reforming the interface between the tablets fully. This would indicate that at some point during the loading and bending process, the gaps that formed between these tablets was so great that it caused the biopolymer that connected them together to fracture, preventing the biopolymer from reforming the tablet-tablet interface.

In **Figure 21**, the point at which the delineation between tablets that reformed their interfaces and the ones that did not is highlighted by the red arrows. This position shows a clear and distinct delineation, where one set of tablets was not able to reform the interface with its neighbor whereas the tablet pair immediately below them was able to. This would indicate that the difference in the strain that was applied to these tablets and as well as the difference in the size of the gap formed

between the tablet pairs could indicate the point at which the biopolymer fractures and is no longer able to assist in the reversible sliding mechanism between the adjacent tablets. This would be explored with further analysis of the images captured during the testing.

While the upgraded version of the three-point bending apparatus allowed for more control during the experimentation process, as well as allowing for the degree of actuation to be accurately measured, there were still certain things that the system could not provide. For instance, unlike the extremely expensive commercially available three-point bending stages, this apparatus could not provide a direct measurement of things such as the stress or strain being applied to the sample during the testing process. Even though there wasn't a readily available method of assessing the stress applied to the nacre beam during the three-point bending experiment, there is a way that the macroscopic global strain could be measured indirectly using the geometry of a bending beam under these conditions. This overall maximum global strain could then be used to calculate the strain at each individual tablet level. The global strains at each of these tablets could also then be compared to the gaps formed between the tablets. Given the clear delineation between the tablets that were able to resolve the gaps between them and those that were not able to, this would provide a measurement of both the size of tablet gap and the global strain applied to a tablet necessary to fracture the biopolymer, thus preventing the biopolymer from aiding in the reversible sliding mechanism. But before any of this could be performed, measurements of the captured images of the nacre architecture during the various stages of bending needed to be performed.

In order to further analyze the reversible sliding mechanism present in the nacre architecture, a measurement of the gap formed between pairs of adjoining tablets was made at the various stages of actuation. Using the images captured of the three-point bending experiment in **Figure 20**, the gaps that formed between tablets at the different stages of actuation were measured using ImageJ

software. The images that were captured for each of the different stages were loaded into the ImageJ software, the scale was set using the scale bar provided with the image, and the gaps between each of the tablets was measured and recorded for each of the stages. The measurements for the tablet gaps were taken approximately at the middle of the tablet, to ensure consistency. The thicknesses of the individual tablets as well as the overall thickness of the nacre beam were also measured using the ImageJ software for use in the strain calculations. All of these measurements were recorded in a spreadsheet to be used in analyzing the reversible sliding process.

The gap measurements for the different stages of actuation are presented graphically as a function of the tablet's depth from the outer most surface in **Figure 22-Figure 23**. As seen in **Figure 22**, the first stage that is presented is the 150 microns of forward actuation as this was the first stage where visible gaps between neighboring tablets was captured in images. At this stage, only some of the tablets closest to the outer surface of the nacre beam can be seen forming a gap between one another. When the actuation reaches 200 microns, the tablets which had already been engaged in sliding began to slide apart further, and some of the tablets which had not previously begun sliding now have a visible and measurable gap formed between them. After the actuation has reached 250 microns, the measurements of the gaps between the tablets have increased further while only one new set of tablets can be seen forming a visible gap between them. Finally, once the actuation reaches 300 microns, the measurement of the gaps between neighboring sets of tablets jumps drastically and now all tablets that were imaged can be seen with a visible gap formed between them.

Figure 23 shows the tablet gaps at the maximum actuation of 300 microns compared to the measured tablet gaps as the actuation was reversed. As the actuation was reversed to 150 microns, all of the measured gaps between the neighboring tablets can be seen decreasing across the board.

The amount of gap that is recovered from this initial unloading and unbending is small however, and the measured gap between the neighboring tablets for the reverse 150 microns is far greater than that of the gaps measured for the initial 150 microns of forward actuation or even those measured for 250 microns of forward actuation (**Figure 22-Figure 23**). This may indicate the presence of some degree of relaxation period to the reversible sliding mechanism in the abalone nacre architecture. Upon returning to the fully unloaded and undeformed state, many of the tablets still have a residual measurable gap between the neighboring tablets. This residual gap coupled with the rapid increase in the measured tablet gap between 250 microns and 300 microns of actuation, seen in **Figure 22**, may indicate that the biopolymer between these tablets was fractured due to the localized strain caused by the tablet sliding and thus was not able to assist in the reversible sliding mechanism. Alternatively, the tablets that were imaged furthest down in the nacre sample which were the last to begin sliding have completely recovered the gap that had formed between them. Here, the biopolymer remained intact which allowed the gaps between these tablets to fully close. While the measurement of the tablet gaps provides significant information with regards to the reversible sliding mechanism present in the nacre architecture, a measurement of the macroscopic global flexural strain at the depth of the various tablets may provide further insight into this mechanism.

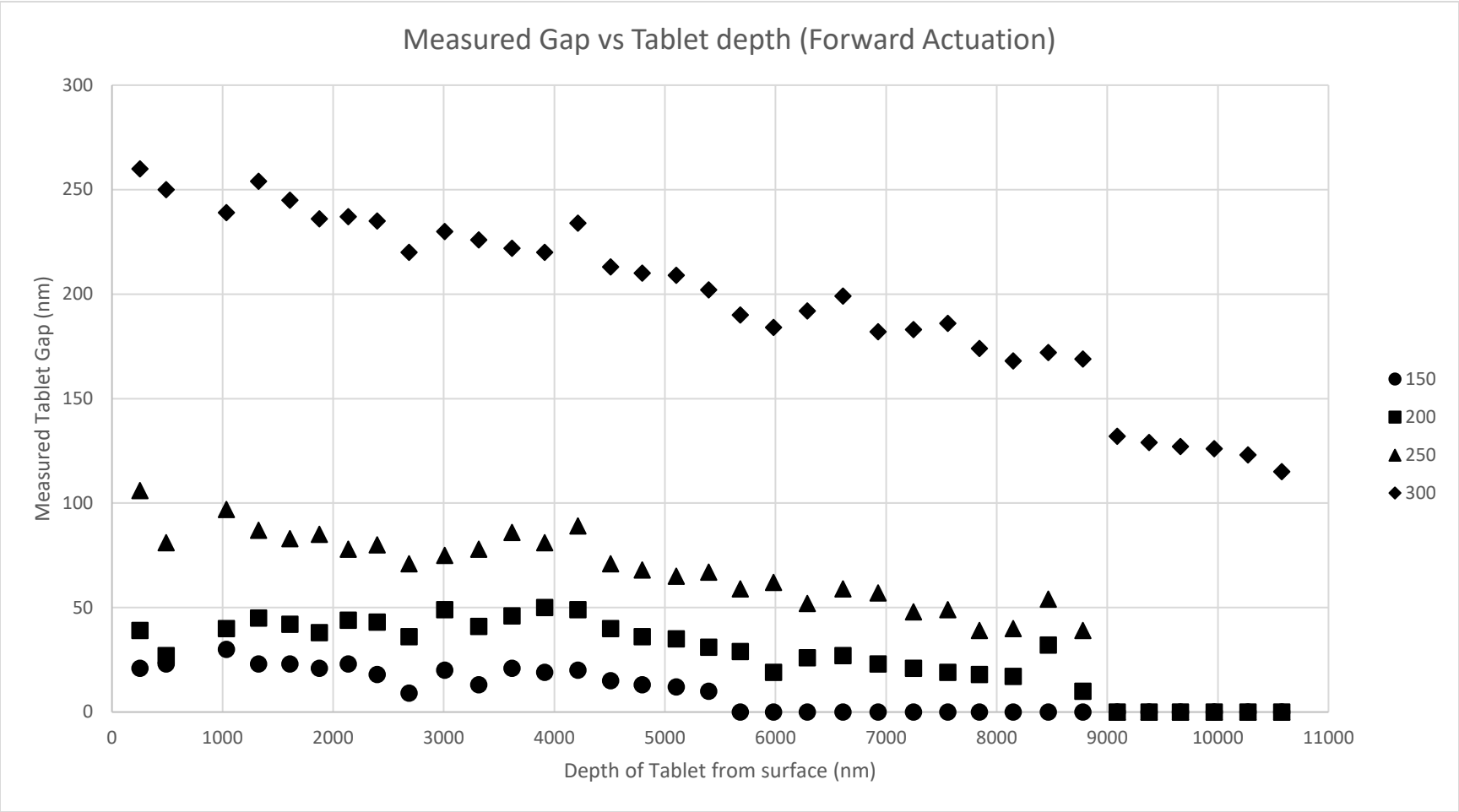

Figure 22: Graphical representation of the measurable gaps in tablets from the outermost surface (0 nm) of the nacre beam to the deepest tablet with images at a high enough magnification. These gaps were measured at the midpoint of the tablet and for actuations of 150, 200, 250, and 300 microns.

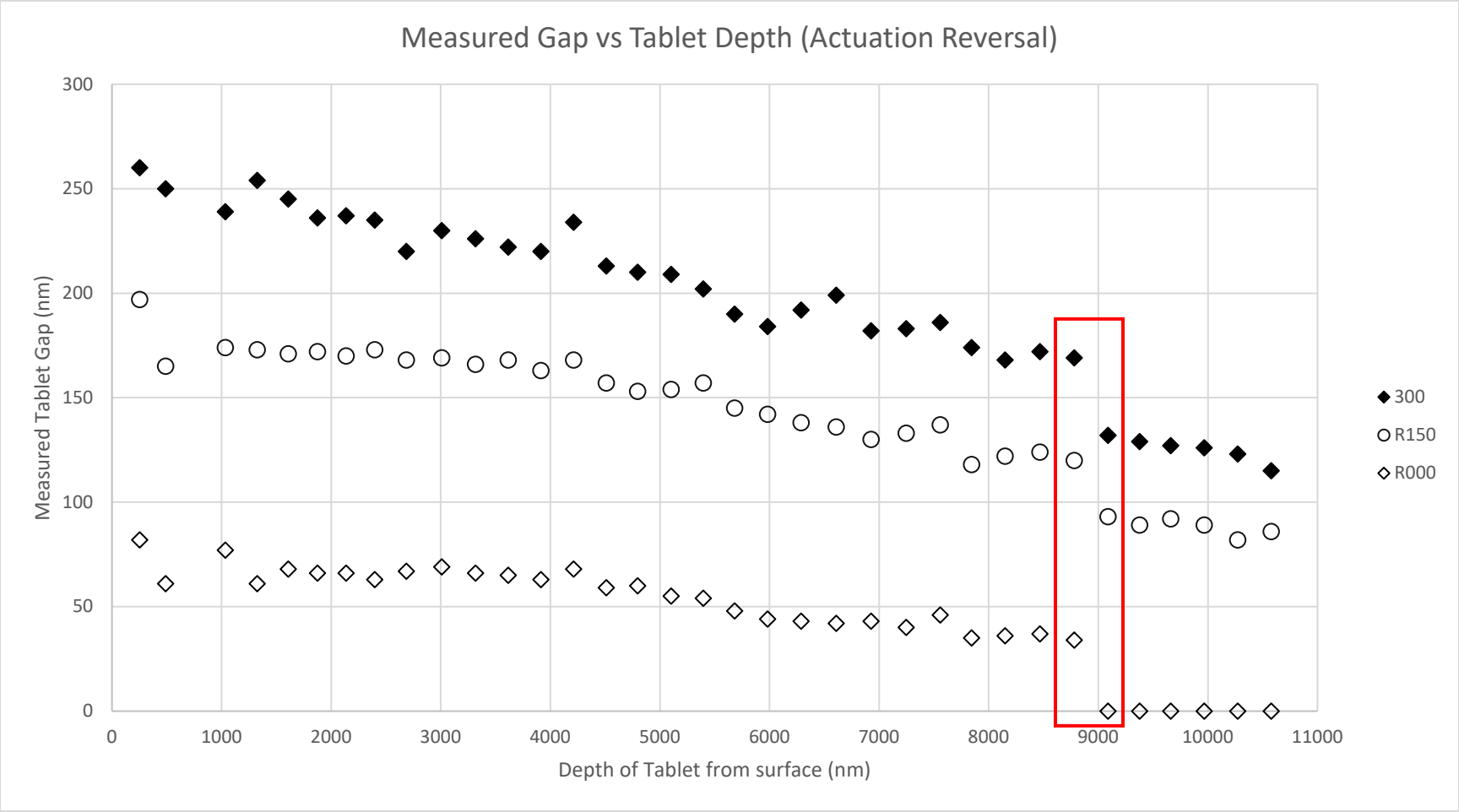

Figure 23: Graphical representation of the measurable gaps in tablets from the outermost surface (0 nm) of the nacre beam to the deepest tablet with images at a high enough magnification. These gaps were measured at the midpoint of the tablet as the actuator was reversed. The highlighted section is the portion at which the tablet gap was no longer measurable and had completely reversed.

The maximum macroscopic flexural strain for the bending of the nacre beam was calculated by using **Equation 1**, which is an equation for the flexural strain for the outermost surface of a rectangular cross section under three-point bending. Using the recorded measurements for the overall thickness of the nacre sample beam, the measurement of the support span, and the measurement of the amount of applied deflection that the shaft of the actuator applied to the beam, the maximum flexural strain at each of the stages of actuation from 50 microns of actuation all the way to 300 microns of actuation. After recording the maximum strains at the various degrees of actuation, the strain at the depth of each individual tablet gap was calculated using **Equation 2**, which was an equation that relates the calculated maximum flexural strain at the outermost surface as a ratio of the distance from the neutral plane found in the center of the beam, where the strain is zero. The neutral plane was found by dividing the overall measured thickness of the sample beam in half, and the distance from the neutral plane for each tablet was determined by taking the distance from the neutral plane and subtracting the accumulated tablet thickness for all of the tablets above it. The strains calculated for each of the tablets that images were captured of at the various stages of the three-point bending experiment were recorded and are presented graphically in **Figure 24** as a function of the tablets distance from the outermost surface of the nacre beam, similar to that of the graphs of the tablet gaps.

When comparing the graph strains at each tablet level and the graph of the tablet gaps during actuation reversal (**Figure 23**), the maximum macroscopic flexural stain above which the biopolymer fractures and the reversible sliding mechanism cannot fully recover the gap formed between the neighboring tablets can be discerned. The macroscopic flexural strains calculated for the tablet pair which were the last to have a residual gap remaining in between them after the load was released from the nacre sample and the first tablet pair to have the gaps between them be fully

resolved through the reversible sliding mechanism (highlighted in **Figure 21**) can be seen in the highlighted in **Figure 23** and **Figure 24**. The macroscopic strain above which the biopolymer fractures and the reversible sliding mechanism can no longer take place was determined to be 0.00502 or 0.502% strain.

These calculations of the macroscopic strains and measurements of the gaps formed between the tablets and recovered during the three-point bend testing of the nacre architecture have provided a broad view of the reversible sliding mechanism at large. However, this estimated global strain appears insufficient in describing how the nacre architecture is responding to the tablet sliding deformation process. In this analysis of the reversible sliding mechanism, the main factor affecting the ability of the tablets to recover the gap formed between them is the fracturing of the biopolymer connected between the tablets. The very nature of the biopolymer, by virtue of being a polymer, has been shown to have an elastic response to its deformation. The estimated global strain of 0.5% is incredibly low for a polymer, and thus subscribing such a low strain to the fracturing of the biopolymer would appear to be inadequate. This has led to a need to better describe how the biopolymer functions in the reversible tablet sliding process in a different way. To understand this mechanism on a deeper level, more information on the effects of reversible tablet sliding on the nacre architecture at the local is needed.

In order to further analyze the reversible sliding mechanism, a better understanding of the local effects of the tablets sliding relative to one another is needed. One method of acquiring the necessary information is through a post-processing technique known as Digital Image Correlation or DIC, which can be employed on captured images of the three-point bend testing of the be samples of the nacre architecture. Previously, this method has been used to measure deformations occurring on sample sizes and scales far greater than that of the nanoscale nacre architecture.

Performing DIC on this scale is a developing field and will require exploring several different methods.

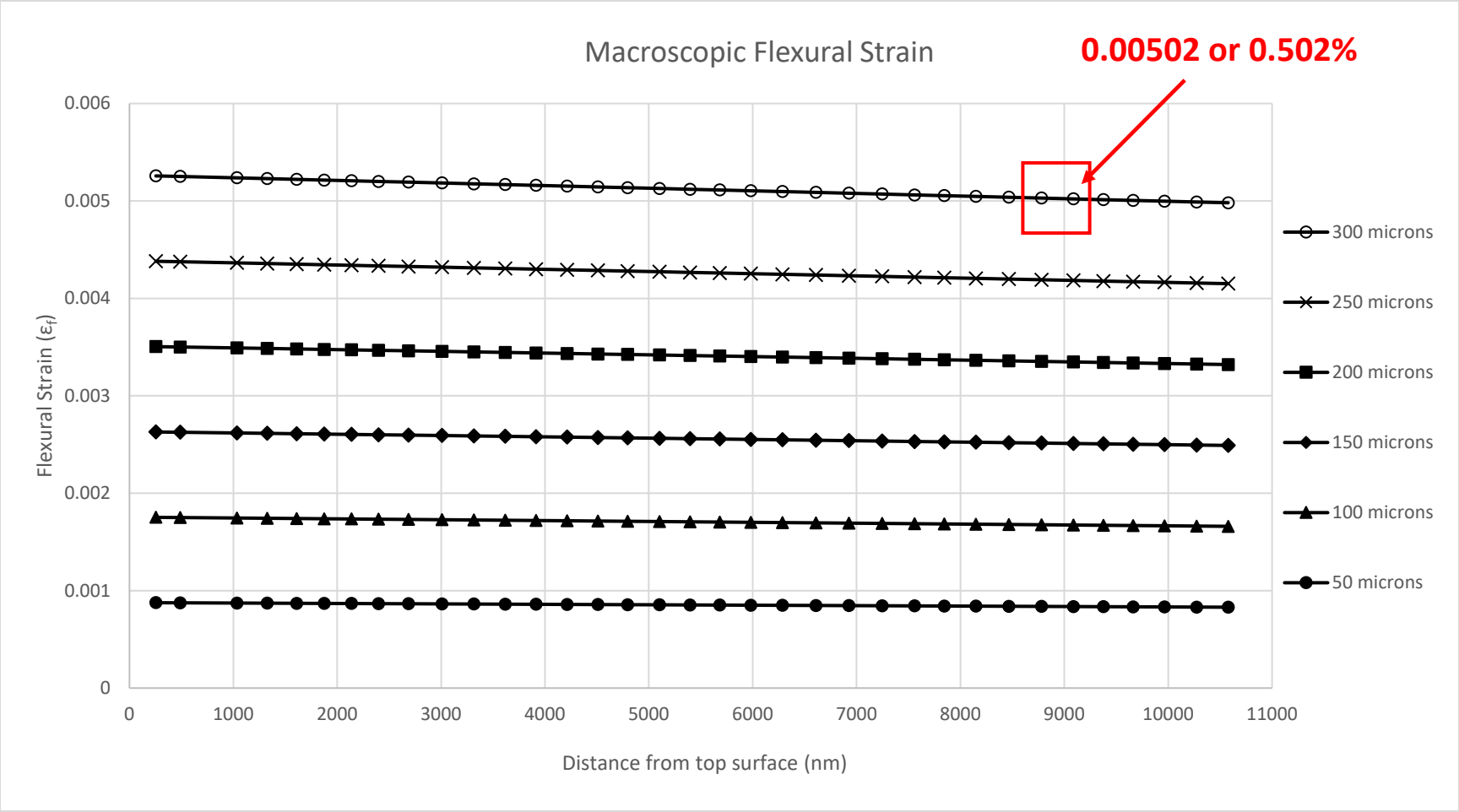

Figure 24: Graphical representation of calculated macroscopic flexural strains in nacre beam for tablets at varying depths. These strains were calculated for each of the successive actuation. The highlighted section is the strains for the last tablet to not completely recover its gap and the first tablet to completely do so.

4. Nanoscale Digital Image Correlation

4.1 Introduction

Further analysis of this mechanism is needed in order to understand it on a more comprehensive level. For this purpose, more detailed information is needed. Digital image correlation (DIC) may provide this information. DIC is an optical technique that accurately measures changes in an image in the 2D and 3D. The process involves a computer-based correlation method to obtain data by recording the motion of a speckle pattern on a specimen surface. With this, local strain as well as global deformation can be decerned from this information [44].

To perform this method of characterization, DIC requires a few things that are crucial for it to perform. The first requirement is an appropriate image capturing method. A camera with sufficient resolution is necessary to capture appropriate images of a sample under deformation conditions. The images captured of the deformation of the sample can be used to track the minute changes in the surface of the sample. This can be further expanded by using a two-camera apparatus to allow for a 3D view of the sample surface. For imaging to work on the scale of the tablets in the abalone nacre, the SEM will be the required imaging method.

Next, in order for DIC to be performed, an appropriate software for preforming the characterization is necessary. There exists several different software that are capable of performing the digital image correlation and providing the related information, each of which have different methods of tracking changes in the surface of a sample undergoing some kind of deformation or

transformation. As previously stated, the selected software for performing digital image correlation is the GOM Correlate software, due to its ease of use and accessibility.

The last thing necessary for the DIC software to track changes in the material's surface, the surface must be coated or covered in a speckle pattern that is randomly distributed and covers the surface adequately. The speckles must also be of a sufficient size, so that they can be tracked by the software. Traditional DIC is performed using paint speckles applied to the surface in various ways. However, for this to work on the nanoscale, traditional methods of speckling can't be employed. A search for an effective method in a developing field such as nanoscale DIC will be necessary.

4.2 Literature Review of Available Nanoscale Speckle Patterning Techniques

The speckle pattern is the most vital component to the method of digital image correlation, as without the pattern the software will have nothing to track and thus can't make any measurements of the deformation. In traditional DIC, the surface is speckled using paint and a special roller (**Figure 25**) that will allow for the sample surface to achieve a random pattern of uniform and appropriately sized speckles. Another method for applying the speckle on a slightly smaller scale involves the use of a paint sprayer with a fine nozzle that allows for a smaller particulate spray. While effective for traditional DIC, these methods would not allow for the DIC to be performed on the micro- or nanoscale.

Figure 25: (A) Depicted is a typical speckle pattern application. A paint roller with fine points is used to apply a randomly placed speckle pattern onto the surface of a sample.[52] (B) A potential alternative to the rolling is a paint spray method. With this, the size of speckles can be controlled by use of different nozzles and distances sprayed from sample.[53]

For this, a new strategy must be employed in order to provide a sufficient speckle pattern at this scale. This field is a developing one, and there are many preliminary methods which are developed and explored simultaneously. Several of these developing methods were explored as options for the experiments performed on the surface of the abalone nacre, and a few were selected and tested to determine viability for producing speckles at the scale necessary for imaging the tablet deformation.

4.2.1 Laser Speckle Pattern

One speckle method that was investigated involves the implementation of a laser pointed at the surface of the nacre beam. In this method the lasers light illuminates the inherent inhomogeneities

that are present in the nacre structure. The inhomogeneities on the sample surface will cause a random speckle pattern to appear on the surface that can then be used to track the minute changes in the surface of the sample as it undergoes deformation. The scale on which these inhomogeneities are illuminated is appropriate for imaging the sliding of the tablets, and thus would require the use of the SEM for appropriate imaging of the deformation.

Verho et al. [48] were able to produce this effect on the surface of a nacre beam as well as a beam comprised of a nanostructure clay/polymer nanocomposite. **Figure 26** shows a schematic set up of the laser speckling method for use on the nacre beam for three-point bending. The team was able to produce a speckle pattern on the surface of their samples and detect the changes in the sample as a failure process zone forms through the three-point bending test (**Figure 27**).

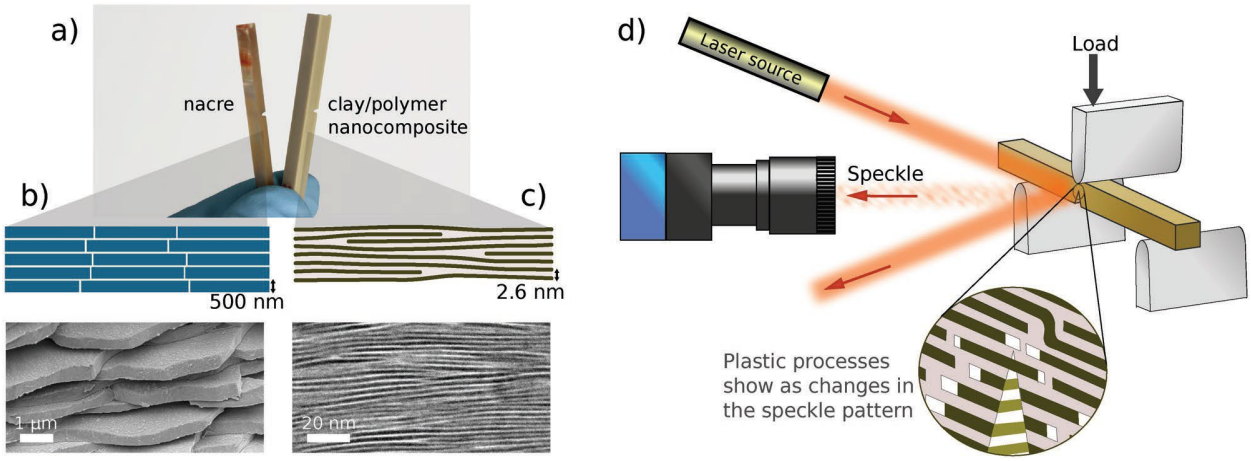

Figure 26: A) A set of notched fracture test beams of abalone nacre and nacre-inspired clay/polymer nanocomposite. B) A schematic and an SEM image of the microstructure of abalone nacre. C) A schematic and a cross-sectional TEM image of the clay/polymer nanocomposite structure. D) A diagram of the laser speckle imaging setup.[48]

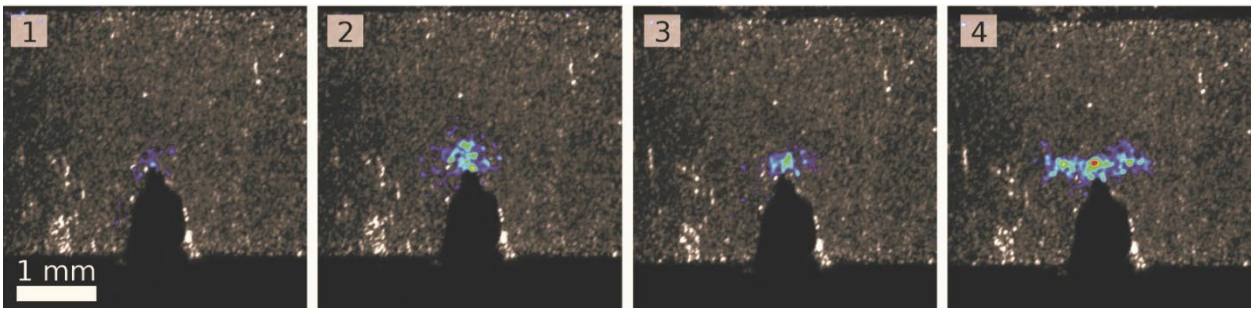

Figure 27: Image captures of the laser speckle measurement showing the gradual development of the process zone during a SEB test of hydrated nacre.[48]

While this method seems to work fairly well, attempts at recreating this setup with the SEM that was accessible to me is where the issues arose. The professional methods of reproducing this set up reached levels of effort that were both time and cost prohibitive to attempt, and any low-cost options were difficult to implement simply into the working setup of the SEM as well as the three-point bending setup that had already been used for this work. With these in mind, other methods were then explored for their effectiveness with this setup.

4.2.2 Self-Assembled Nanoparticle Surface Patterning

Kammers and Daly [49] worked on a technique of surface patterning that would allow for self-assembled gold nanoparticles to coat the surface of a sample. This will create the nanometer resolution necessary for preforming digital image correlation experiments in the SEM. This technique was originally developed for creating substrates for surface-enhanced Raman scattering (SERS). Gold Nanoparticles can be synthesized to sizes ranging from 15-136 nm for application to the surface of the samples. The nanoparticles attach themselves to the substrate surface by means of organosilane molecules. These molecules possess a pendant functional group that has a strong affinity for gold.

As seen in **Figure 28**, the gold nanoparticles are immobilized on the surface an aluminum substrate. The effective distribution of the nanoparticles across the surface would allow for DIC experiments to be performed on the deformation of these samples. These samples were tested by *in-situ* tensile testing within the SEM. The images were then put through post processing DIC and strain fields were generated (**Figure 29**).

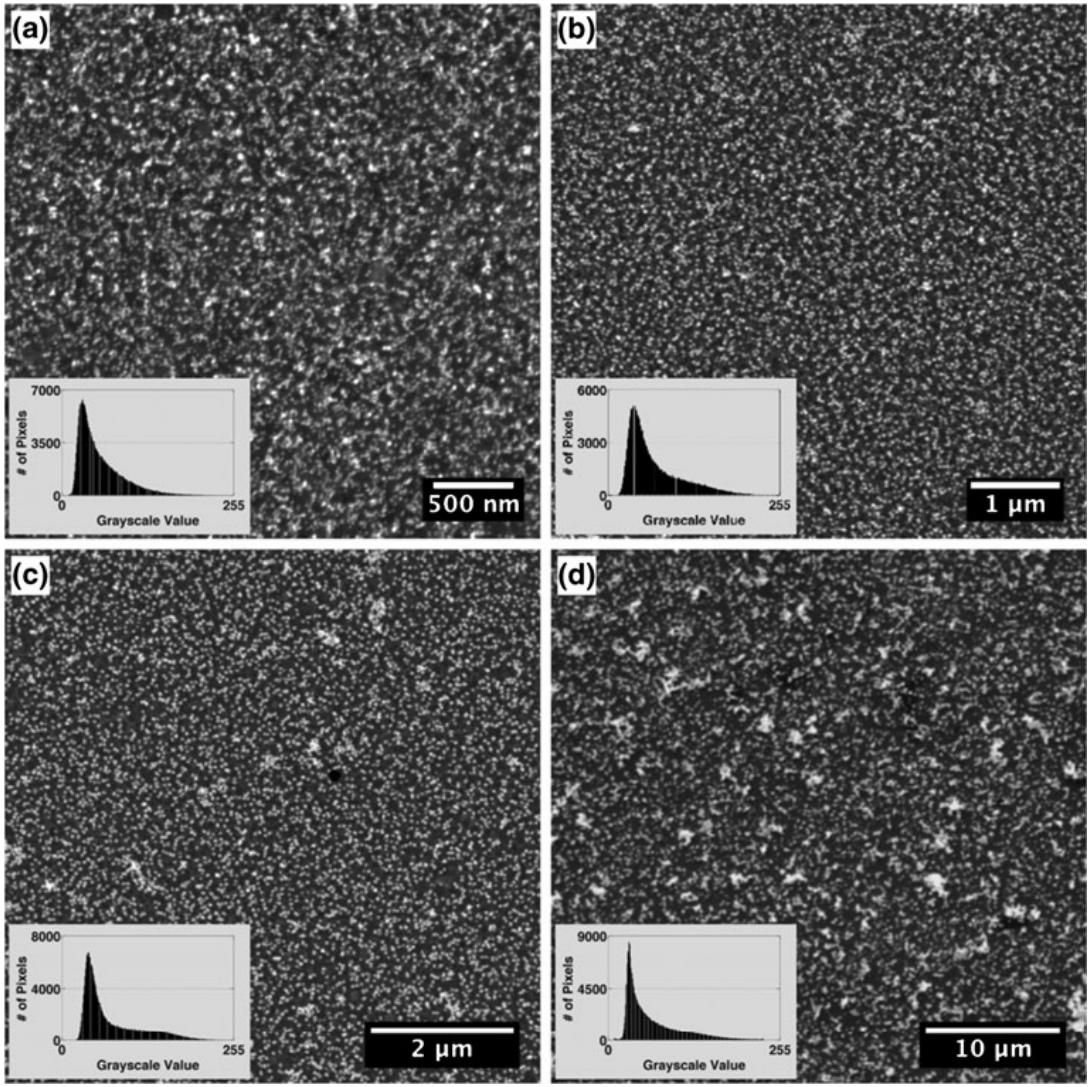

Figure 28: AuNPs immobilized with MPMDMS on the surface of a 99.99 % Al substrate. The patterns were created by soaking the substrates in (A) 15 nm diameter AuNPs for 5 days, (B) 32 nm diameter AuNPs for 3 days, (C) 48 nm diameter AuNPs for 1 day, and (D) 136 nm diameter AuNPs for 1 day. The histogram at the lower left of each image shows the grayscale distribution of the image.[49]

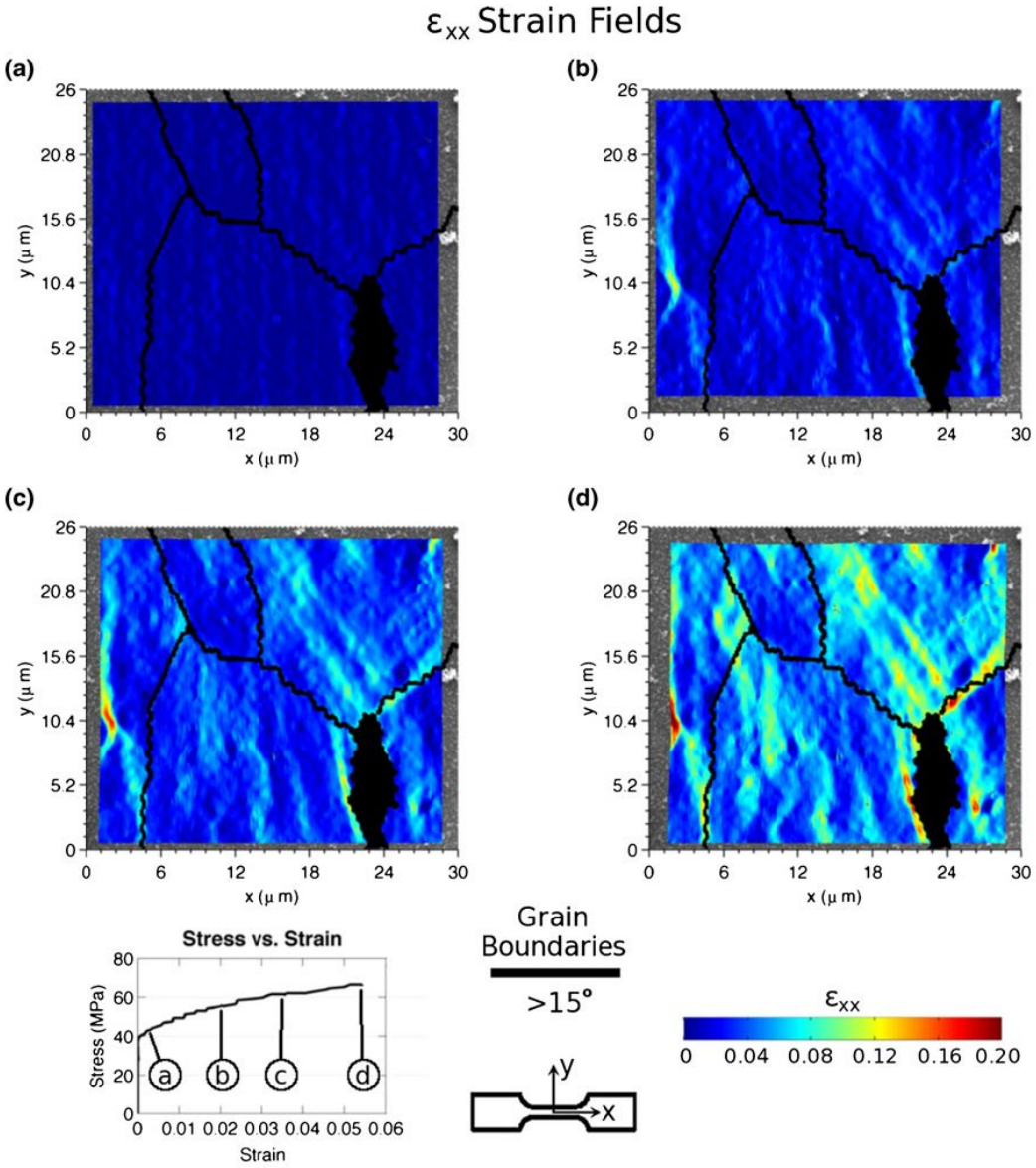

Figure 29: DIC calculated axial strain field evolution for a tensile test on 1100 Al. High strain is observed around the iron intermetallic particle at the bottom right of the strain fields. SEM parameters: 30 kV, 91pA, 12.4 mm working distance, 10 microsecond dwell, 8 image integrations, 1024×884 image size. DIC parameters: 31×31 pixel subset size, 1 pixel step size.[49]

This method, however, has some significant draw backs for use on the abalone nacre. While having the ability to synthesize gold nanoparticles and controlling the size of the nanoparticles would allow for this method to be applied to the nanoscopic realm of the abalone nacre architecture, the functionalization of the nacre surface is where this method hits a proverbial wall. In this method, hydroxylation of the surface of the samples by soaking them in a Piranha solution. The use of this on the mineral surface of the tablet structure of nacre may cause adverse effects and could potentially be detrimental to the nacre architecture as a whole. The Piranha solution could have the potential to eat away at and destroy the biopolymer in the nacre matrix. The removal of the biopolymer from the nacre matrix would prevent the nacre from undergoing the reversible sliding mechanism, making tests with the functionalized samples pointless. For these reasons, this method was deemed non-viable for use on the abalone nacre tablet samples for this work.

4.2.3 Liquid-Powder Speckle Deposition Method

Since functionalization of the nacre tablet surface is out as an option, a potential alternative would be to directly deposit the speckles onto the surface of the sample. One such method is the deposition of a powder held in a liquid slurry onto the surface of the samples. This method was explored by Mehdikhani et al. [50] on the surface of their unidirectional glass/epoxy composite material. The team went through several iterations of their experiment to achieve the desired speckle pattern on the surface of their samples. The initial slurry produced consisted of a 1 wt% suspension of alumina powder suspended in distilled water, with an equal 1 wt% of DARVAN-CN which acts a dispersal agent to prevent particle aggregation.

A drop of this solution was applied to the surface of their samples, the sample was allowed to dry, and the quality of the surface coating was assessed. It was observed that this initial 1wt% solution was far too high and caused extreme coverage of the sample in the alumina powder preventing the microstructure of the sample from being visible in the SEM images (**Figure 30 D**). To counter this, the powder was reduced to a tenth of its original weight percentage. This new solution now consisted of 0.1 wt% alumina powder and an equal portion of DARVAN-CN. A droplet again was placed on the surface of the sample, the sample was allowed to dry, and the quality of the surface was the assessed. A more disperse speckle pattern was achieved with this method, however there were still small portions of the sample that received a high degree of particle aggregation.

A final iteration of the suspension was attempted. This attempt involved cutting the weight percentage of alumina powder and DARVAN-CN again in half. This gave the final suspension an 0.05 wt% alumina powder and 0.05 wt% DARVAN-CN suspended in distilled water. A droplet of this suspension was then dropped onto the surface of the samples and allowed to dry. This process was repeated to give the sample the same amount of alumina powder as the 0.1 wt% solution. As seen in **Figure 30 F**, with the two-drop method, the sample receives a more disperse speckling of alumina powder on the surface while avoiding creating areas of increased particle aggregation.

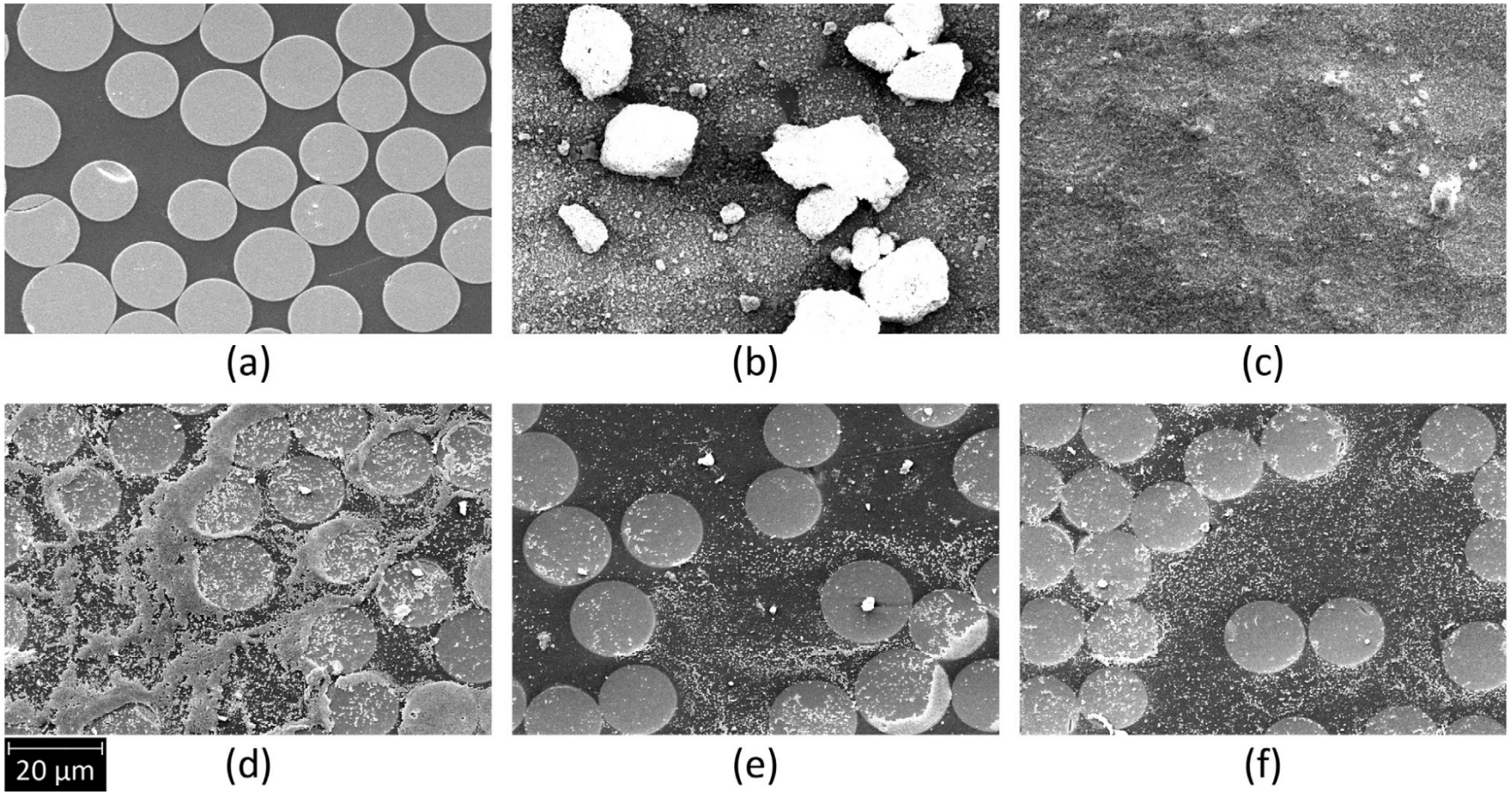

Figure 30: SEM images of (A) a bare specimen surface and (B)–(F) speckled surfaces with alumina suspensions using (B) 1 wt.% alumina, without ultrasonication and stirring, without dispersant agent; (C) 1 wt.% alumina, with ultrasonication and stirring, without dispersant agent; (D) 1 wt.% alumina, with ultrasonication and stirring, with dispersant agent; (E) 0.1 wt.% alumina, with ultrasonication and stirring, with dispersant agent and (F) twice deposition of 0.05 wt.% suspension, with ultrasonication and stirring, with dispersant agent.[50]

4.2.4 Vapor assisted Gold Thin Film Remodeling Process

In order to take images of the abalone nacre structure in the SEM, thin film of gold must be placed on the surface to create a conductive layer and allow for high resolution images. It would then be highly beneficial then if there were a process to create a speckle pattern on the surface of the samples while employing the already existing gold coating on the surface of the samples. Well, the team of Di Gioacchino and Quinta da Fonseca [45] attempted to prove that just such a thing is possible. Their goal was to produce a speckle pattern using a gold thin film placed onto the surface of a sample.

As the name would suggest, in this method, a thin film of gold is placed onto the surface of a sample and is remodeled through heating of the sample to a certain temperature and allowing a subsequently heated vapor to pass of the surface of the coated sample. Since the gold thin film is now heated, but at a point below its melting temperature, it is still solid but more free flowing than at room temperature. As the vapor passes over the surface of the gold thin film, the gold particles will flow along with it. The particles will run into one another and begin to form tiny islands of gold speckles that begin to contrast with the background of the sample. As time passes, more and more islands form, eventually creating a fully evolved speckle pattern that can be harnessed for the purposes of DIC work.

The refinement of this methodology is vital to ensuring the speckle pattern is properly generated. There were many variables that were evaluated to determine the optimal speckle pattern formation process. They include the final polishing medium, the temperature that the sample was heated to, the amount of time the process was allowed to take place, the vapor flow right over the surface of

the samples, and the thickness of the applied gold thin film. The team took to optimizing these variables one by one to ensure the method was as effective as possible.

To start this process, the team polished 304 Stainless Steel tensile wishbones in various ways. The final polishing solutions included a 0.25 μm diamond suspension, 0.05 μm Al_2O_3 suspension, an OPS suspension with a pH of roughly 7 for 10 minutes, and an OPS suspension with a pH of roughly 8 for 10 minutes. Samples using each of the final polishing methods were given a coating with a gold thin film of varying thicknesses. The film thicknesses varied from 30 nm, 50 nm, and 80 nm.

Next, the method of remodeling the gold thin film through the vapor assisted remodeling process could take place. As seen in **Figure 31**, on a hot plate, a beaker of water was placed in the center. Around this beaker the wishbone steel samples with gold thin films were placed on the surface of the hot plate. The hot plate allows for even heating of the samples, and the large surface allows for more samples to be placed upon the surface so that more samples could be processed at once.

Over the top of both the samples and the beaker was placed an even larger beaker or cup. This larger cup was propped up with a set of cup holders so that the vapor could flow out of the beaker and through the cup. As the vapor flows out of the larger cup, it passes over the surface of the samples performing the vapor assisted remodeling of the gold thin film. Various temperatures and processing times were tested on samples to determine the optimal methodology. The temperatures that were tested were between 150 ℃ up to 300 ℃ and processing times ranged between 60 and 90 minutes. The team noticed that remodeling only occurred at temperatures exceeding 240 ℃, and determined that the optimal temperature for processing their samples was at 280 ℃ with a process time of 1 hour and an average vapor flow rate 100 ml/h.

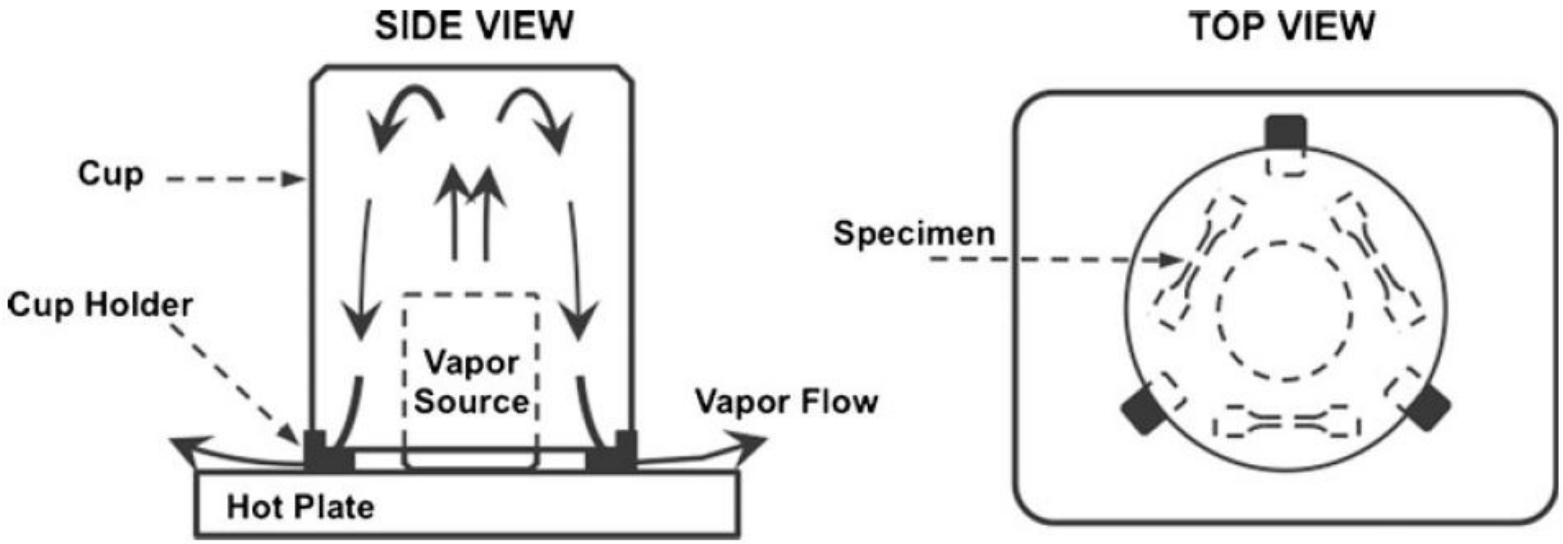

Figure 31: A diagram of the experimental apparatus used in vapor assisted remodeling process.[45]

The results of these experiments are seen here in **Figure 32**. The samples polished with 0.25 μm diamond suspension (**Figure 32 A-B**) were found to produce significantly smaller speckles but were less defined and didn't appear to create a great enough contrast with the samples background, while the samples polished with the 0.05 μm Al_2O_3 suspension (**Figure 32 C**) formed irregularly agglomerated speckles. The OPS pH~7 and OPS pH~8 samples (**Figure 32 D-I**) yielded more consistent and fruitful results. The OPS~8 samples at 50 and 80 nm thicknesses (**Figure 32 G-H**) yielded larger speckles with a greater spacing between them with the thick film creating further spacing, and with an increased polishing time (**Figure 32 I**) the spacing appears to be unaffected but the speckles yielded were drastically reduced.

The OPS~7 samples appear to have produced some of the best speckle patterns for use in DIC works. The 30 nm thick sample (**Figure 32 D**) appears to not create large enough particles or with high enough contrast against the sample background. The 50 and 80 nm thick samples on the other hand produced a densely packed speckle patterns with fairly uniform speckle sizes that would allow for DIC to be performed. The 50 nm thick sample (**Figure 32 E**) produced a speckle pattern consisting of fine speckles with a decent level of contrast between it and the sample background. The 80 nm thick sample (**Figure 32 F**) produced larger uniform speckles with the same level of density. Depending on the needed speckle size, either of these preparation and process methods would be acceptable for DIC work.

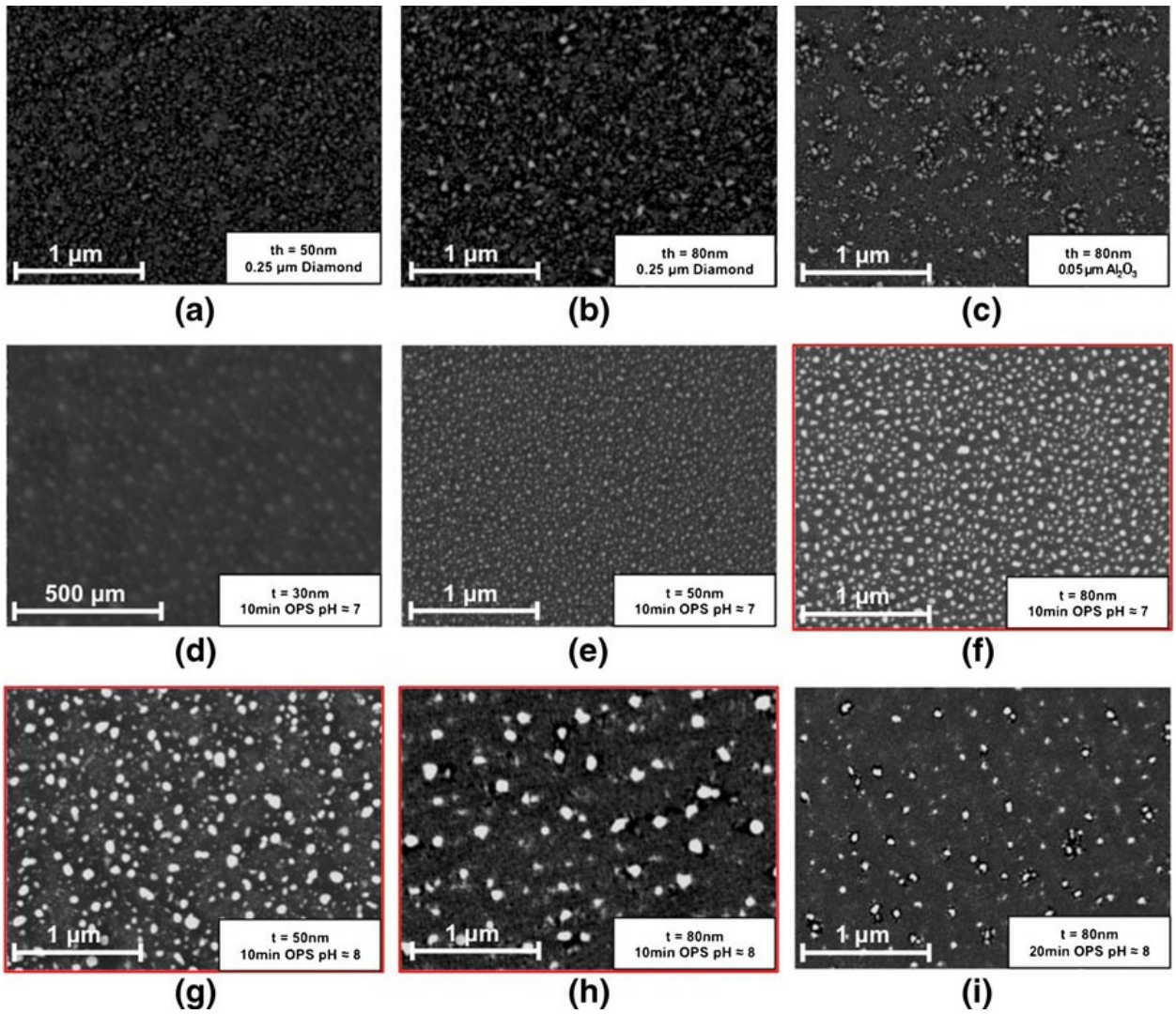

Figure 32: Speckles patterns formed after 1 h vapor exposure at 280 °C using apparatus in Fig. 1(A) following distinct surface finish and gold film deposition. 0.25 micron diamond finish and 50 nm and 80 nm film thickness (A), (B). 0.05 micron alumina finish for 80 nm film thickness (C). 10 min of 0.05 micron colloidal silica polishing with a 1:30 volumes diluted solution (pH≈7) for 30 nm 50 nm and 80 nm film, (D), (E), (F). 10 min of 0.05 microns colloidal silica polishing with a 1:10 diluted solution (pH≈8) for 50 nm and 80 nm film (G), (H). 20 min 0.05 microns colloidal silica polishing with a 1:10 diluted solution (pH≈8) for 80 nm film (I). Patterns most suitable for plastic strain mapping with sub-micron resolution are highlighted in red. [45]

4.3 Speckle Pattern Method Testing

Two methods were selected as viable test methods for producing a speckle pattern on the surface of the abalone nacre beam samples for use in DIC imaging with three-point bed testing, the liquid-powder deposition, and the gold thin film remodeling process. Each method was tested with the sample beams to determine the viability. Both methods presented their own challenges and difficulties in their implementations with the nacre structure. There was however a clear favorite method for producing an effective speckle pattern.

4.3.1 Nacre Beam Tests with Liquid-Powder Deposition Method

When performing initial experiments with liquid powder deposition method, some interesting difficulties presented themselves that were unforeseen. Initial experiments were performed with the 0.05 wt% double drop wetting method. After applying the second drop to the surface and allowing it to dry, the samples were taken into the SEM for evaluation of the speckle pattern on the sample surface. The sample surface appeared to have no significant speckle pattern on it. This lack of patterning led to a few repeat attempts at this concentration level, yielding similar results.

After these failed attempts, the concentration of the alumina powder was increased to 0.1 wt% in an attempt to have a larger proportion of alumina in the droplets, giving a better chance of surface patterning to occur. Initially, only a single drop was applied to the surface and allowed to dry. This yielded the same results as the 0.05 wt%. Next, a second attempt with the 0.1 wt% was performed,

this time with a double drop method. This method too yielded a similar lack of results in patterning the surface.

It was at this time that an evaluation of the deposition method was performed. Looking at the samples when the droplets were applied, only a finite amount of the droplet actually remained on the surface of the cross-sectional side of the sample. The vast majority of the droplet spilled over the sides and onto the surface of the carbon tape used to hold it upright. Due to the extremely thin nature of the nacre beams (roughly 350 microns in thickness) there is not a large amount of surface area for the droplet to wet. Thus, only a finite amount of an already finite amount of alumina actually had a potential to make contact with the sample surface. It was with this revelation, as well as the success of another method, that led to abandoning this method.

4.3.2 Nacre Beam Tests with Gold Thin Film Remodeling Method

For this method, several variables were taken into consideration to ensure success with creating a speckle pattern on the surface of the nacre structure. The first was the temperature at which the samples were heated, especially with relationship to the temperatures effect on the biopolymer matrix that is laced throughout the nacre structure. The largest component of the biopolymer is the β-chitin which has been found to have a estimated melting point greater than 300 ℃. So, to prevent a breakdown of the biopolymer, temperatures were kept below 300 ℃ while performing this method. Various temperatures were tested, and it appears that temperatures around 240 ℃ were the most optimal for producing speckle patterns from the gold thing films applied to the nacre beam samples.

The set up for performing this technique can be seen in **Figure 33**. The small beaker of water is placed in the center of the hot plate. The hot plate was heated, and the water was brought to a boil. Using an Omega Digital IR-Pyrometer (**Figure 34**), the temperature of the hot plate at the locations at which the samples would be placed was measured to ensure the samples would be heated to an appropriate temperature. The samples were then placed at these locations, marked by a sharpie. A larger beaker was placed over the top of both the small beaker and the samples. The large beaker was propped up by these small disks which were produced by compressing mounting powder in a mounting press. This is to allow the vapor to flow through the bottom of the larger beaker and subsequently over the surface of the samples. This process was performed for a time varying between 60 and 90 mins. Several challenges presented themselves during this process, and unique solutions were produced to meet them.

One of the first challenges met while performing this technique was the vaper flow rate. Depending on the location of set up, the amount of airflow in the room could affect the flow of the vapor through the bottom of the large beaker. Without a proper flow of the surface of the sample, the remodeling process cannot occur. To combat this problem, a fan was placed in front of the hot plate in a way depicted in **Figure 33 C-D**, with the front of the fan facing away from the hot plate and the back of the fan facing the hot plate. This allows of the vapor to be pulled from the beaker at a much more gradual rate, as opposed to the rate of the fan blowing the vapor across the surface.

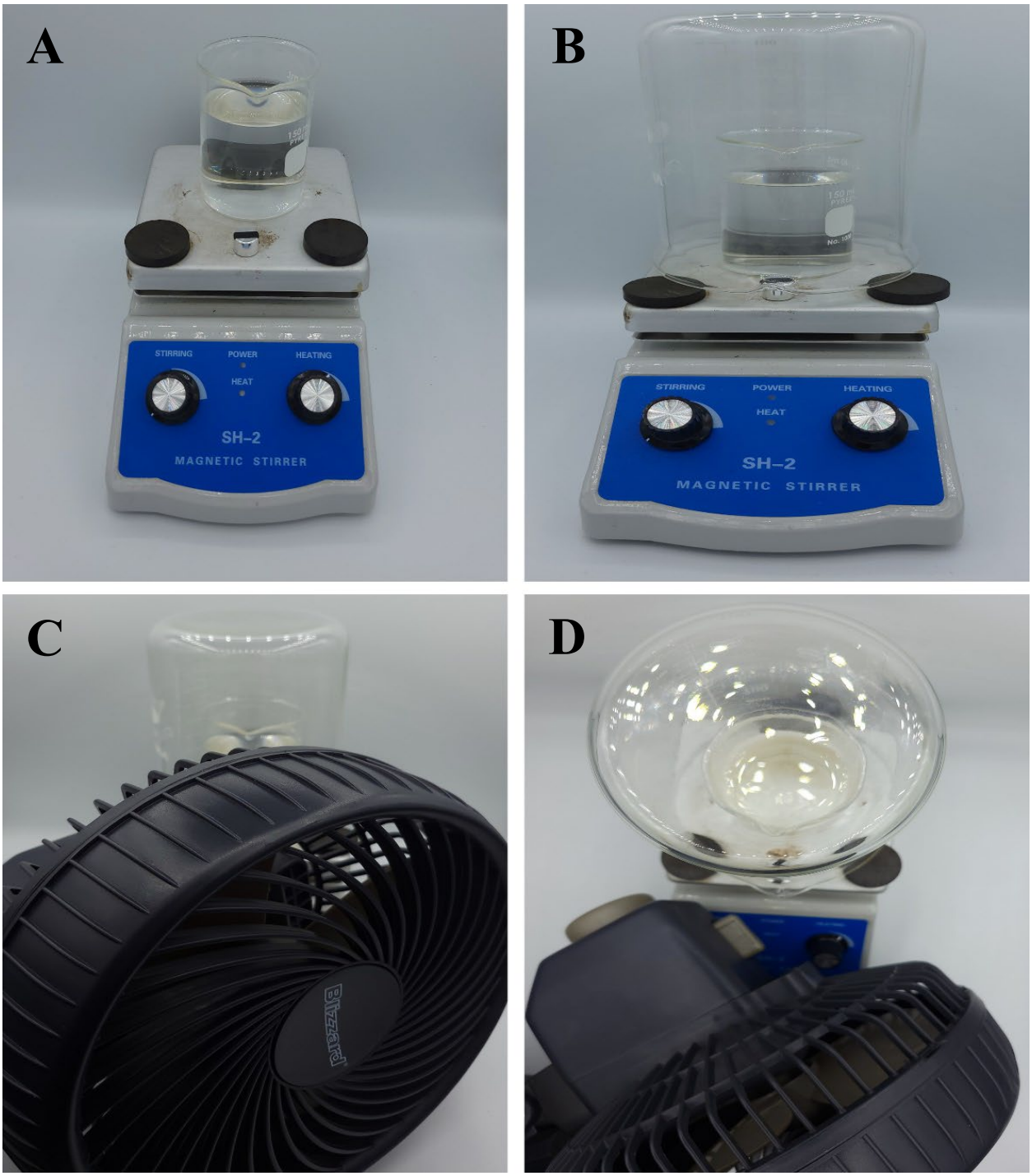

Figure 33: Experimental setup for vapor assisted thin film remodeling process. (A) Hot plate with beaker and sample mount resting in position. (B) Hot plate with larger beaker placed over sample and vapor source. (C) Hot plate with fan placed in front of it to assist in the vapor flow rate. (D) Vertical view of hot plate and fan set up.

Figure 34: Omega Digital IR Pyrometer used to confirm the temperature of the surface of the hot plate.

The next challenge was in placing the samples onto the hot plate. The samples needed to sit in a way as to allow the vapor to pass over the cross-sectional side of the nacre beam where the gold thin film is placed. Due to the small and thin nature of the samples, they could not just be placed directly onto the surface of the hot plate as they would immediately fall over. The initial solution was to place a piece of double-sided carbon tape onto the surface of the hot plate to mount the samples on vertically so that the cross-sectional side was exposed. This method was effective initially and allowed for the samples to be mounted during the remodeling process. However, after multiple uses of the carbon tape attached to the hot plate, the adhesion would wear down and samples began falling over during the remodeling process or not adhering to the tape. The removal of the tape also proved both difficult and messy in order to replace it with fresh tape. Two alternative methods were devised to combat this issue.

The first alternative method was the use of conductive carbon tape. As it is not double sided, a strip of the tape was placed on the hot plate in reverse so that the adhesive side faced upwards. This allows for the samples to be mounted on it, allowing the cross-sectional portion of the sample to face upwards. The ends of this strip of tape was then held down by two smaller pieces of tape. This method appeared effective in the beginning of the remodel process, but as time passed, the adhesive on the tape became too fluid and the samples began to fall over, preventing the vapor from contacting the cross-sectional portion of the beams. For this reason, this method was scrapped for a second alternative. In this method, the carbon tape was placed onto the surface of a 12.5 mm aluminum puck and the samples then mounted onto that. When the carbon tape would wear down and degrade, it could easily be placed into acetone do dissolve and remove the carbon tape and replaced with a fresh piece of tape or be replaced by a second puck with a fresh piece of tape on it.

After these challenges were overcome, it was time to start experimenting with varying the length of time that this method was performed as well as the thickness of the gold film applied to the surface. Initial attempts found the best speckle patterns was produced with samples having an 80 nm thick layer on the surface that underwent a 90-minute remodeling process. The 50 nm samples only produced sporadic speckling and not in the areas that were most vital to three-point bend testing, i.e., the outer edges of the cross-sectional side of the sample where tablet sliding is seen to occur during the testing. The 80 nm samples produced some promising speckle patterns on the abalone nacre samples.

There were some inconsistencies with theses samples. It was noticed that samples that were placed on the sides of the beaker didn't appear to consistently produce any speckles, so samples were kept to the front of the beaker. There were also cases of over speckling, where the gold particles would pool in a specific area, blocking all view of the sample beneath. This led to a reduction in the processing time from 90 minutes to 60 minutes. The final step in refining this process involved the placement of the sample relative to its position between the smaller beaker and the larger beaker. Some samples that underwent the processing were placed closer to the small beaker than others. It was noticed that the ones that were placed closer to the beaker either produced very little e speckling and even sometimes no speckling at all. Conversely, the samples that were placed closer to the larger beaker produced speckles consistently as well as higher quality speckles, with the best speckles being produced on the samples placed right at the edge of the beaker. So now all future attempts at performing the vapor assisted gold thin film remodeling method would be performed for 60 minutes at temperatures of roughly 240 ℃, on samples with 80 nm thick gold thin films.

Figure 35 depicts a sample beam of the nacre architecture with an appropriate amount of speckling applied to the surface through the gold-thin film application as previously described. Once the

speckle pattern was applied to the surface of the sample of the nacre architecture, images were captured of areas that were seen as having a sufficient amount of speckling nearest to the outer most surface of the sample beam. These images were then taken and uploaded to the GOM Correlate software and had a surface component applied to it to analyze the quality of the speckle pattern that was applied to the surface of the sample. In general, for the GOM Correlate software to appropriately track any amount applied speckle pattern on a sample, a surface pattern quality of above 2 on the surface pattern quality scale is needed as this will allow the software to analyze subsequent deformation images properly. Looking at **Figure 36**, the surface component applied to the surface of the sample image with an applied speckle pattern is above 2 for the entirety of the imaged surface so this area is deemed appropriately speckled for further testing and imaging in order for digital image correlation of the deformation process of this sample area to be properly performed.

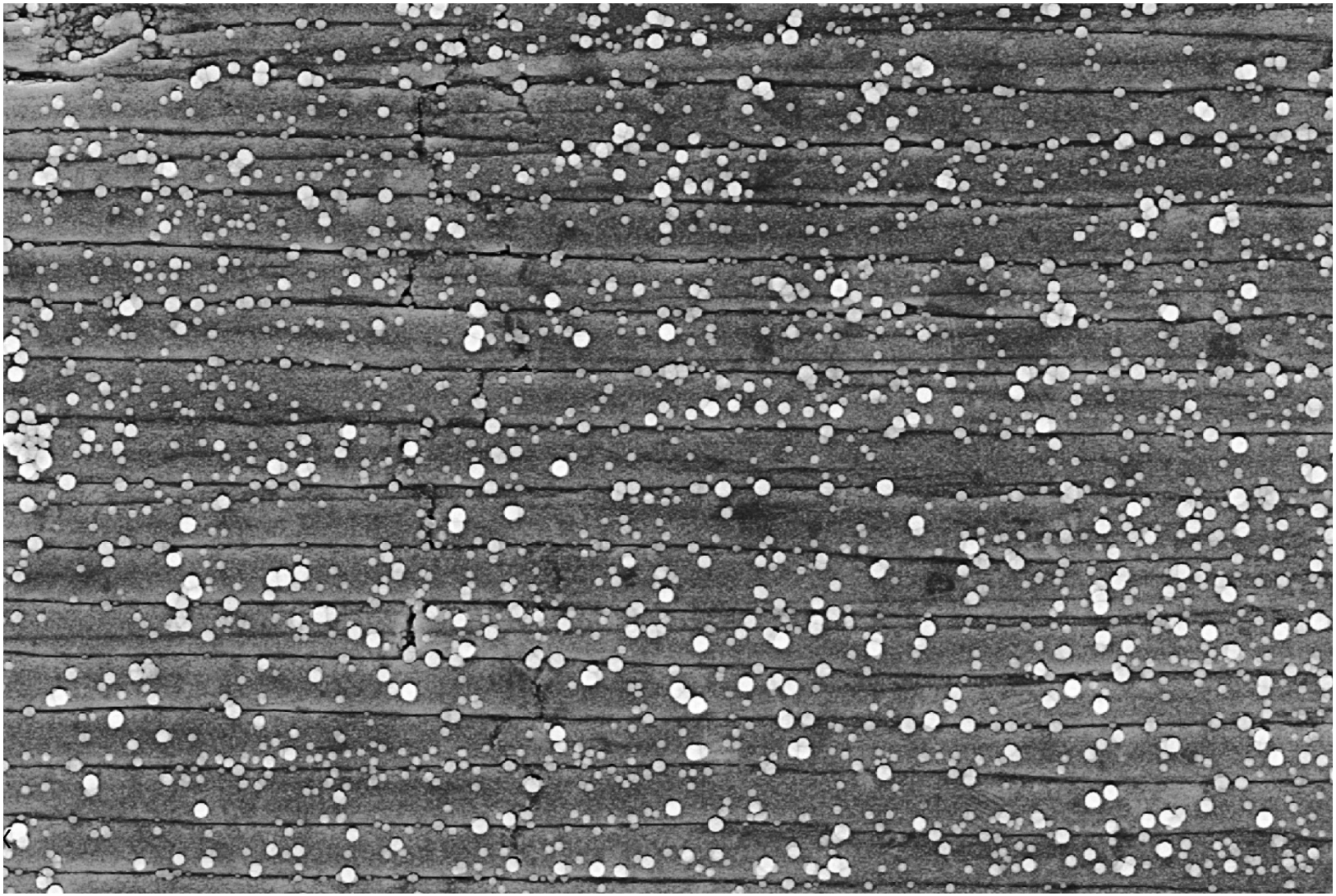

Figure 35: Image of nacre architecture with a sufficient speckle pattern applied to the surface of the cross-sectional surface of the sample beam using the gold thin-film remodeling technique

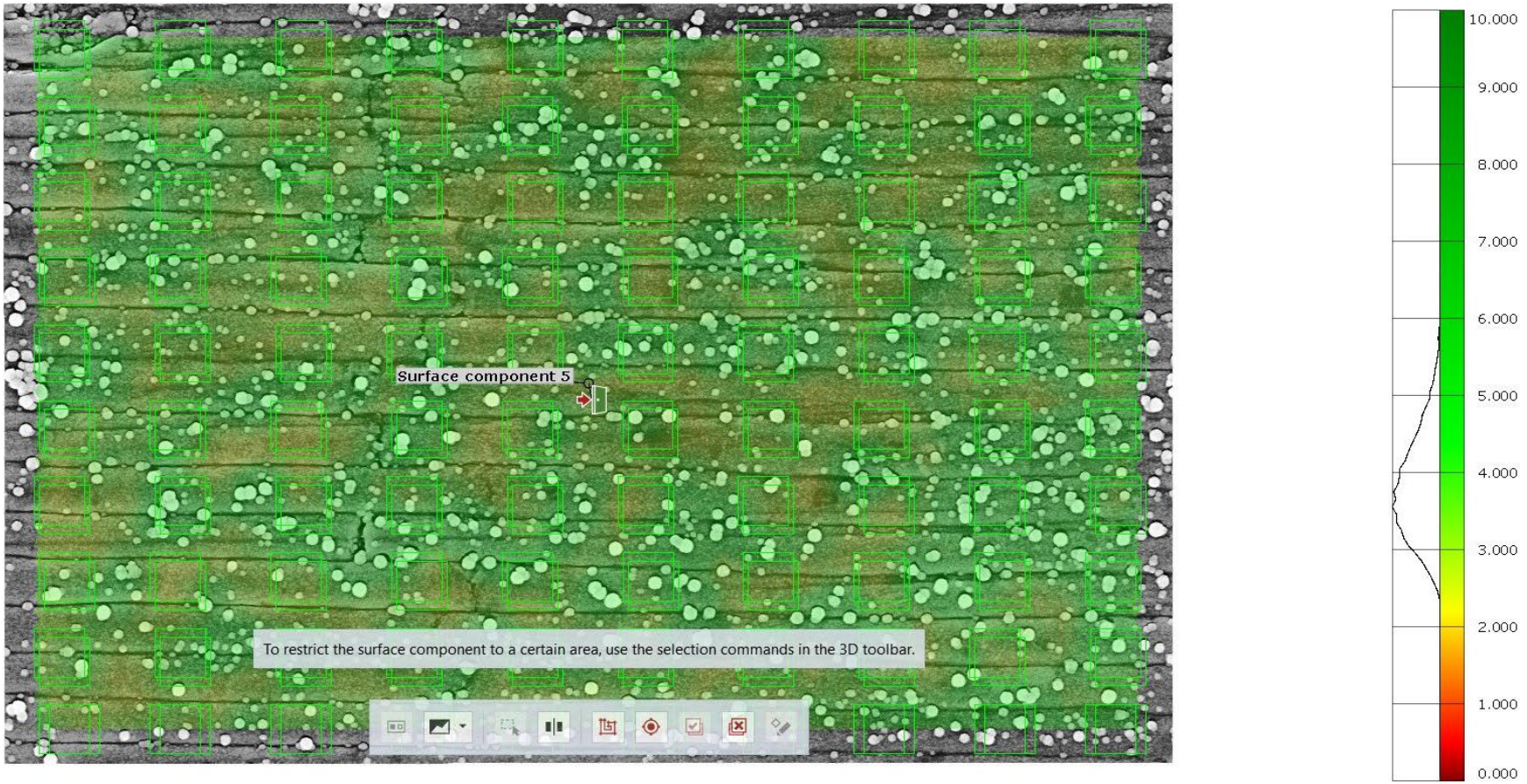

Figure 36: Image of speckle pattern on the nacre architecture being assessed by GOM Correlate for quality of pattern and the software's ability to track the applied pattern.

4.4 Three-Point Bend Mechanical Testing of Nacre Sample Beams with Applied Speckle Pattern

In order to perform digital image correlation on the nacre beam samples, first nacre sample beams with a sufficient speckle pattern applied to the surface of the nacre architecture would need to undergo three-point bend mechanical testing. As with the previous three-point bending, samples were placed in the three-point bending apparatus and placed inside the SEM. The shaft of the actuator was advanced incrementally until the head of the shaft appeared to make contact with the sample beam. A 50-micron advancement and reversal of the actuator shaft was performed to confirm the initial contact point of the head of the actuator shaft and the sample beam. The actuator was then advanced 50 microns and the beam sample was carefully scanned for signs of tablet sliding occurring in the nacre architecture. The process of advancing the actuator 50 microns at a time and scanning the sample beam for signs of tablet sliding was repeated until the signs of tablet sliding was detected in the nacre architecture.

Following this, the actuator shaft was returned to the point of initial contact and the sample beam was allowed some time to respond to the removal of the load. After some time had elapsed, images were captured of the area of interest where tablet sliding had initial been detected in its undeformed state. The shaft of the actuator was then advanced 20 microns, the position of the stage was adjusted until the area of interest was relocated, and images of the area were captured. This process was repeated until the actuator shaft had been advanced to 240 microns. The actuator shaft was then reversed 20 microns, the position of the stage was adjusted until the area of interest was relocated, the nacre beam was allowed some time to respond to the load removal, and images of the area were captured. Again, this process was repeated until the nacre beam had been returned to its undeformed state. The decision to advance the actuator 20 microns at a time as opposed to

the 50 microns as was the case with the initial three-point bend testing of the nacre beam samples was to allow for more images of the nacre architecture to be captured at a wider variety of bending stages.

Once the images were captured and compiled, they were taken to be processed in the GOM Correlate software and undergo digital image correlation. To start with, the images were first uploaded into Photoshop photo editing software, which allows for batch editing of images to help along with this process. The black bars at the bottom of the captured images which provide information such the magnification, working distance, and scale bar which were provided by the SEM image capturing software needed to be removed as they were found to interfere with and confuse the correlation software. After cropping the scale bars out of these images, the images were then aligned with one another. This alignment was performed to aid the correlating software in preforming the digital image correlation. Since the images were not always taken perfectly at the exact same location each time, aligning these images would help to reduce the amount of time required to run the digital image correlation on these images using GOM Correlate. It would also ensure that any report images that were produced from the correlation software would be uniform and show the same area of the sample.

The alignment was initially performed using the built-in auto-align feature of the photo editing software, making sure to select the reposition only option as the other methods would cause the images to become distorted. After the auto-alignment was performed on the images, a manual alignment was executed to confirm the images were properly aligned as best as possible. A set of speckles near the bottom-center of the area of interest in the images was selected as the point of alignment for the captured images. Once each image was aligned to the selected speckle, the sides of the images were cropped to make them all a uniform size. The images were then exported as

individual files, these files were then renamed as the GOM Correlate software required the files be named in a specific way. The GOM Correlate software required that imported images have their file names formatted with a number at the end. The best way to format the naming of these images was to name them with chronological numbers. Starting from the initial undeformed image being named as 1, and each subsequent image of further bending and unbending of the nacre beam was named in chronological order. After completing all of the proper formatting for use in the GOM Correlate software, the images were finally imported into the software so that digital image correlation could be performed on them.

4.4.1 Three-Point Bend Testing with Sufficiently Speckled Sample

After many attempts at performing three-point bend testing on samples with a speckle pattern applied to it, a sample beam with a sufficient amount of speckling on the outer surface produced signs of tablet sliding that was detected in an area with enough speckles in order to perform digital image correlation. **Figure 37** shows the nacre architecture of the sample beam with the speckle pattern applied to the surface of the sample. The outer most tablets, seen in the upper portion of the sample image, had some residual damage in it likely caused by the polishing process. This portion of the nacre architecture would likely not provide images of tablet sliding that could be used for the purpose of performing digital image correlation. For that reason, images of the nacre architecture below this area (highlighted in **Figure 37**) were captured during the tablet sliding process.

For this three-point bend test, the nacre beam was affixed to the mounting stage of the three-point bend apparatus and loaded into the SEM. The shaft of the actuator was advanced and reversed as described previously until the initial contact point was confirmed. Images of the undeformed state of the nacre beam were captured at this time. The shaft of the actuator was then advanced 20 microns, after which the stage was repositioned so that the area of interest was in view again, and images of the nacre architecture were captured. This process was repeated until the actuator shaft had reached 240 microns. After images were taken of the nacre architecture at this stage, the actuator was reversed 20 microns, an amount of time was allowed to elapse for the architecture to respond, and images were captured. This process was again repeated until the actuator had returned to the point of initial contact. After all of the images were collected and processed, the images were imported into GOM Correlate and underwent digital image correlation.

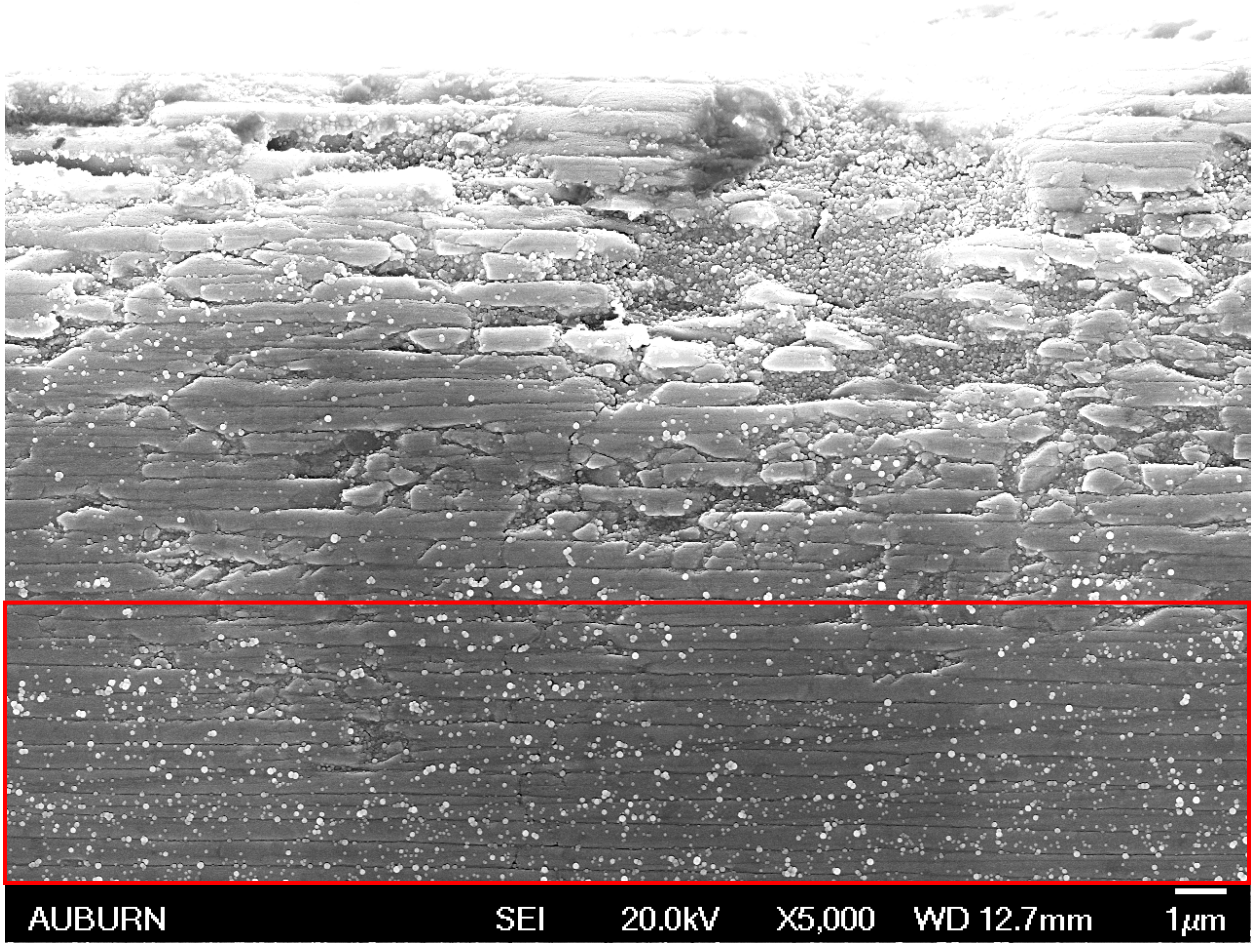

Figure 37: A tablet sample with a sufficient speckling pattern placed on it. The upper edge of the sample at the location where sliding was detected had debris and charging issues on it, so images for sliding where taken bellow in the highlighted region.

4.4.2 DIC Evaluation of Speckle Pattern

To begin performing digital image correlation on the deformation images of the nacre beams, first thing that must be done to the images is generating a surface component as an overlay on the images of the three-point bend test images that were captured. The GOM Correlate software offers various options for surface components, but the standard surface component is the best for these purposes as it allows for the necessary strain measurements to be performed when it is applied to the sample images. The local effects are the most crucial aspect of this study and selecting the best possible variables to maximize the information that can be determined from applying digital image correlation is very important.

There are two main variables that can be controlled when producing the surface components, the facet size and the point distance. The point distance was the easiest variable to pin down to an appropriate level. The smaller the point distance, the more local information that can be discerned from the software calculations. GOM Correlate has suggested that the lower limit of the functional point distance is 20% of the facet size. This allows for an optimal balance between the amount of information that can be discerned, the number of facets placed on the surface, and the amount of time necessary to perform the calculations.

The more difficult variable to sort out was the facet size. As stated earlier, the larger facet size produces a surface component that is worse at detecting the local effects but better at performing accurate coordinate measurements. The inverse is true for smaller facet sizes, where the smaller facet sizes are better at detecting local effects but are worse at coordinate measurements. For the images captured of the nacre sample beam with an applied speckle pattern subjected to three-point bend testing, four surface components with varying facet sizes and accompanying point distances

were placed onto the deformation images for calculations. These surface components included a 50-pixel facet size with a 10-pixel point distance, a 100-pixel facet size with a 20-pixel point distance, a 150-pixel facet size with a 30-pixel point distance, and a 200-pixel facet size with a 40-pixel point distance.

Figure 38 shows the various surface components as they are being created overlayed onto the deformation images. The area around the tablets sliding was selected to ensure the calculations focus on this area. As the pixel size increases, more and more area in each individual facet is overlapped by neighboring facets. On the right side of the images in an assessment of the pattern quality as it relates to the strength of the stochastic pattern inside the selected facets. The 50-pixel facets (**Figure 38 A**) have the largest range of pattern quality band where the 200-pixel facets (**Figure 38 D**) has the tightest range. This increase in pattern quality is due in part to the overlapping area of the increased facet size. While this helps to "smooth" the quality of the surface component, this is also what leads to the diminishing of the local effect measurements. The area covered by the various surface components changes due to the size of the facets, with the 50-pixel facet reaching the most amount of tablet gaps and the 200-pixel facet reaching the fewest.

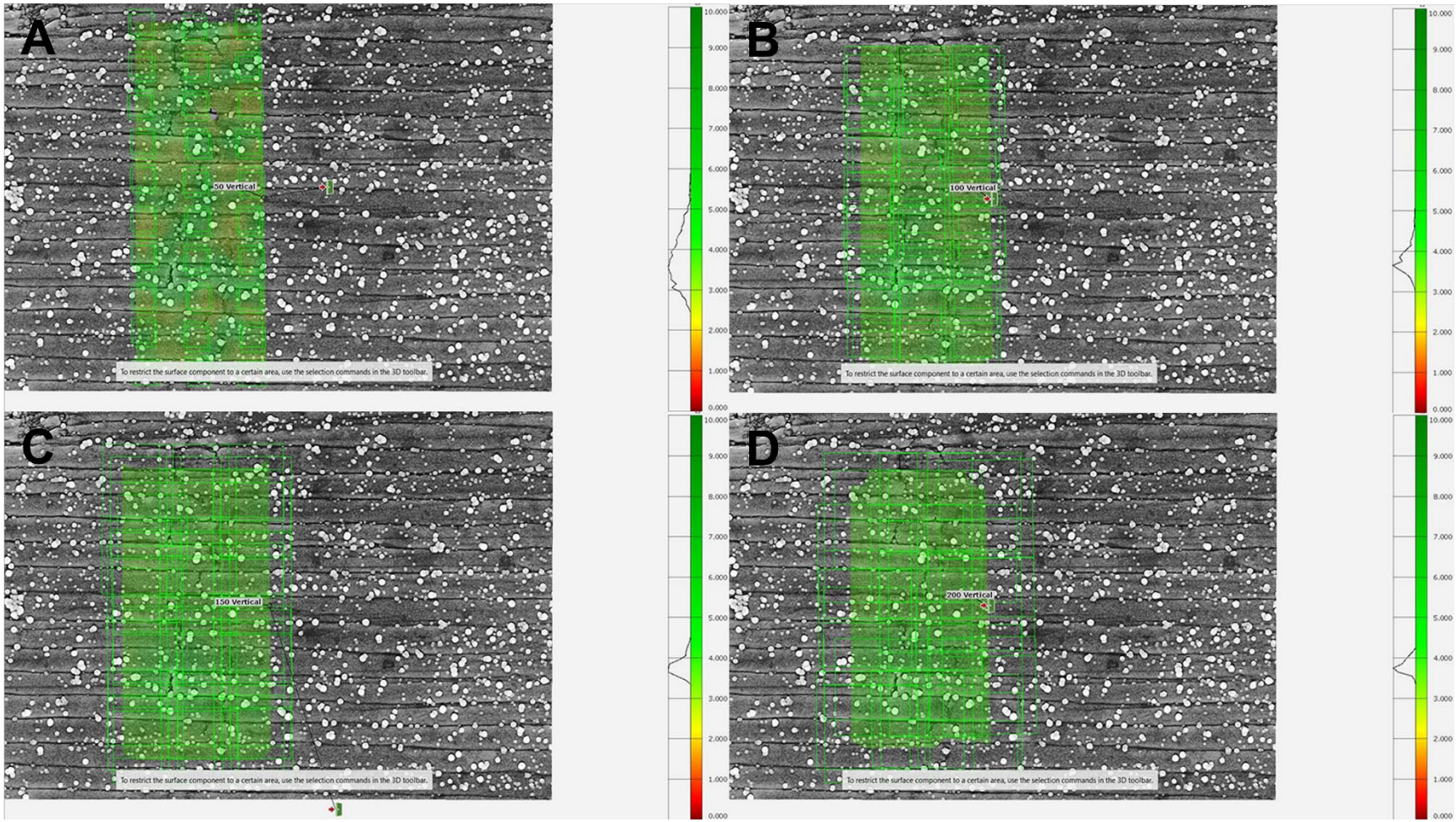

Figure 38: Images of the various surface components lain over the deformation images using the GOM Correlate software. Depicted are the (A)50-pixel facet size, (B) 100-pixel facet size, (C) 150-pixel facet size, (D) 200-pixel facet size.

To assess the quality of each surface component, calculations of strain in the x-direction for each surface component were performed. The strain was measured with respect to the reference stage which is the non-deformed initial image. **Figure 39-Figure 47** show the various surface components with the strain measurement images overlayed on top at different stages of deformation.

Looking at the strain calculations for the undeformed image and the early stages of deformation (**Figure 39-Figure 41**), all of the surface components behave fairly similarly. The 50-pixel facet component has much more localized view of the strain variations as indicated by the color variations in the strain measurements in the strain image at 20 microns of actuation (**Figure 40 A**), whereas the larger facet sizes show a more even color variation and even no color variation at all for the 200-pixel facet component (**Figure 40 D**). At 100 microns of actuation (**Figure 41**), all facets show the tablets are undergoing a tensile strain, indicate by the green coloring in the x-direction strain. As the actuation reaches 140 microns (**Figure 42**), the 50-pixel facet image (**Figure 42 A**) shows the first signs of localized tablet sliding occurring with the presence of the increased strain on the uppermost tablet indicated by the color change. The other facet sizes have not detected these strain increases yet.

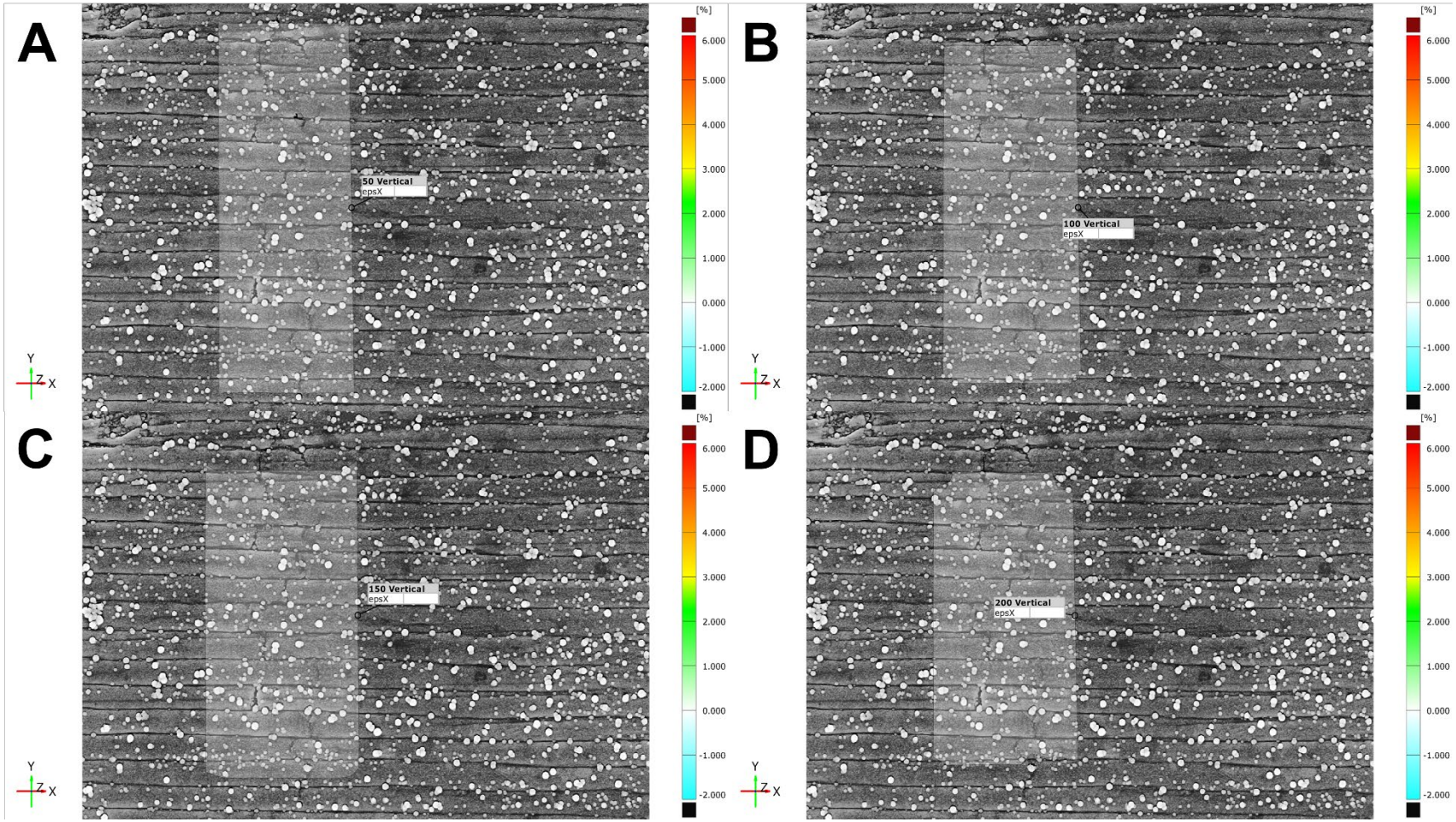

Figure 39: Images comparing the various surface components including the (A)50-pixel facet surface component, (B) 100-pixel facet surface component, (C) 150-pixel facet surface component, and (D) 200-pixel facet surface component with the undeformed reference stage image.

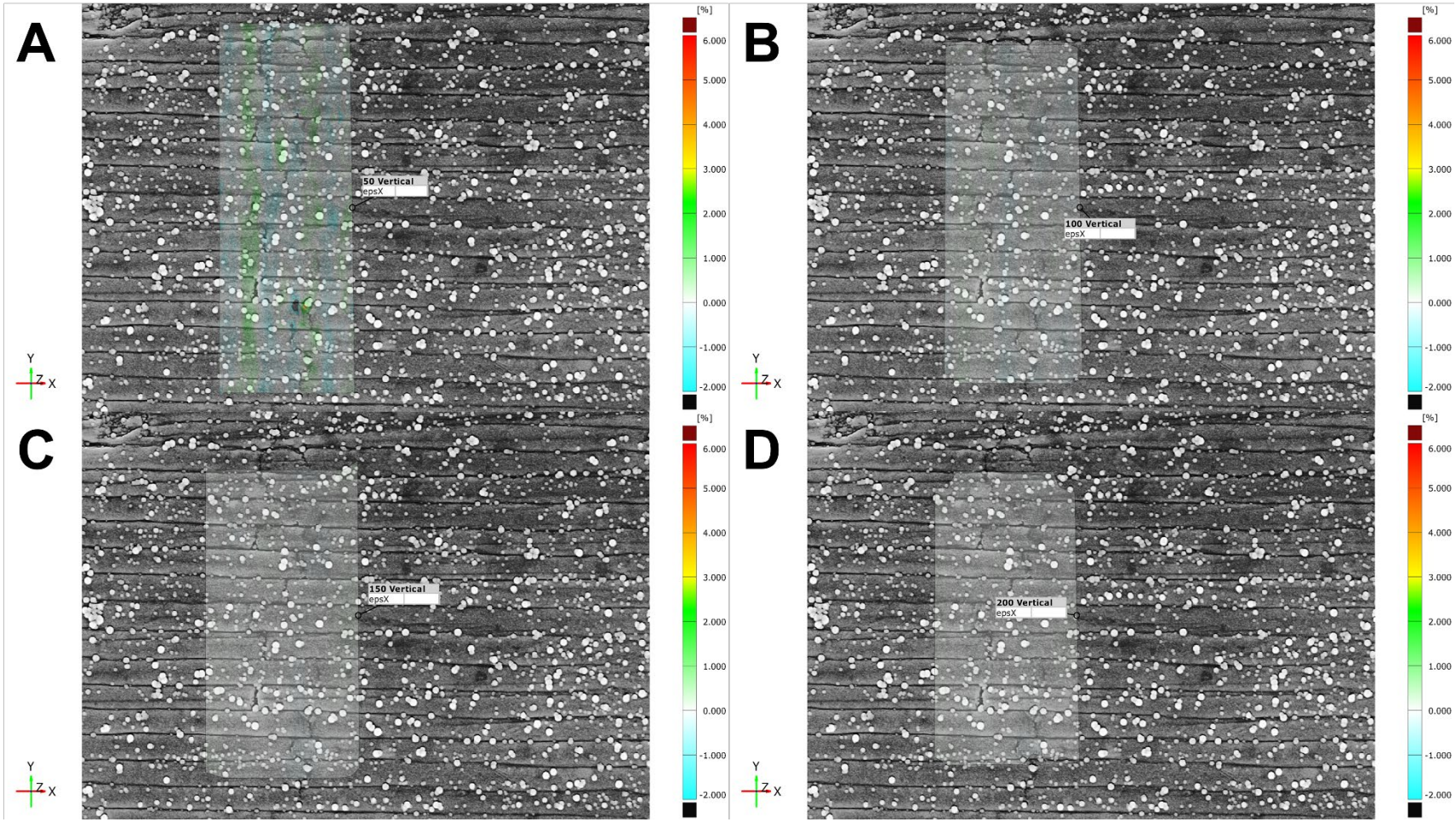

Figure 40: Images comparing the various surface components including the (A)50-pixel facet surface component, (B) 100-pixel facet surface component, (C) 150-pixel facet surface component, and (D) 200-pixel facet surface component at 20 microns of forward actuation.

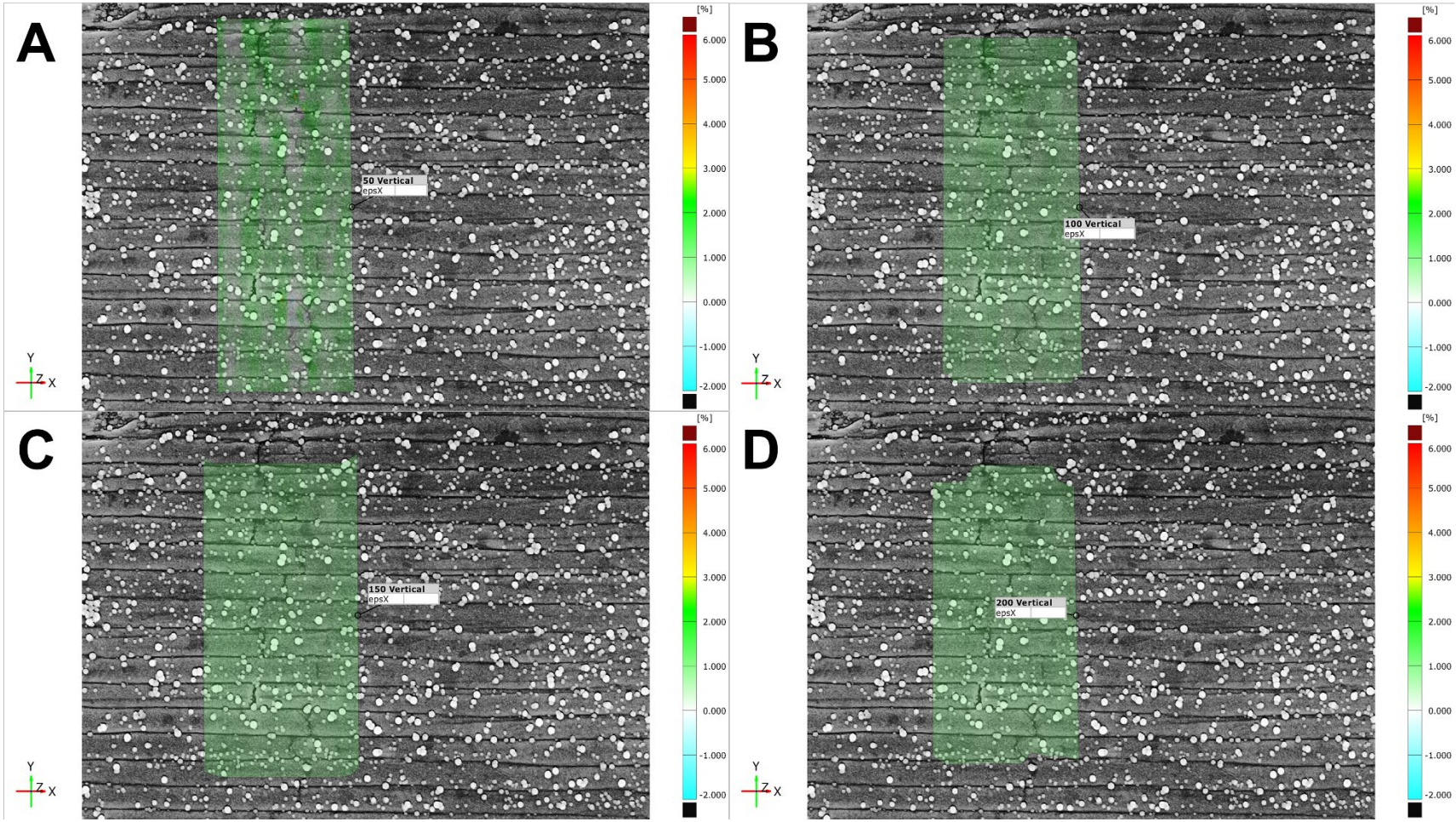

Figure 41: Images comparing the various surface components including the (A)50-pixel facet surface component, (B) 100-pixel facet surface component, (C) 150-pixel facet surface component, and (D) 200-pixel facet surface component at 100 microns of forward actuation.

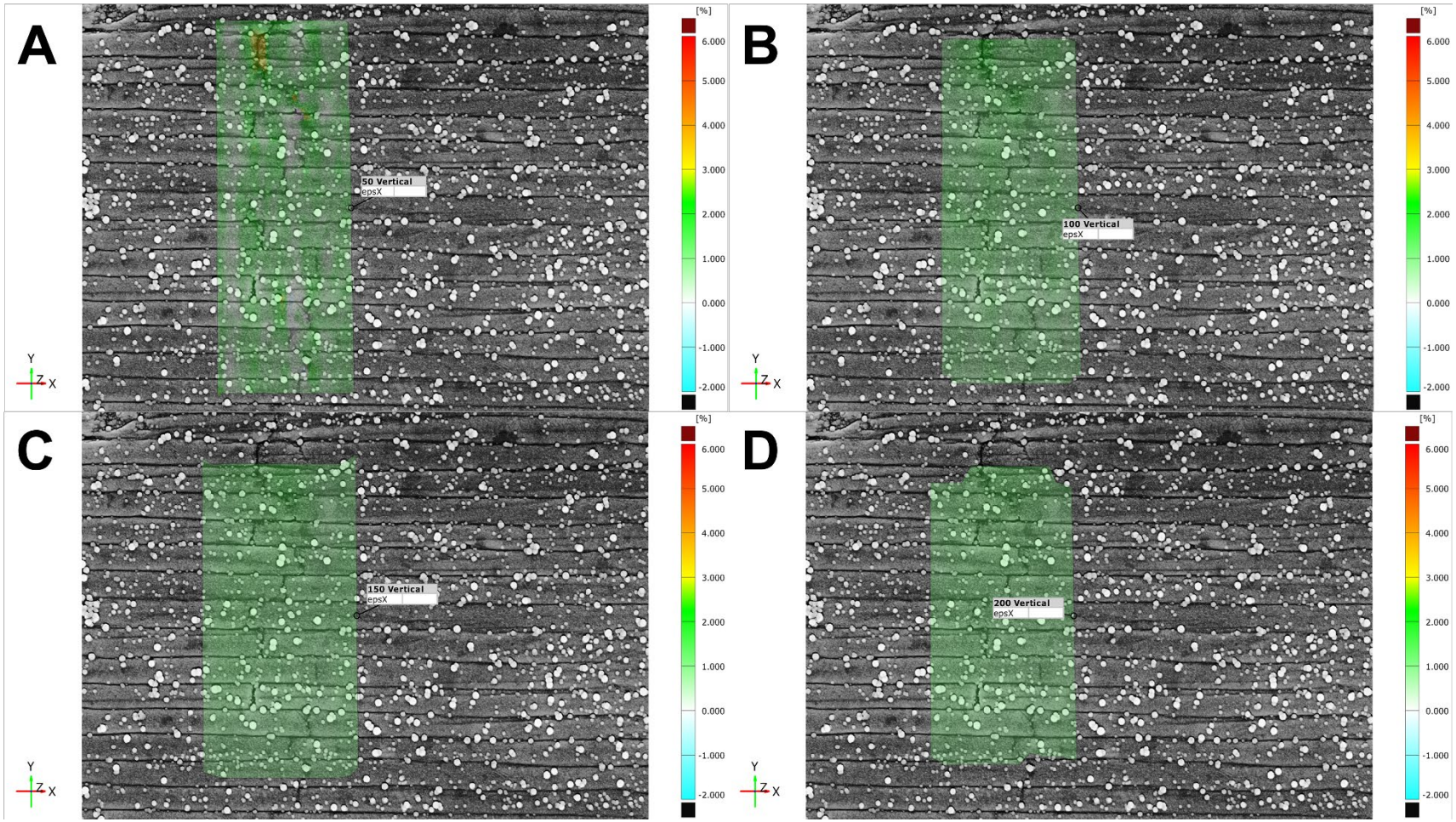

Figure 42: Images comparing the various surface components including the (A)50-pixel facet surface component, (B) 100-pixel facet surface component, (C) 150-pixel facet surface component, and (D) 200-pixel facet surface component at 140 microns of forward actuation.

Arriving at 220 microns of forward actuation (**Figure 43**), looking at the 50-pixel facet component (**Figure 43 A**), the strain calculations are very much localized to just the area surrounding the gaps forming at the sliding tablets. As the facet size increases (**Figure 43 B-D**), the calculations shift from the localized strain variations to a broader and band like formation, with the 200-pixel facets having the largest band of strains (**Figure 43 D**). There is also a decrease in the intensity of the strain measured in these areas indicated by the lightening of the colors between the 50-, 100-, 150- and 200-pixel facet surface components. Both the broadened banding structure of the strain calculations as well as the reduction in the intensity of the strains calculated are attributed to the "smoothing" affect caused by the overlapping nature of the increased facet sizes.

Another difference noticed in strain calculations at this point between the various surface components is the shifting of the some of the strains associated with the tablet gaps away from the areas where the tablet sliding is occurring (Highlighted in **Figure 43 B-D**). The 50-pixel surface component maintains the strains at the locations where the tablet sliding is occurring, whereas the 100-,150, and 200-pixel surface component have a shift in the strains in certain areas. This is again attributed to the loss of local strain calculation caused by the overlapping facets of these components.

When the actuation reaches the maximum 240 microns (**Figure 44**), the degree of brightness caused by the formation of the tablet gaps in the upper portion of the sample causes a loss in integrity of the strain calculations in the 50-, 100-, and 150-pixel surface components (**Figure 44 A-C**). This brightness prevents the software from viewing the speckle pattern in the facets selected in this area, and thus the strains can't be measured at these specific areas for all but the 200-pixel facet surface component (**Figure 44 D**) as this particular surface component does not reach this area. There is also the spot of compressive strain calculated in the 50-pixel facet component

(**Figure 44 A**), indicated by the black and blue area in the strain calculation image. This is most likely caused by one of the speckles in the area where this facet is tracking has been caught in the interface between the neighboring tablets, and thus does not move during the sliding. This would cause the calculations to measure these facets as if they are moving towards one another in a compressive manner in this area even though, in reality, a particular speckle is just locked in place.

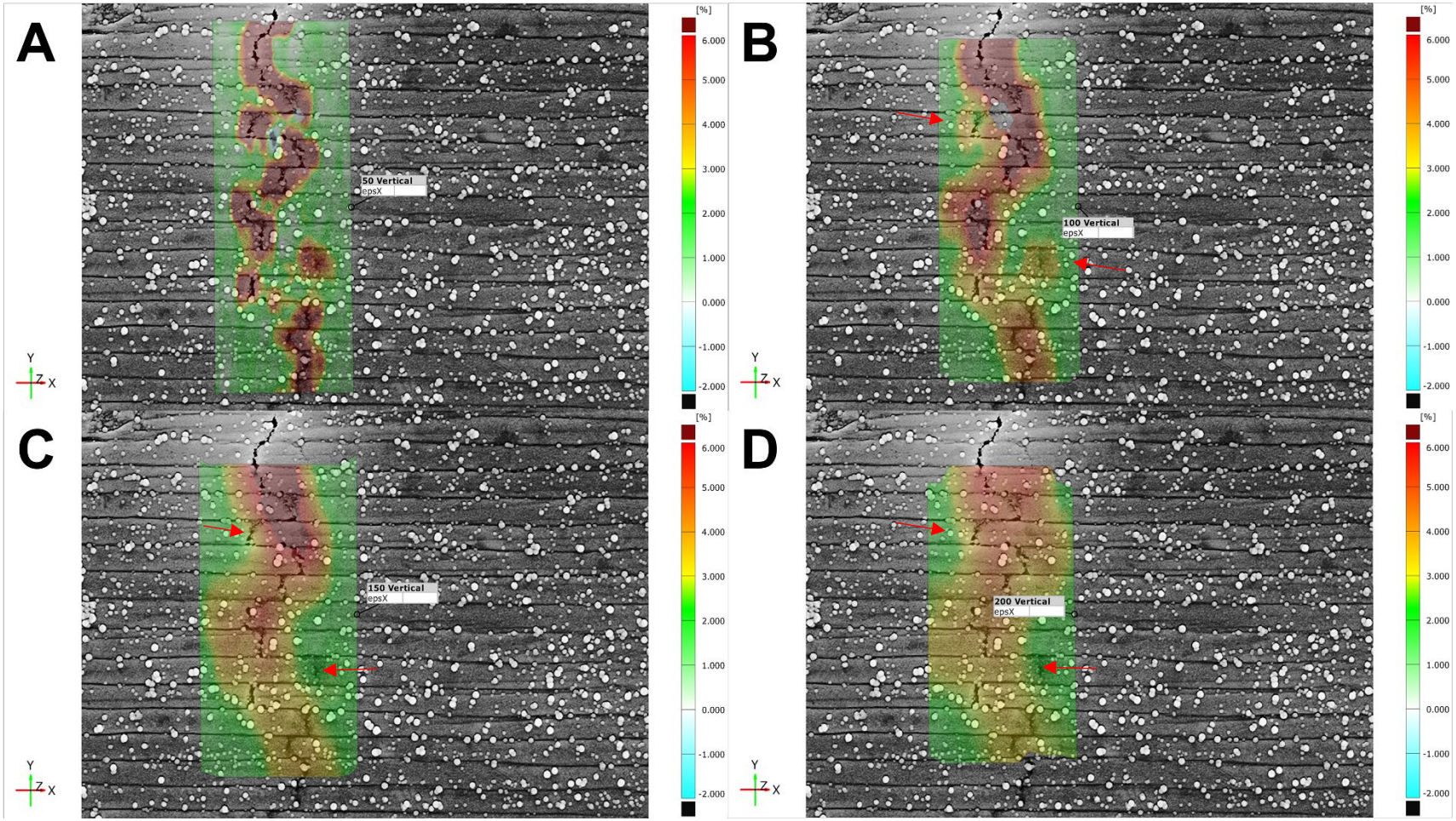

Figure 43: Images comparing the various surface components including the (A)50-pixel facet surface component, (B) 100-pixel facet surface component, (C) 150-pixel facet surface component, and (D) 200-pixel facet surface component at 220 microns of forward actuation.

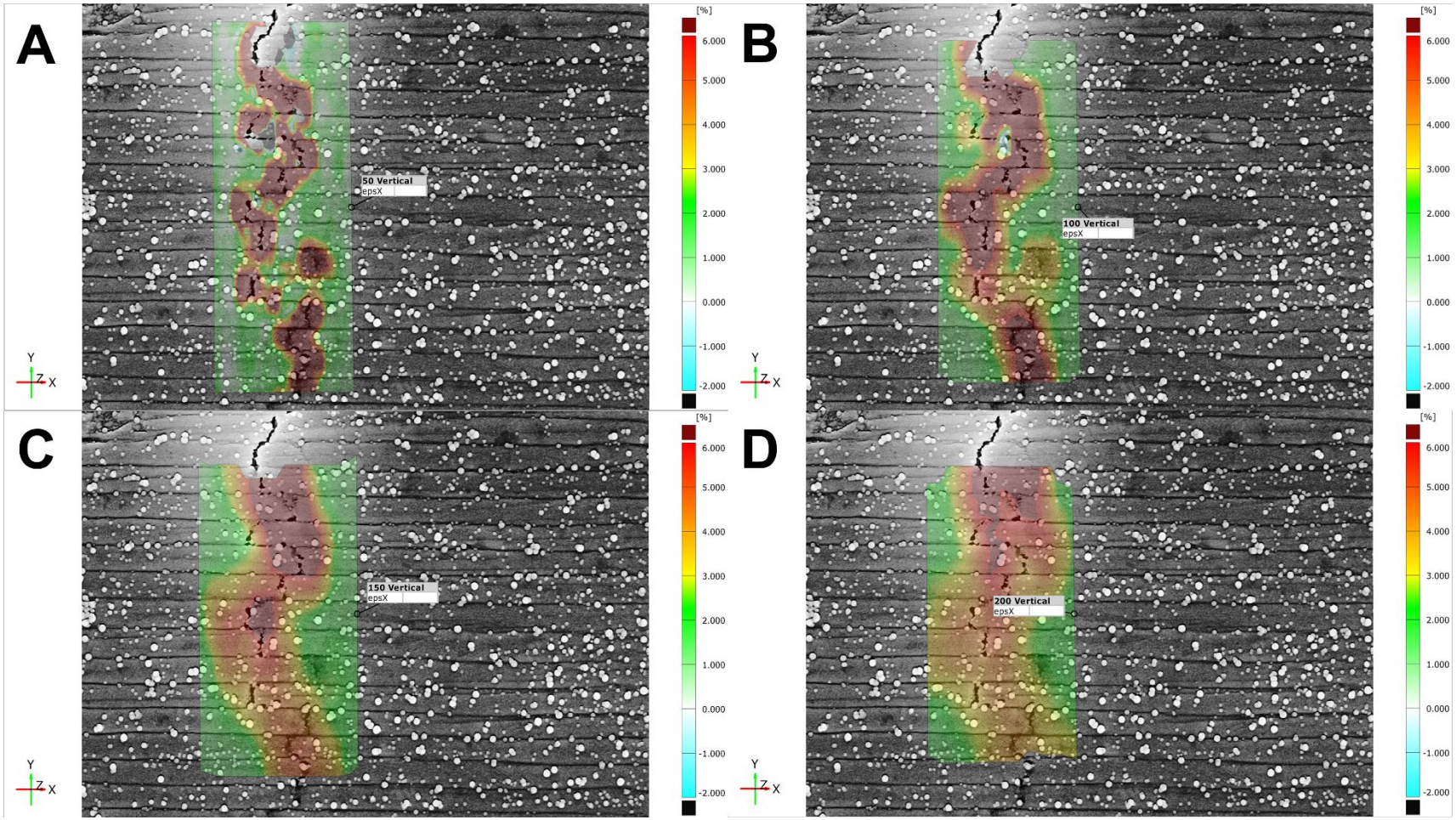

Figure 44: Images comparing the various surface components including the (A)50-pixel facet surface component, (B) 100-pixel facet surface component, (C) 150-pixel facet surface component, and (D) 200-pixel facet surface component at the maximum of 240 microns of actuation.

With the actuation reversed to 120 microns (**Figure 45**), the tablet gaps have closed enough that the brightness caused by them has reduced, allowing the software to recognize the pattern in these areas again, and thus the strains calculations could be performed again. As the actuation is returned to 60 microns (**Figure 46**), the strains in the tablet gaps in the 50-pixel component (**Figure 46 A**) are still very much present and still localized. The 100-pixel and 150-pixel facet components (**Figure 46 B-C**) still show some degree of strain, whereas the 200-pixel component (**Figure 46 D**) appears to have recovered almost all of the strain. Once the strain is completely removed (**Figure 47**), we can now see even more differences in the strain calculations produced from the various surface components. The 50-pixel surface component (**Figure 47 A**) shows a large degree of residual strain left in the sample at the tablet gap interfaces. The 100-pixel surface component (**Figure 47 B**) shows some remaining in certain locations, whereas the 150- and 200-pixel surface components (**Figure 47 C-D**) show almost all strain completely recovered, with no indication of gaps remaining.

With all of these differences in mind, it was determined that the 50-pixel surface component would be the most effective in calculating the strains present in the sample during deformation. The smaller facet size allows the surface component to avoid the pit falls of the others, such as the banded strain structure and shifted strains from the locations of tablet sliding caused by the "smoothing" effect of the overlapping facets in the larger pixel facet components. The ability to measure and calculate the minute local changes in the strains during deformation with the 50-pixel surface component. The potential negative effects such as the loss of strain visualization in areas and the small area of compressive strain calculated in some images are far outweighed by the increased amount of strain data that is achieved.

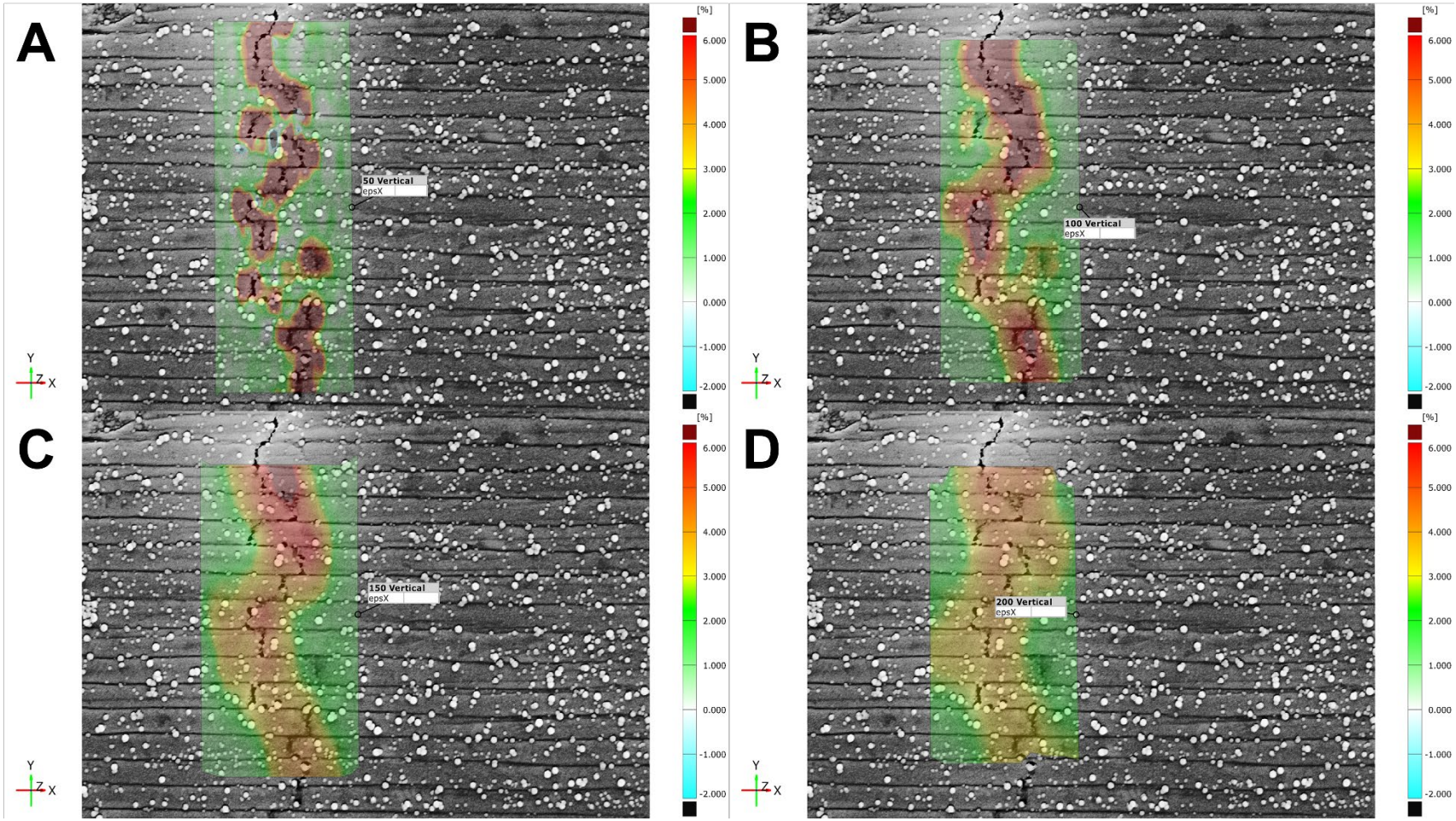

Figure 45: Images comparing the various surface components including the (A)50-pixel facet surface component, (B) 100-pixel facet surface component, (C) 150-pixel facet surface component, and (D) 200-pixel facet surface component when the actuation was reversed to 120 microns of actuation.

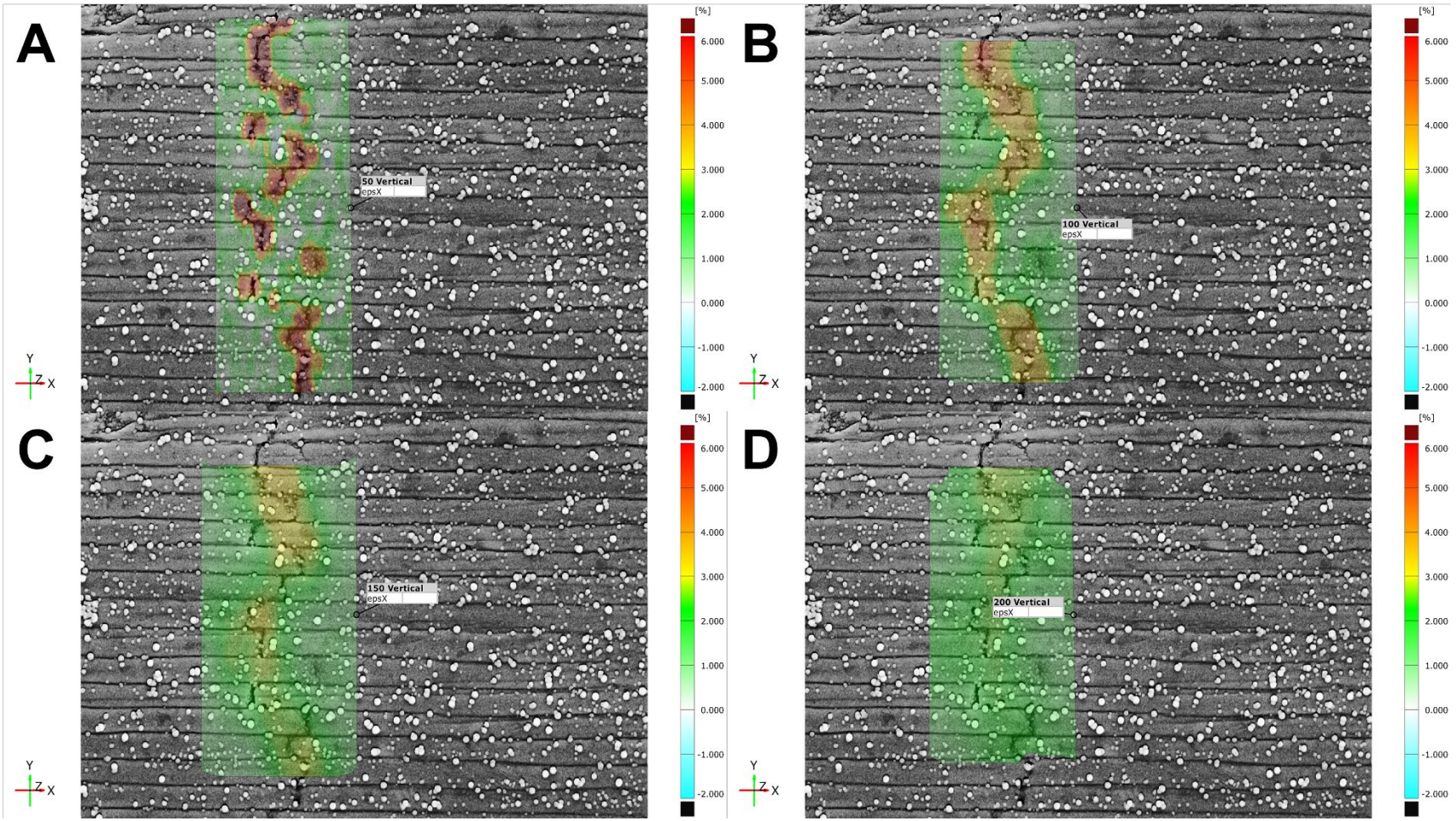

Figure 46: Images comparing the various surface components including the (A)50-pixel facet surface component, (B) 100-pixel facet surface component, (C) 150-pixel facet surface component, and (D) 200-pixel facet surface component when the actuation was reversed to 60 microns of actuation.

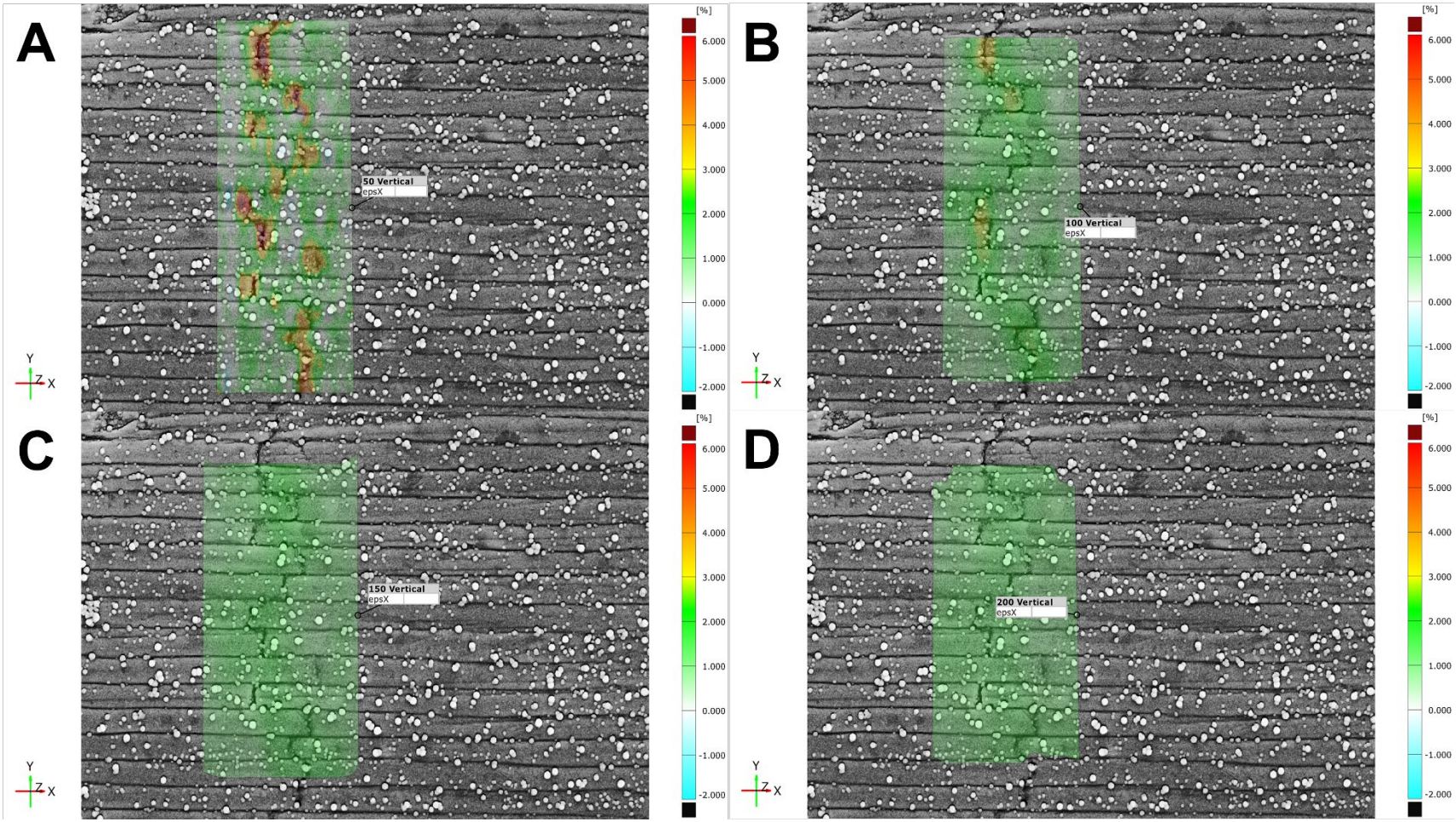

Figure 47: Images comparing the various surface components including the (A)50-pixel facet surface component, (B) 100-pixel facet surface component, (C) 150-pixel facet surface component, and (D) 200-pixel facet surface component when the actuation has been completely reversed.

4.4.3 Digital Image Correlation Results

After analyzing each of the surface components, it was determined that the 50-pixel surface component was the most appropriate option for calculating the strains in the deforming nacre sample. Once the 50-pixel surface component was constructed on the surface of the captured images, the GOM Correlate software was then used to perform stain calculations for the images at each stage of bending and reversal so that the local effects of the three-point bending experiment on the nacre architecture could be assessed. These strain measurements were performed for both the x-direction and the y-direction for each of the stages of bending and are depicted in **Figure 48-Figure 72**. The scale bar on the sides of these figures shows the color gradient between different strains on the surface. The zero percent strain color was selected to be white which will provide a good contrast between the other colors selected for non-zero strain and will allow the appearance of the increasing strain to be easily visualized. The compressive strains are represented by blue on the scale bar and range to -2% strain. The extrema for compressive strain for anything beyond -2% is represented by the color black and can be seen on the bottom of the scale bar. The tensile strains are represented by a range of colors starting with green, transitioning to yellow, then onto orange, and finally up to red which this scale bar ranges up to 6% tensile strain. The extrema for tensile strain for anything above 6% strain is represented by the dark burgundy color and can be seen at the top end of the scale bar.

Figure 48 shows the images captured of the nacre architecture in the initial undeformed state. The digital image correlation overlayed on the surface shows the strain calculations performed for both the x-direction (**Figure 48 A**) and the y-direction (**Figure 48 B**). For the initial unbent stage of the nacre architecture, the strains calculated on the surface were zero, as this was the undeformed

reference stage. This is represented by the all-white of the surface component which was chosen as the color to represent zero strain. After the actuator was advanced the initial 20 microns (**Figure 49**), the strain measurements on the surface component appears to have calculated a banded like structure with both compressive and tensile strains present in the x-direction (**Figure 49 A**) and y-direction (**Figure 49 B**). This is likely caused by the repositioning of the SEM stage between each image taken, as when the actuation is increased, the section of interest moves out of view of the scanning view of the SEM. When the area is brought back into view, changes in the way the electron beam rasters on the surface of the sample can cause these minute changes in the positioning of the speckles in the images.

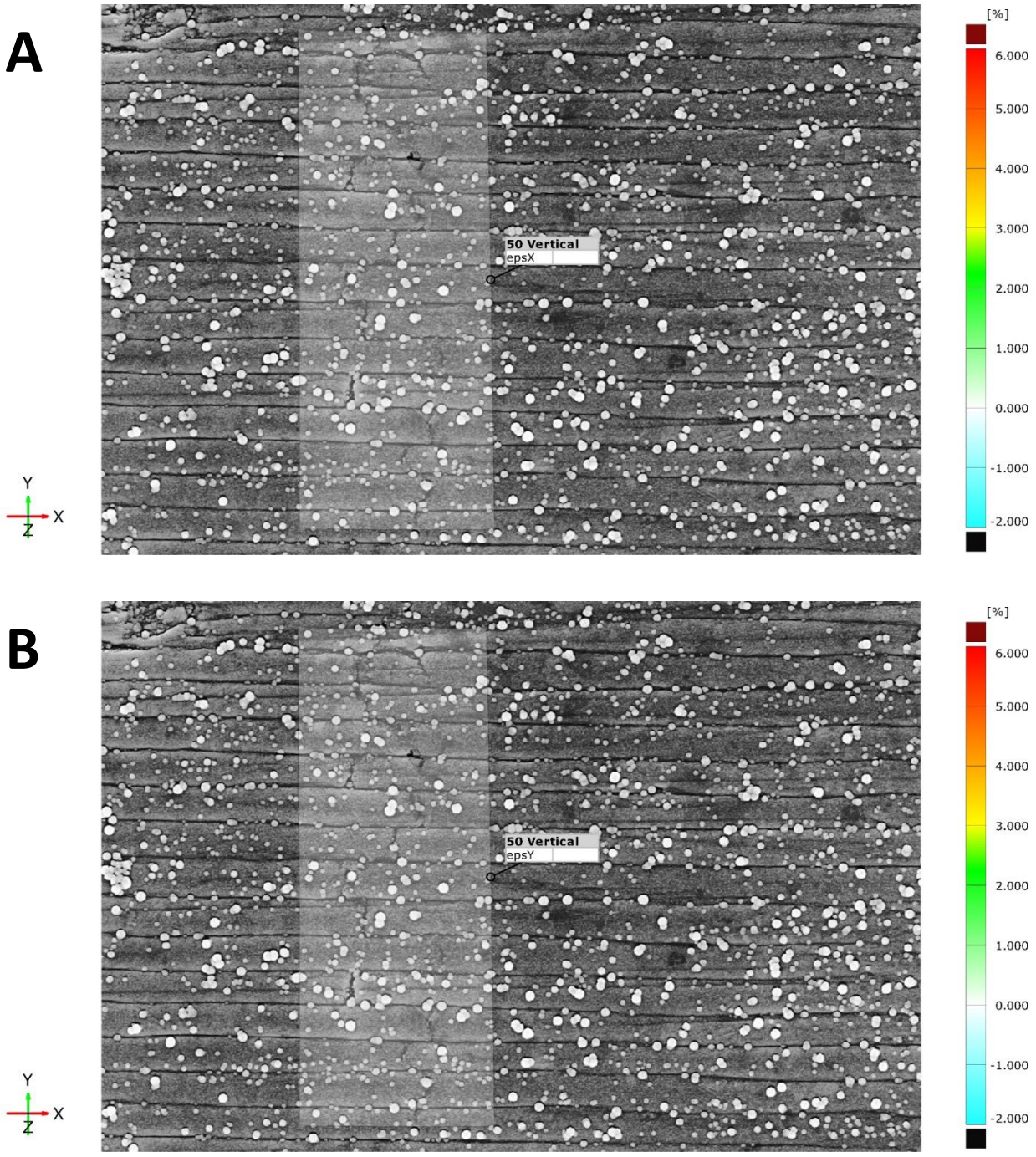

Figure 48: Images of DIC being performed on captured SEM images of the initial undeformed state of the nacre architecture. DIC strains are presented for both the (A) x-direction and (B) y-direction.

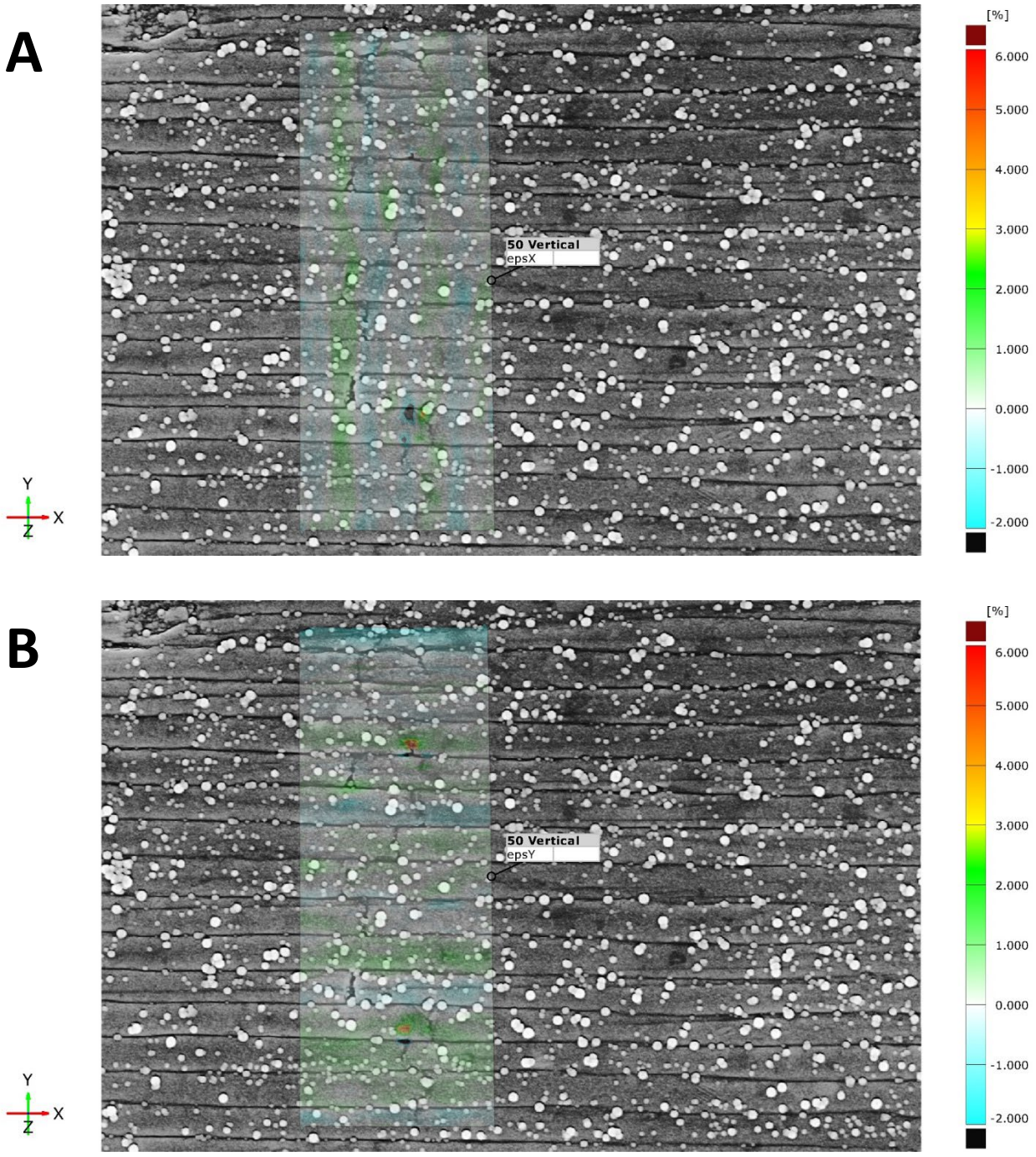

Figure 49: Images of DIC being performed on captured SEM images of the nacre architecture after 20 microns of actuation. DIC strains are presented for both the (A) x-direction and (B) y-direction.

When the shaft of the actuator was advanced to 40 microns (**Figure 50**) the strains can now be seen building in both the x- and y- directions. These strains can be seen by the change in the color of the surface component. As the tensile strains increase in the both the x-direction and the y-direction, the color on the surface component begins to shift towards green. At this stage, most areas can be seen beginning to form tensile strains, whereas others still remain unstrained indicated by the remaining white portions of the surface components. The y-direction also appears to have some isolated locations beginning to show a greater increase in strain indicated by the appearance of yellow on the surface component (**Figure 50 B**). Upon advancing the actuator shaft to 60 microns (**Figure 51**), the strain in the x-direction appears to hold relatively steady with little changes or increase in the intensity of the colors on the surface component. However, the strains in the y-direction appear to continue to increase. **Figure 51 B** shows the strains in the y-direction appear to have increased further indicated by the appearance of discrete bands of yellow/orange coloring on the surface component, while the rest of the surface component still maintains the green coloring throughout the rest of the surface component.

As the actuation was advanced to 80 microns, the strain in the nacre architecture continues to evolve further. The strain in the x-direction (**Figure 52 A**) continues to remain constant, with no change in the color gradient of the surface component or formation of any visible gaps. The strain in the y-direction, however, changes drastically. **Figure 52 B** shows the strain measured in the y-direction of the nacre architecture shown on the surface component is now predominantly yellow and orange, with small amounts of green interspersed throughout. There is also a dark red portion of the surface component at the upper most portion of the surface component. Once the actuator was advanced to 100 microns, the strain map of the nacre architecture changes once again (**Figure 53**). While holding constant in the x-direction, the strain in the y-direction has gone through a

relaxation, indicated by the change in intensity of the color gradient. The areas previously with a higher strain and intense yellow, orange and even red coloring now appear either light yellow or green.

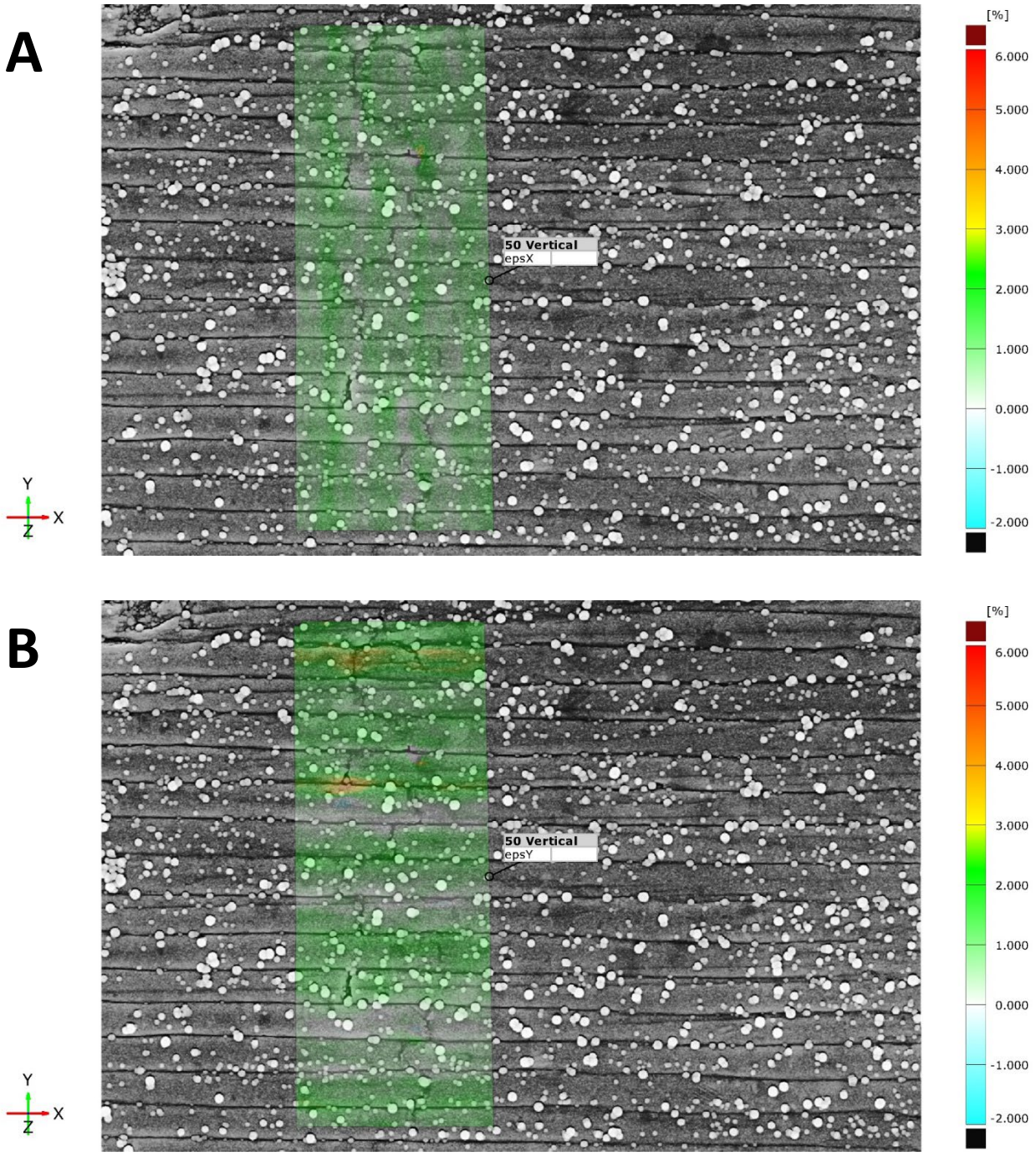

Figure 50: Images of DIC being performed on captured SEM images of the nacre architecture after 40 microns of actuation. DIC strains are presented for both the (A) x-direction and (B) y-direction.

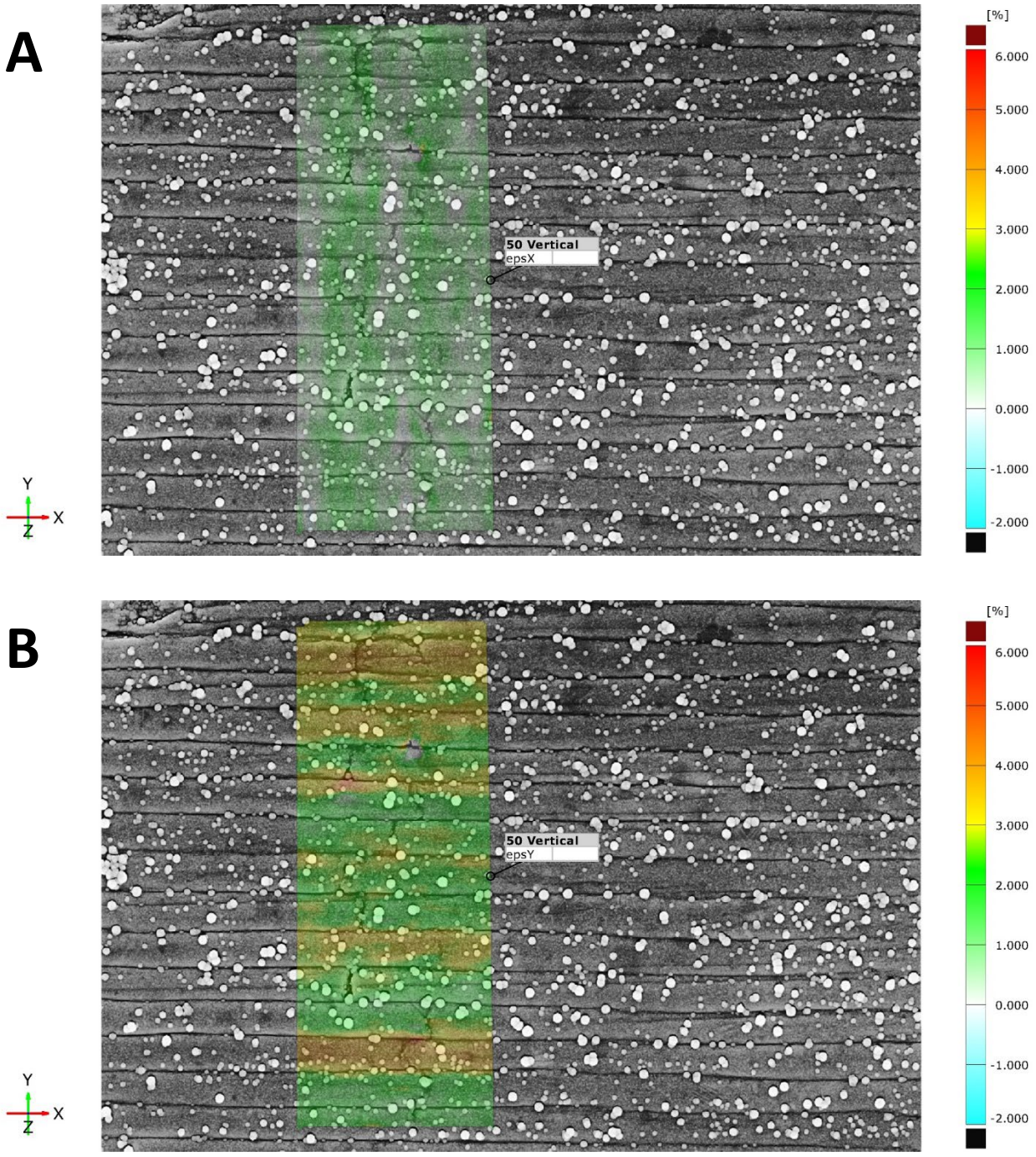

Figure 51: Images of DIC being performed on captured SEM images of the nacre architecture after 60 microns of actuation. DIC strains are presented for both the (A) x-direction and (B) y-direction.

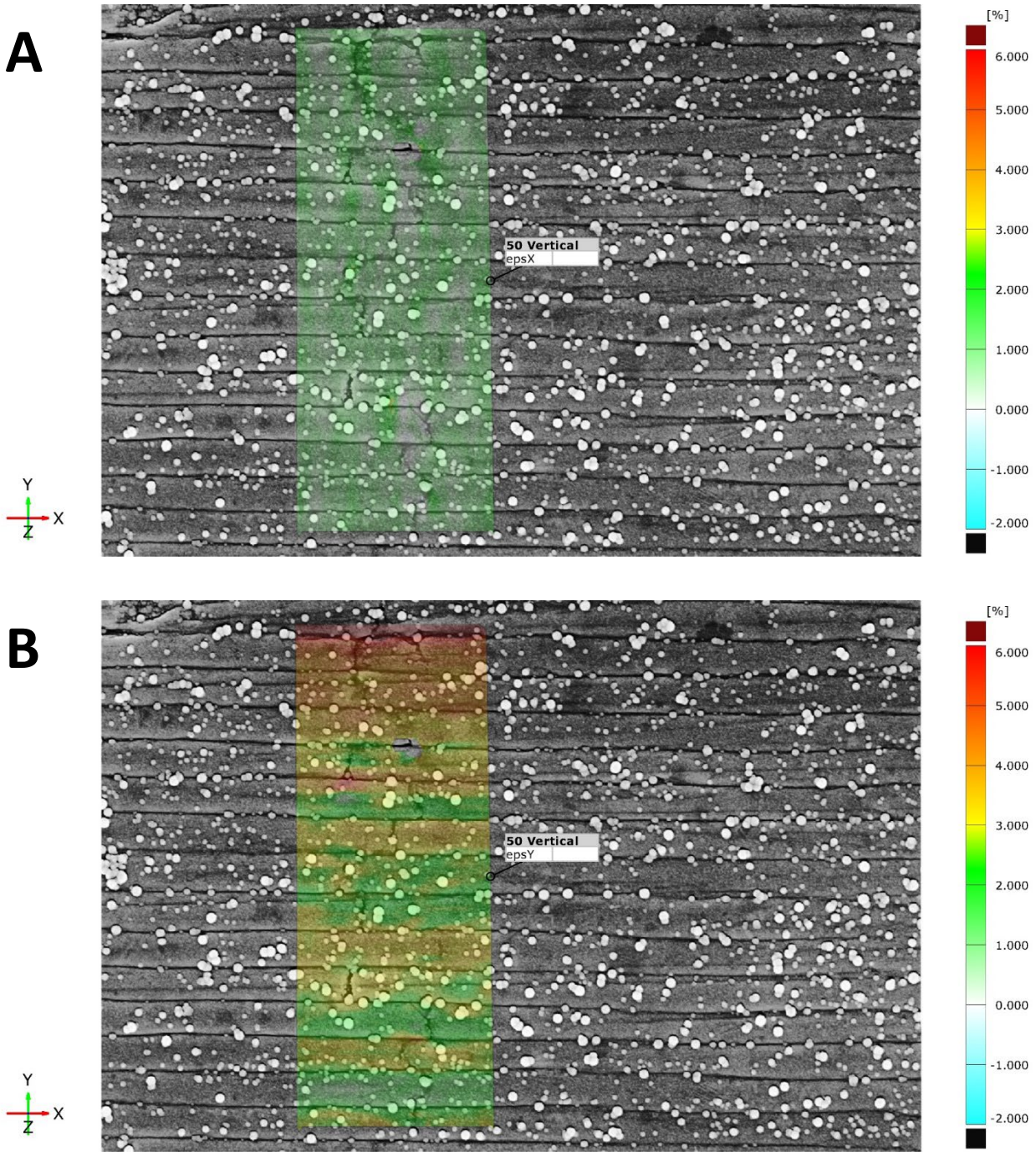

Figure 52: Images of DIC being performed on captured SEM images of the nacre architecture after 80 microns of actuation. DIC strains are presented for both the (A) x-direction and (B) y-direction.

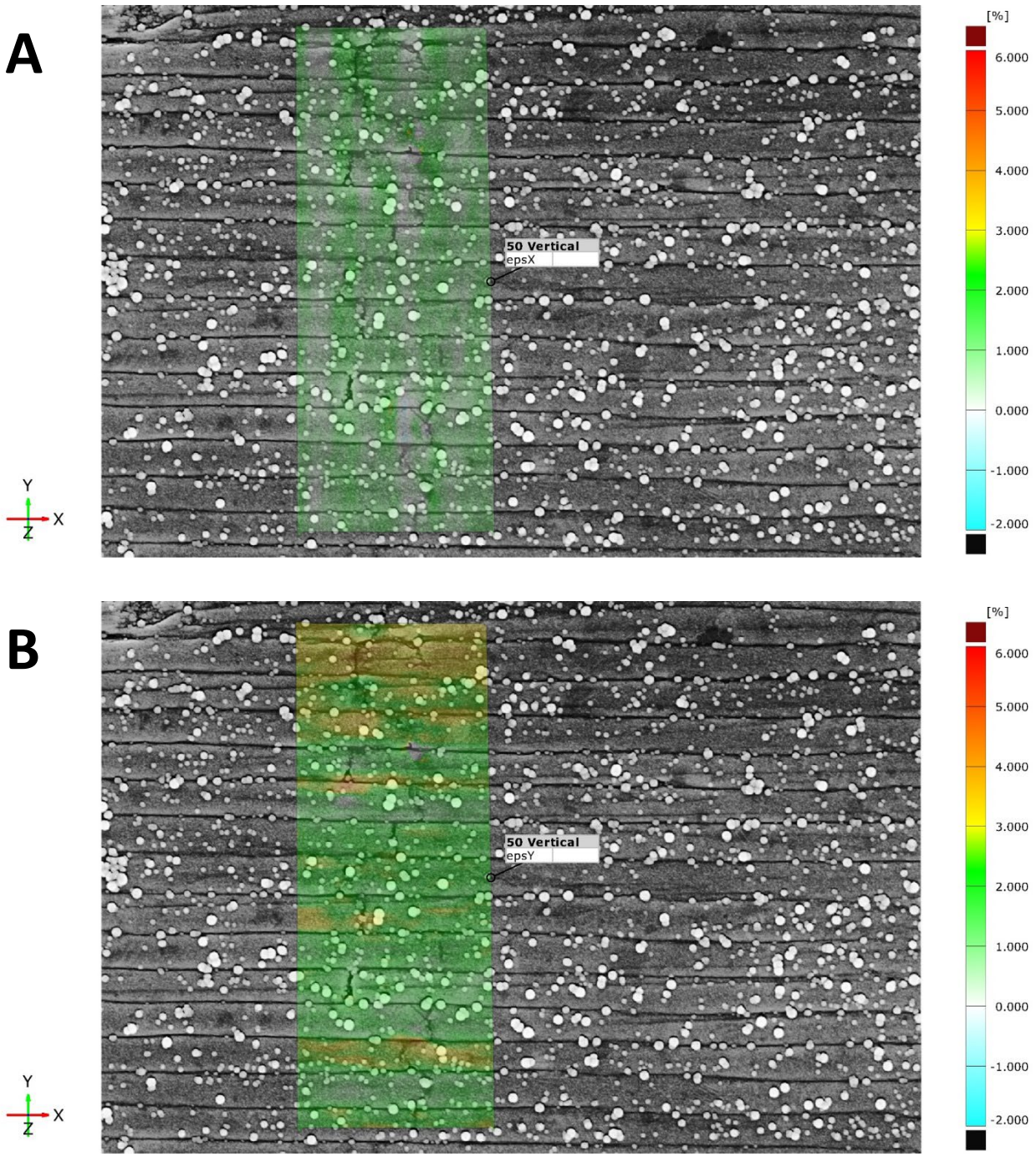

Figure 53: Images of DIC being performed on captured SEM images of the nacre architecture after 100 microns of actuation. DIC strains are presented for both the (A) x-direction and (B) y-direction.

This reduction in the strain in the y-direction continues to evolve as the actuator is advanced further to 120 microns (**Figure 54**). The yellow in the y-direction strain surface component (**Figure 54 B**) has almost completely vanished and is replaced by green in most areas. Once the actuator was advanced to 140 microns (**Figure 55**), the strain in the nacre architecture takes another turn in its evolution. The strain in the y-direction here has increased again, indicated by the appearance of more yellow and orange in the surface component in **Figure 55 B**. But unlike with the previous stages of actuation, the strain in the x-direction is no longer holding constant. In **Figure 55 A**, the strain in the upper most tablet interface has shifted in color from green to yellow/orange, indicating an increase in the strain at this point.

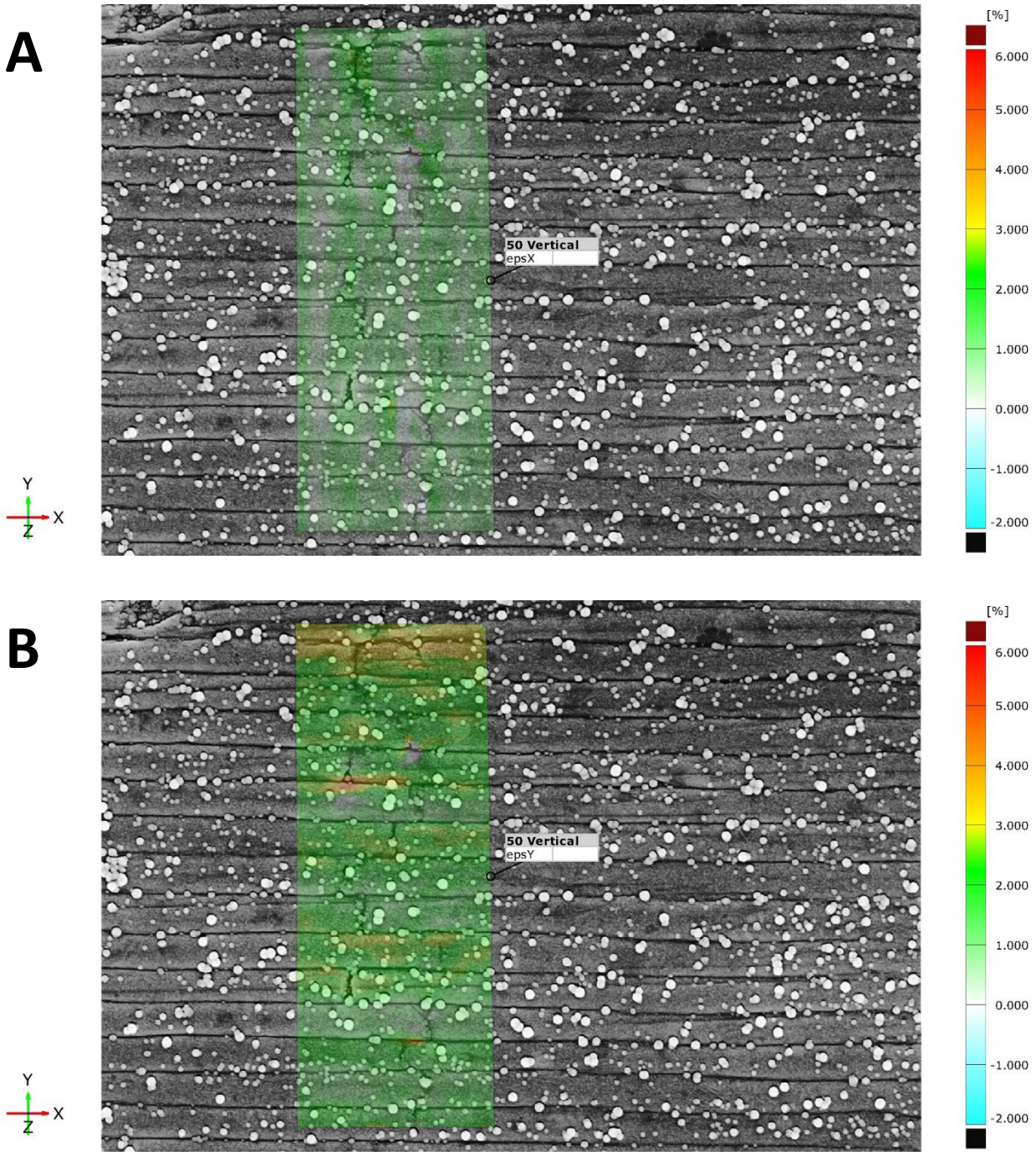

Figure 54: Images of DIC being performed on captured SEM images of the nacre architecture after 120 microns of actuation. DIC strains are presented for both the (A) x-direction and (B) y-direction.

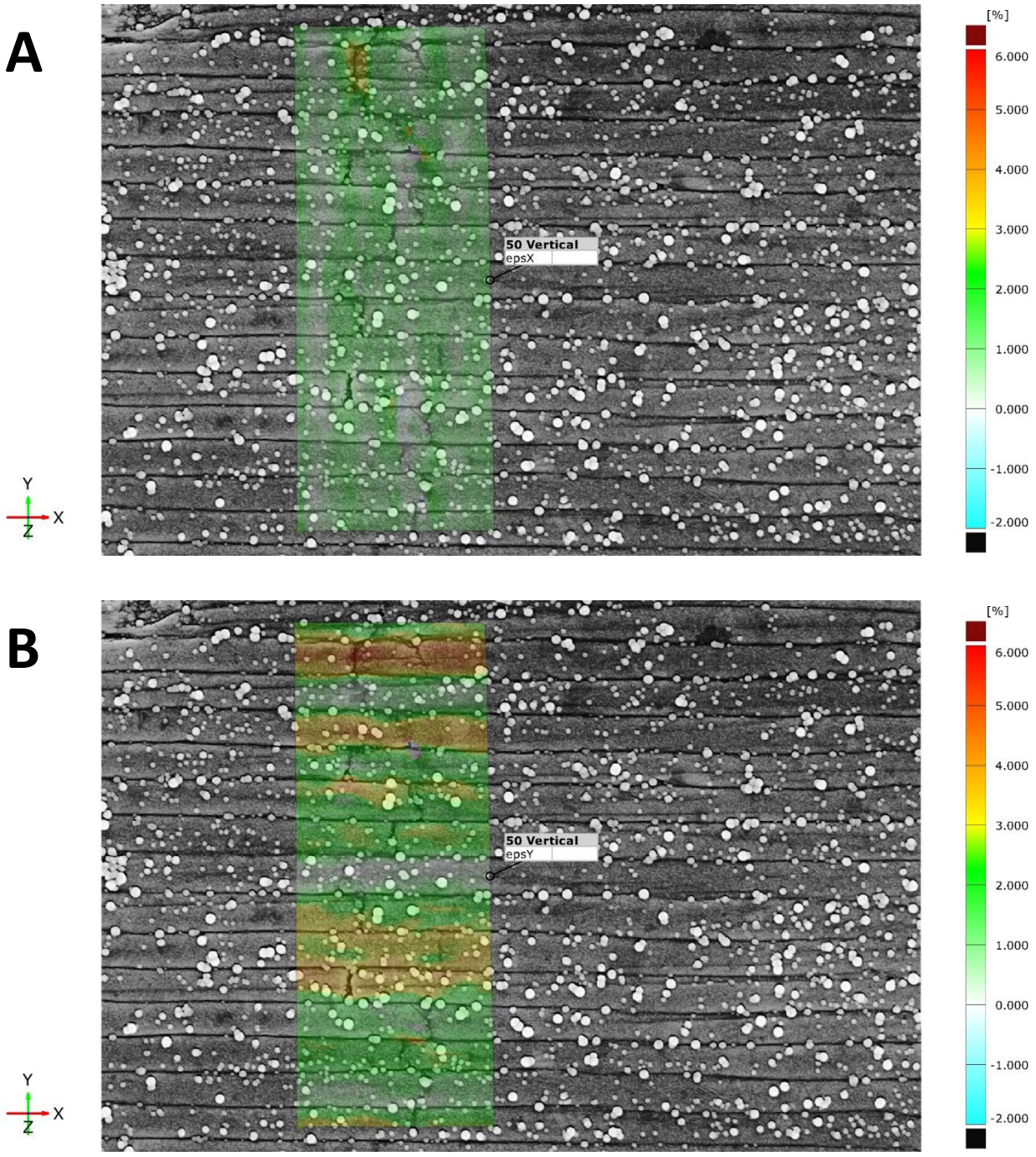

Figure 55: Images of DIC being performed on captured SEM images of the nacre architecture after 140 microns of actuation. DIC strains are presented for both the (A) x-direction and (B) y-direction.

The evolution of the strain in the nacre architecture from 40 to 140 microns of actuation (**Figure 50-Figure 55**) reveals a very interesting dynamic caused by the bending of the nacre architecture. Through the initial stages of actuation, the strain in the x direction remains fairly consistent, maintaining roughly the same amount of strain as the previous deformation images. However, the strain in the y-direction increases significantly by comparison and continues to increase through 80 microns of actuation. This increasing strain in the y-direction is indicative of the presence of nanoasperities between the tablet interfaces that run along the length of the tablets and reveals how these nanoasperities interact with one another during the tablet sliding deformation mechanism. As the nacre architecture is bent further and further, the tablets start sliding apart from one another. However, before the tablets can slide apart from one another and form visible gaps, they must overcome a host of other mechanisms that help strengthen the material such as the nanoasperities.

At the start of tablet sliding, the nanoasperities come in contact with one another, stopping any further sliding of the tablets in the nacre architecture. For the sliding to continue, the nanoasperities must overcome one another. Since the x-direction is blocked by the opposing nanoasperities, the only way for them to pass one another is by moving up and over in the y-direction. This motion of the nanoasperities overcoming one another is depicted in the increase in strain in the y-direction in the subsequent bending images. Once the nanoasperities in the tablet interfaces have moved past one another, the tablet interfaces are allowed to come back together which is indicated by the relaxation in the strain in the y-direction between the subsequent bending stages. It is only after the nanoasperities overcome one another that the tablets can slide further in the x-direction. This is seen by the increase in the strain in the x-direction following further bending after the relaxation. The strain in the y-direction was previously unseen as no visible gaps between the tablets in this direction were formed, so gap measurements, such as the ones performed in previous experiments

couldn't be made. However, with the aid of digital image correlation, we can see that the tablets undergo tensile strains in both the x-direction and y-direction.

Furthering the actuation from 140 microns to 160 microns (**Figure 56**), and yet again on to 180 microns of actuation (**Figure 57**) shows similar interactions to that of the previous increases in actuation. The strain in the y-directions relax incrementally between 140 microns (**Figure 55 B**) and 160 microns (**Figure 56 B**) and yet again when the actuation is increased to 180 microns (**Figure 57 B**). The increase in the strain in the y-direction for the 140-micron stage (**Figure 55 B**) and the subsequent relaxation of the strain in the y-direction for the 160-micron and 180-micron stages (**Figure 56 B** and **Figure 57 B**) is indicative of another set of nanoasperities have overcome one another. This is further validated by the change in the strains in the x-direction.

When the actuation reaches the 140-micron stage, the surface component shows the first signs of significant increase in strain in the x-direction (**Figure 55 A**). Upon further actuation to the 160-micron stage (**Figure 56 A**), the strain in the x-direction can be seen increasing further at the sight of the initial tablet interface from the 140-micron stage. It can also be seen that other tablet interfaces at this stage now have a deeper green or even a yellow/orange color over them, indicating an increase in the strain at these locations. Furthering the actuation again to the 180-micron stage (**Figure 57 A**), the strains in x-direction have now increased quite significantly, with several of the tablet interfaces now having a deep red color over them and visible gaps beginning to form between the tablets.

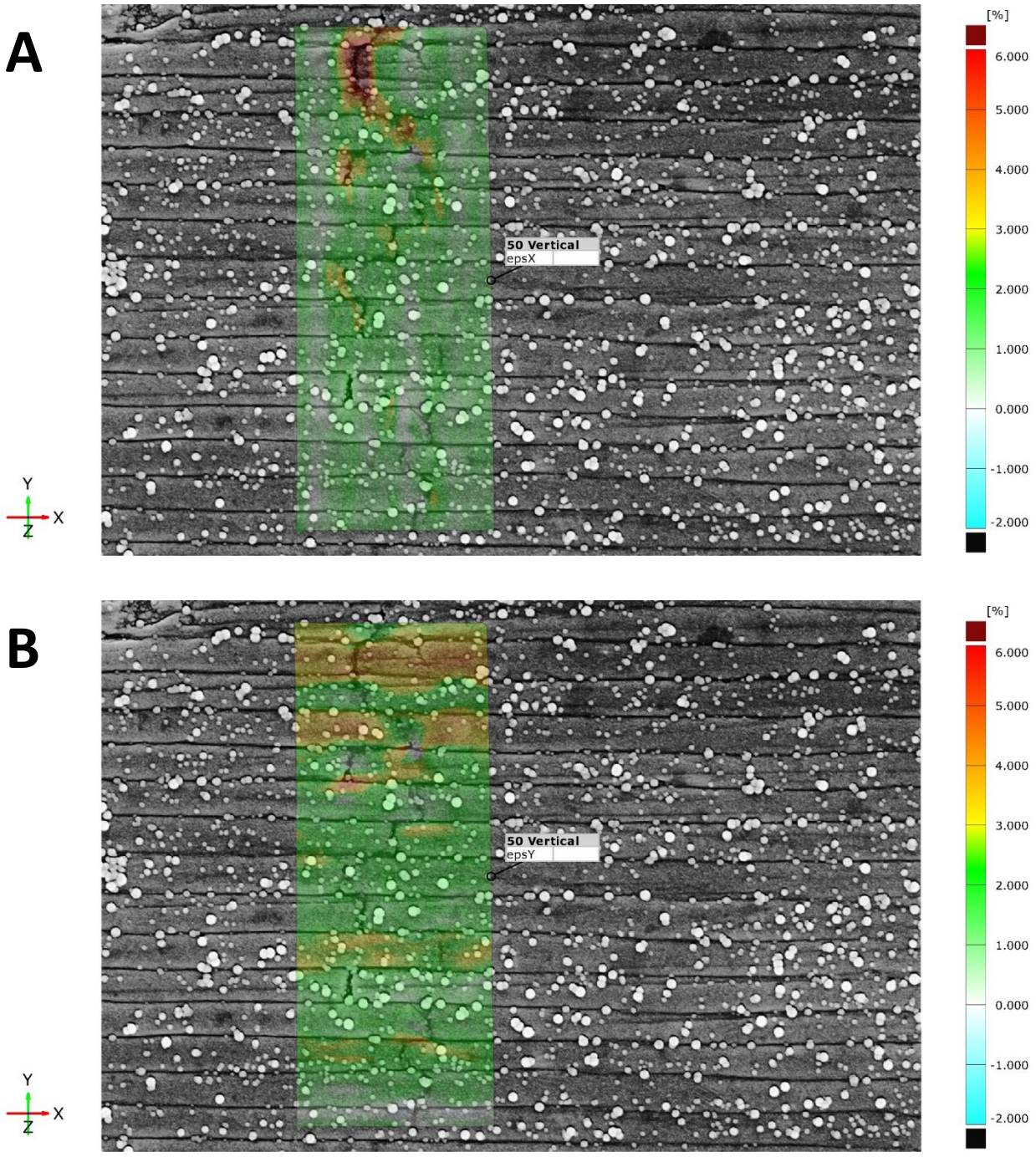

Figure 56: Images of DIC being performed on captured SEM images of the nacre architecture after 160 microns of actuation. DIC strains are presented for both the (A) x-direction and (B) y-direction.

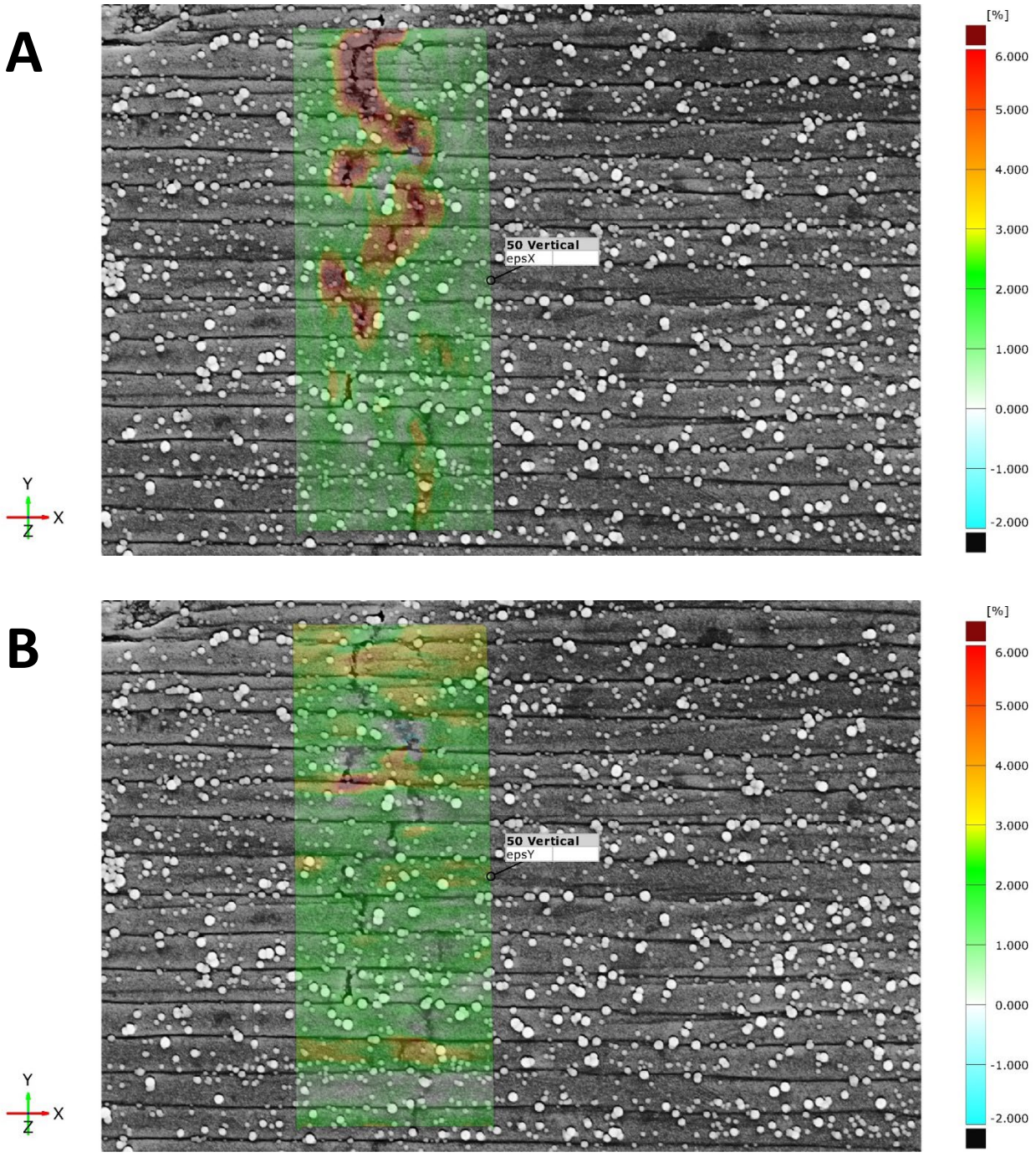

Figure 57: Images of DIC being performed on captured SEM images of the nacre architecture after 180 microns of actuation. DIC strains are presented for both the (A) x-direction and (B) y-direction.

As the actuator shaft reaches 200 microns of actuation (**Figure 58**), the strain in the x-direction increases further with the area of the surface component around the tablet gaps growing even darker red and that red covering more of the area around those tablet gaps. The gaps between the tablets can also be seen increasing further. The strain in the y-direction, however, does not appear to change as the actuation was furthered. These trends continue on as the bending reaches the 220-micron stage (**Figure 59**). The strain in the x-direction continues to increase, as seen by the increased area now covered by the deep red, while the strain in the y-direction maintains little to no change across most of the nacre architecture through this continued actuation. The increase in strain in the x-direction with little to no increase in strain in the y-direction is indicative of the tablet sliding no longer being restrained by the nano asperities and that the tablets are now free to continue sliding apart from one another with no impediment from this particular toughening mechanism in this area. There are however isolated locations of strain in the y-direction increasing. These appear to be localized near the tablet gaps and it is at these points where the tablets appear to be pulling apart from one another in that direction in these areas.

As the actuator shaft is advanced to 240 microns (**Figure 60**), the nacre architecture has reached the final stage of increased bending for this experiment. While the strain in the y-direction continues to remain relatively stable, the strain in the x-direction shows a deep red coloring around all of the visible tablet gaps and this coloring has now expanded wide across each of these tablet gaps (**Figure 60 A**). The tablet gaps themselves are also now visibly wider and show a great degree of tablet sliding has occurred. One of the side effects of the increased tablet sliding is the brightening of the edges of the tablet gaps, as occurred in previous experiments. This increased brightness has caused the surface component to lose track of the speckling in the uppermost tablet

in these images, meaning calculations for the strain won't be able to be performed at this stage of actuation in this particular area.

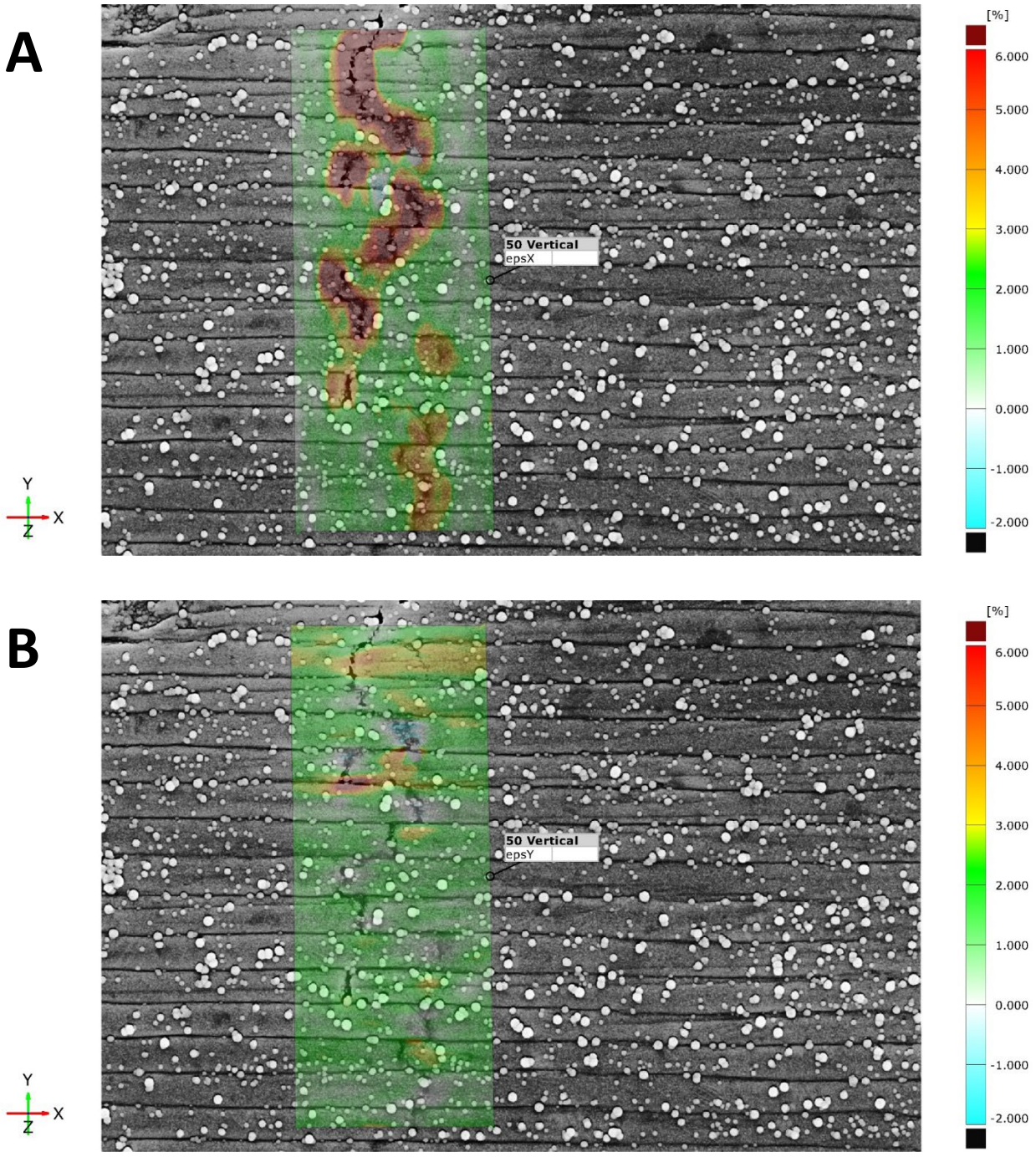

Figure 58: Images of DIC being performed on captured SEM images of the nacre architecture after 200 microns of actuation. DIC strains are presented for both the (A) x-direction and (B) y-direction.

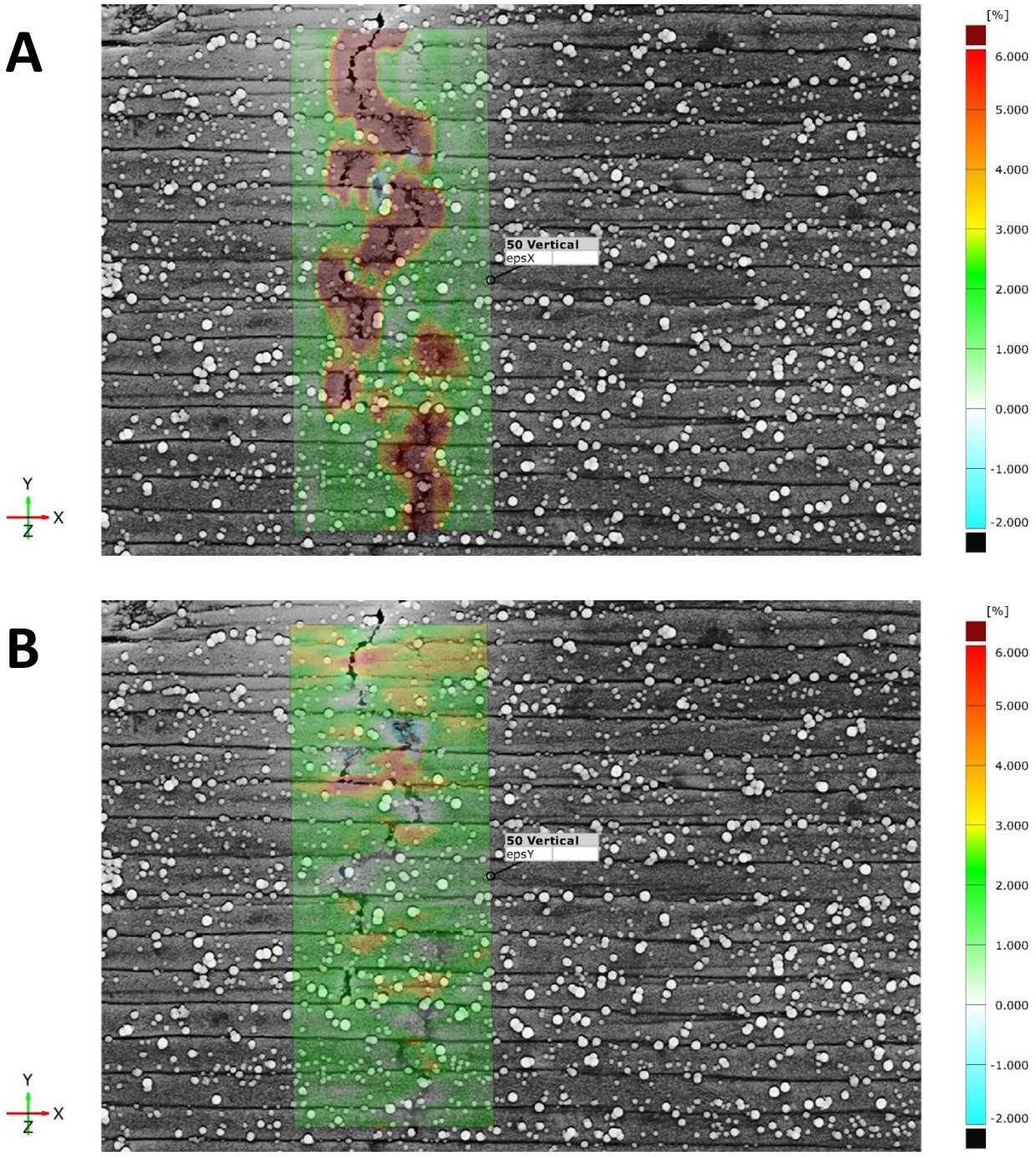

Figure 59: Images of DIC being performed on captured SEM images of the nacre architecture after 220 microns of actuation. DIC strains are presented for both the (A) x-direction and (B) y-direction.

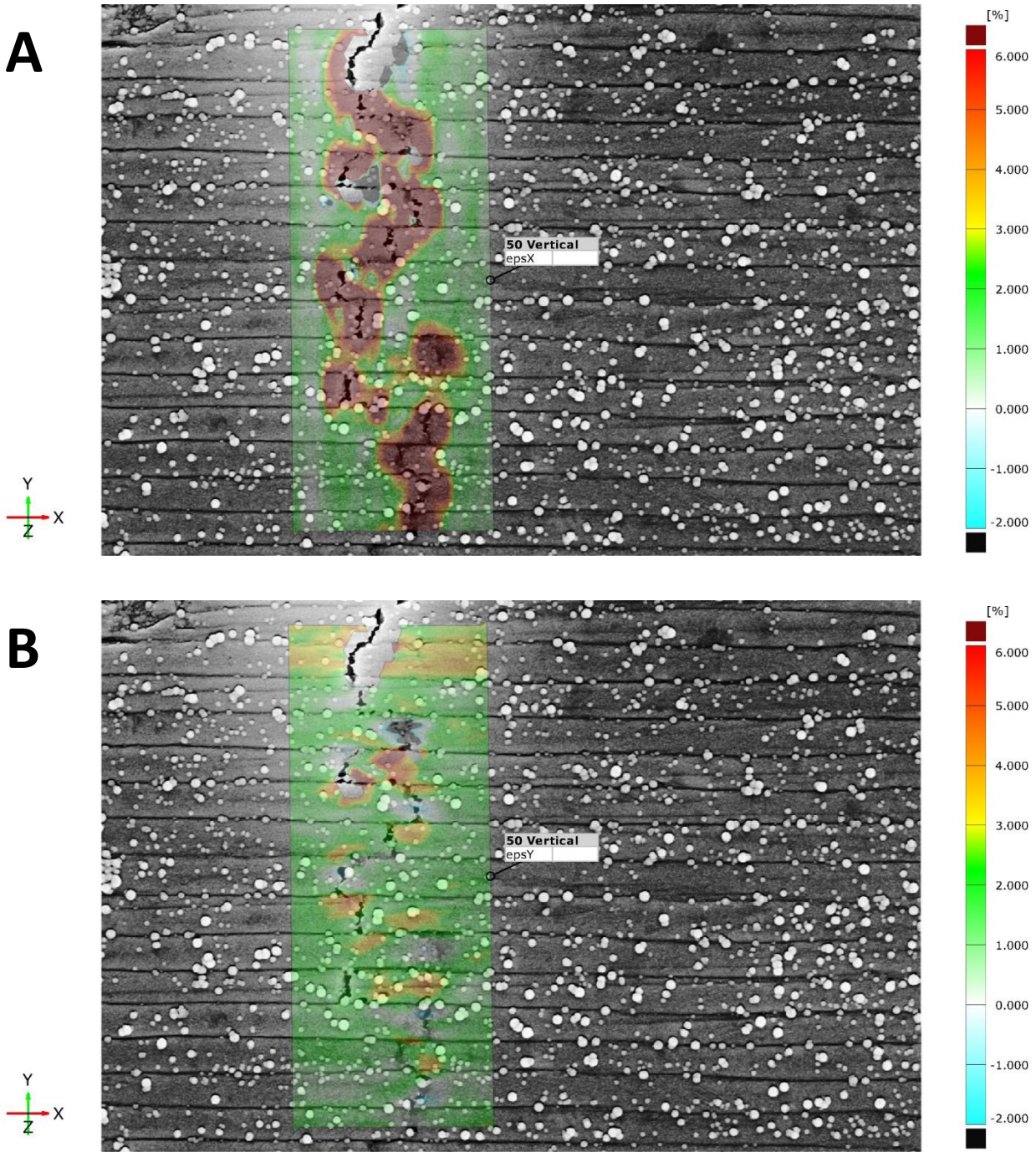

Figure 60: Images of DIC being performed on captured SEM images of the nacre architecture after 240 microns of actuation. DIC strains are presented for both the (A) x-direction and (B) y-direction.

Following capturing the images at the 240-micron stage, the actuator shaft was reversed 20 microns at a time and images were captured of the nacre architecture undergoing the reversible sliding mechanism. With the reversal of this actuation to 220 microns (**Figure 61**) and again to 200 microns (**Figure 62**), the reversible sliding process begins to get underway. For these initial stages of reversal actuation, the strain in both the x -direction and y-direction appear to remain fairly constant. The main notable change through these initial recovery stages is the reduction in the brightness around the edges of the tablet interfaces, which has allowed the surface component to begin tracking more of the area near the upper most tablet gap in the images of the nacre architecture. This reduction in the brightness is also indicative of the gaps formed between these tablets are beginning to close slightly. When the actuation is reversed to 180 microns (**Figure 63**), the strain in the x-direction around the tablet gaps is still holding fairly constant, with the tablets sliding back together slightly more as indicated by the further reduction in brightness and return of the calculated information in the areas where it was previously lost (**Figure 63A**). The strain in the y-direction (**Figure 63B**), however, has begun to show a response to the further reduction in actuation. As the 180-micron stage is reached, the strain in the y-direction increases in the band-like pattern similar to how the nacre architecture responded to the forward actuation. This may indicate that as the tablets are sliding back together, the nano asperities which had previously hindered the tablets from sliding apart, now need to be overcome once again in order for the reversible sliding mechanism to continue.

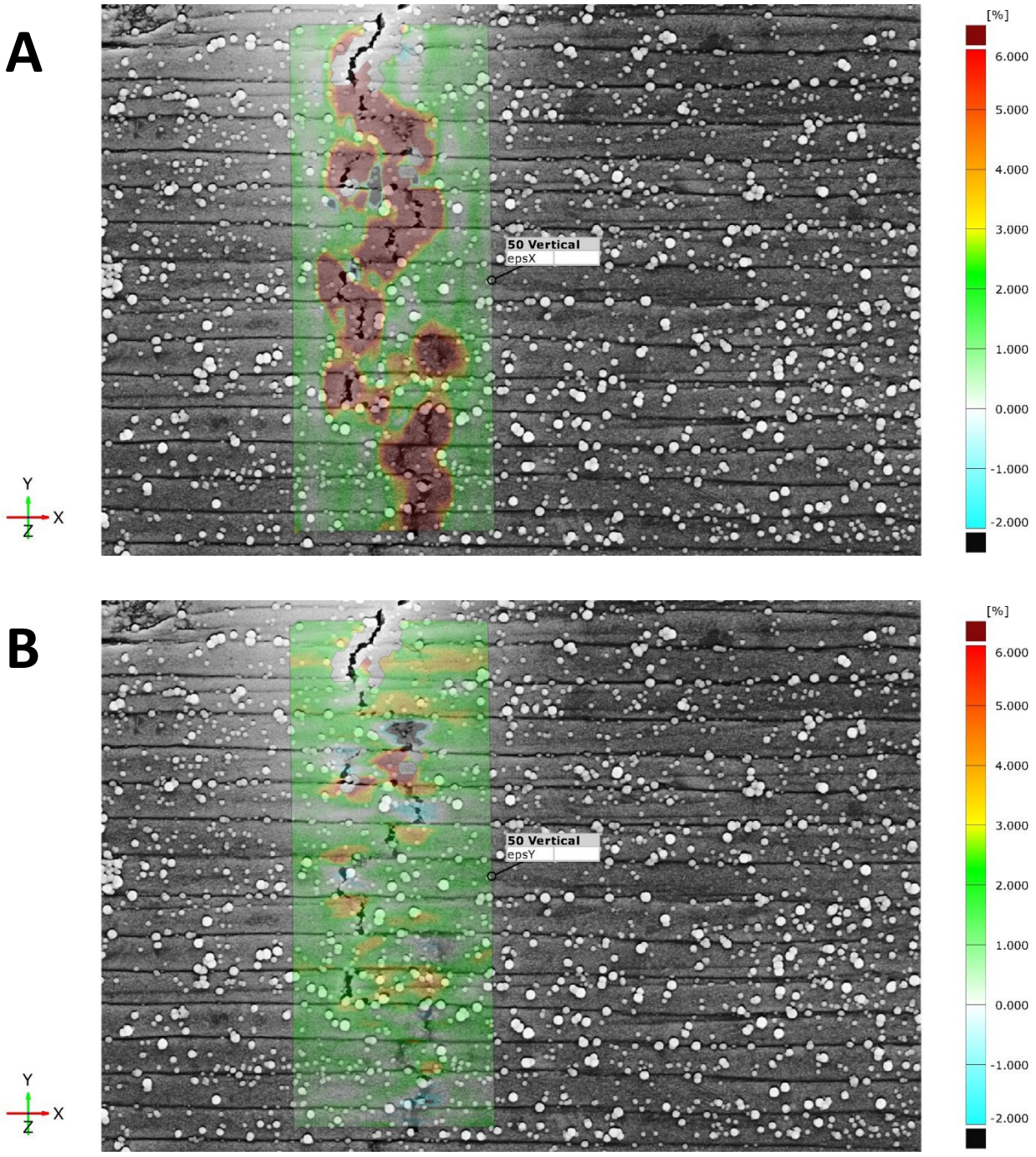

Figure 61: Images of DIC being performed on captured SEM images of the nacre architecture upon reversing the actuation to 220 microns. DIC strains are presented for both the (A) x-direction and (B) y-direction.

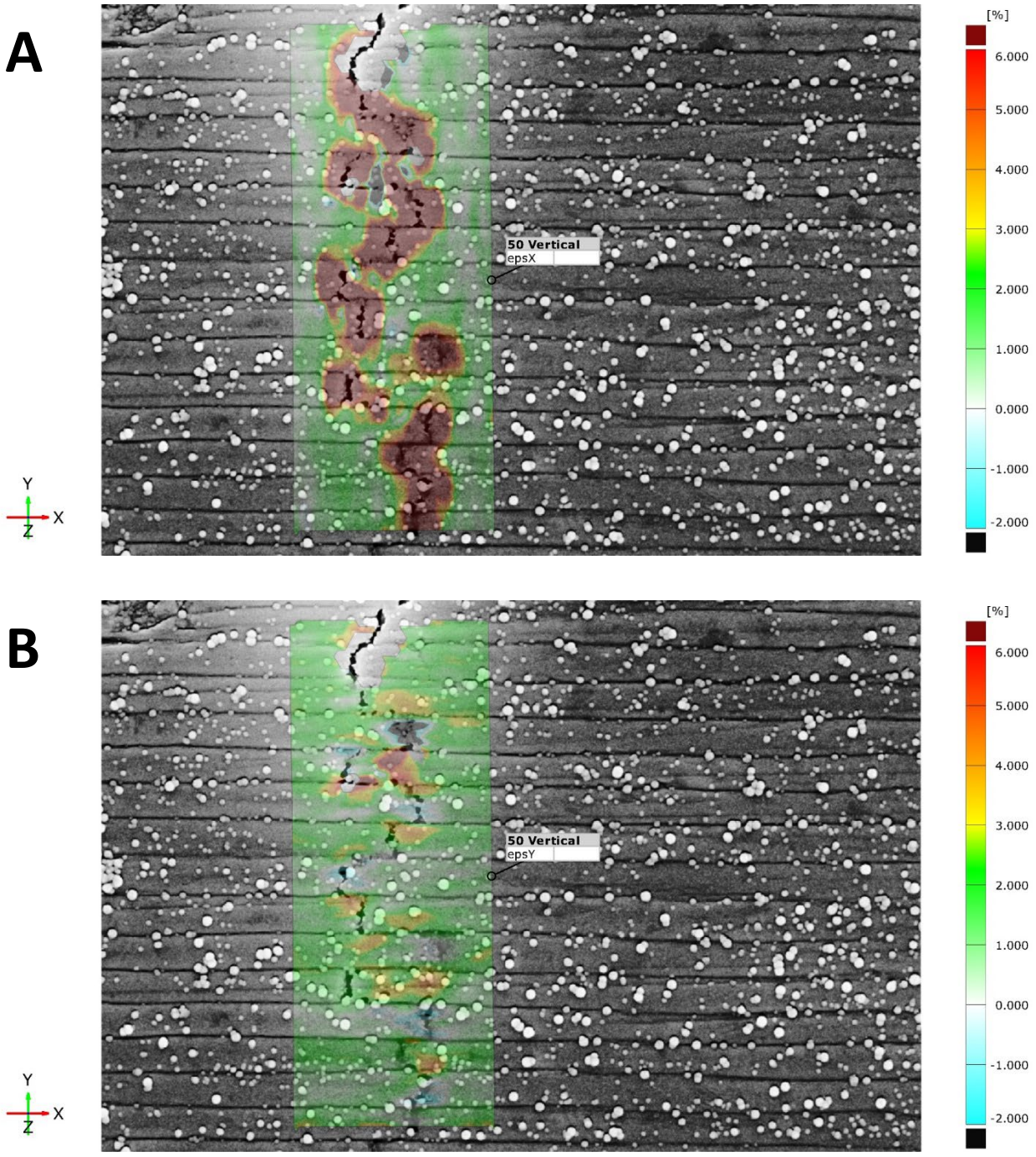

Figure 62: Images of DIC being performed on captured SEM images of the nacre architecture upon reversing the actuation to 200 microns. DIC strains are presented for both the (A) x-direction and (B) y-direction.

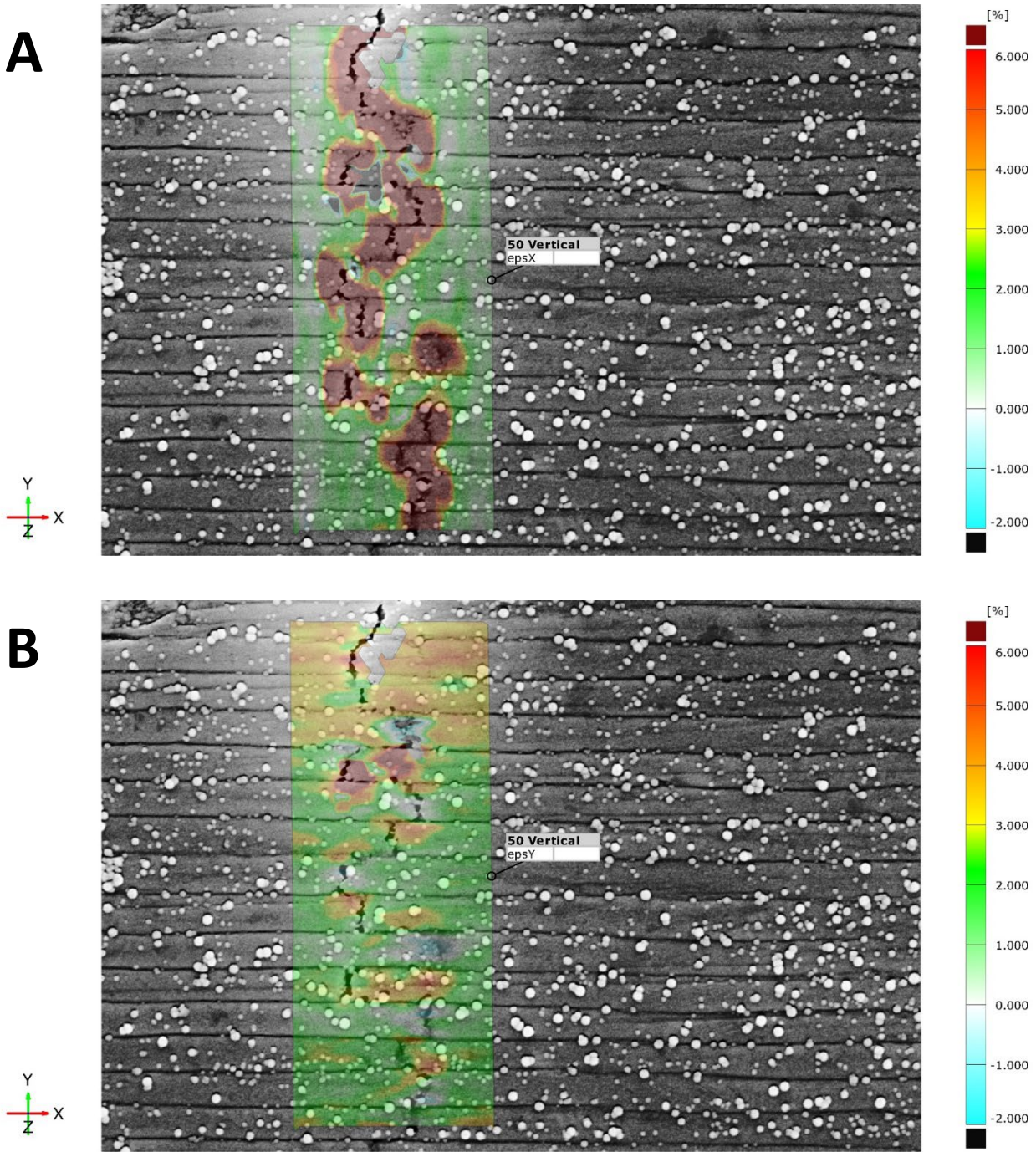

Figure 63: Images of DIC being performed on captured SEM images of the nacre architecture upon reversing the actuation to 180 microns. DIC strains are presented for both the (A) x-direction and (B) y-direction.

As the actuation is reversed further to 160 microns (**Figure 64**), the nacre architecture continues to undergo the reversible sliding mechanism. The strain in the y-direction (**Figure 64 B**) can be seen relaxing from the previous stage, with the bands of strain reducing in the intensity of the color. The strain in the x-direction can also be seen responding to this reversal in actuation. As seen in **Figure 64 A**, the areas around the tablet gaps that are predominated by the dark red color have begun to shrink ever so slightly. The brightness in the tablet gaps has almost completely dissipated at this point, leaving only small, isolated pockets of missing data in the surface component calculations. Upon reversing the actuation to 140 microns (**Figure 65**), the strains in both the x-direction and y-direction appear to be holding steady with minimal changes in the calculated strains for the surface component at this stage of actuation. However, once the actuation was reversed further to 120 microns, the strains can now be seen responding to the reversal in a big way (**Figure 66**). In the y-direction (**Figure 66 B**), the strain in the upper portion of the surface component can be seen undergoing a relaxation, while the strain band in the lower third of the surface component can be seen intensifying. So, while the upper portion is likely at the stage where the nanoasperities have fully passed one another, the lower portion is in a build-up stage where the nanoasperities are attempting to pass one another. As for the x-direction (**Figure 66 A**), the areas of concentrated high strain around the sights of the tablet gaps can be seen receding as the gaps continue to reversibly slide.

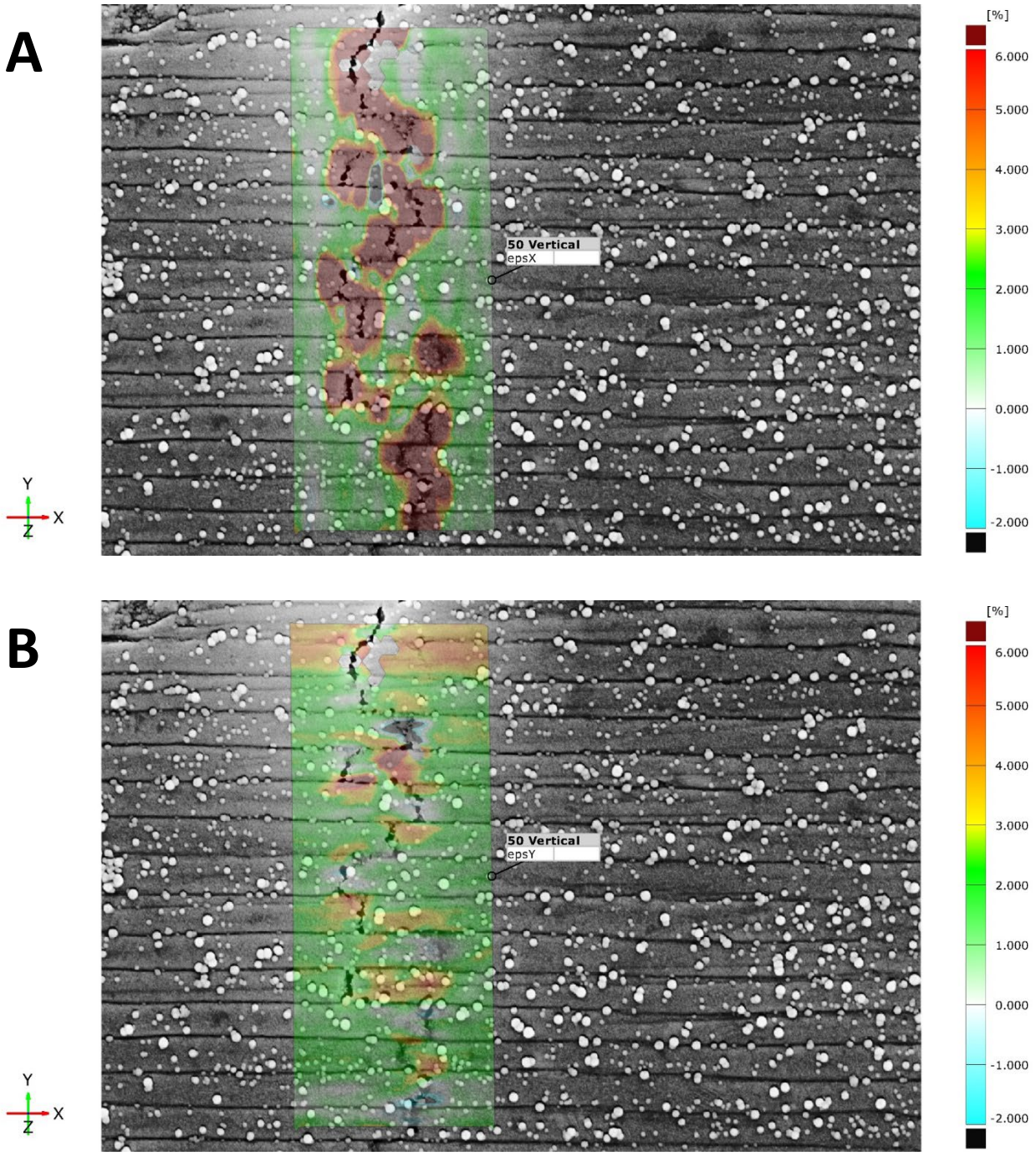

Figure 64: Images of DIC being performed on captured SEM images of the nacre architecture upon reversing the actuation to 160 microns. DIC strains are presented for both the (A) x-direction and (B) y-direction.

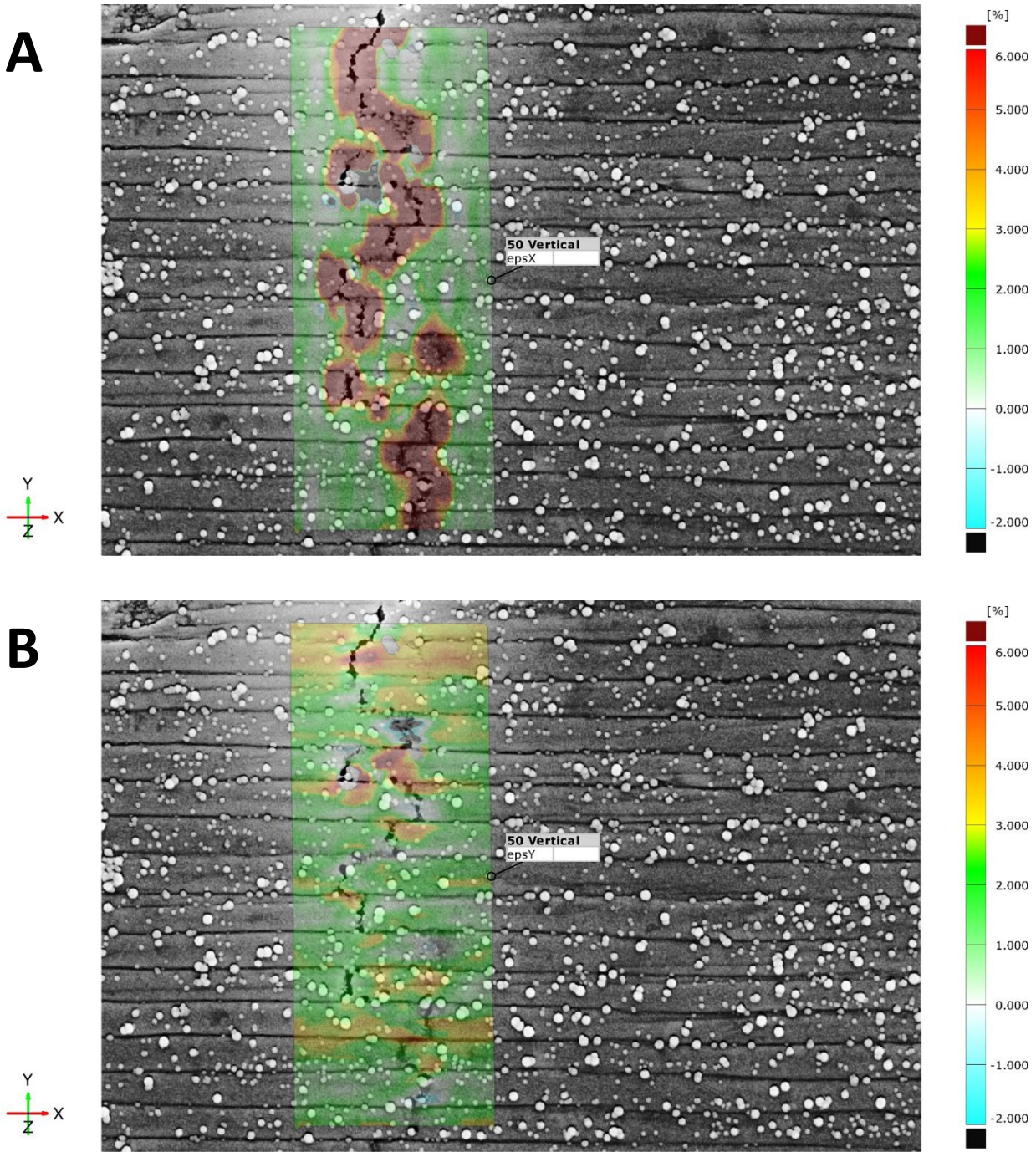

Figure 65: Images of DIC being performed on captured SEM images of the nacre architecture upon reversing the actuation to 140 microns. DIC strains are presented for both the (A) x-direction and (B) y-direction.

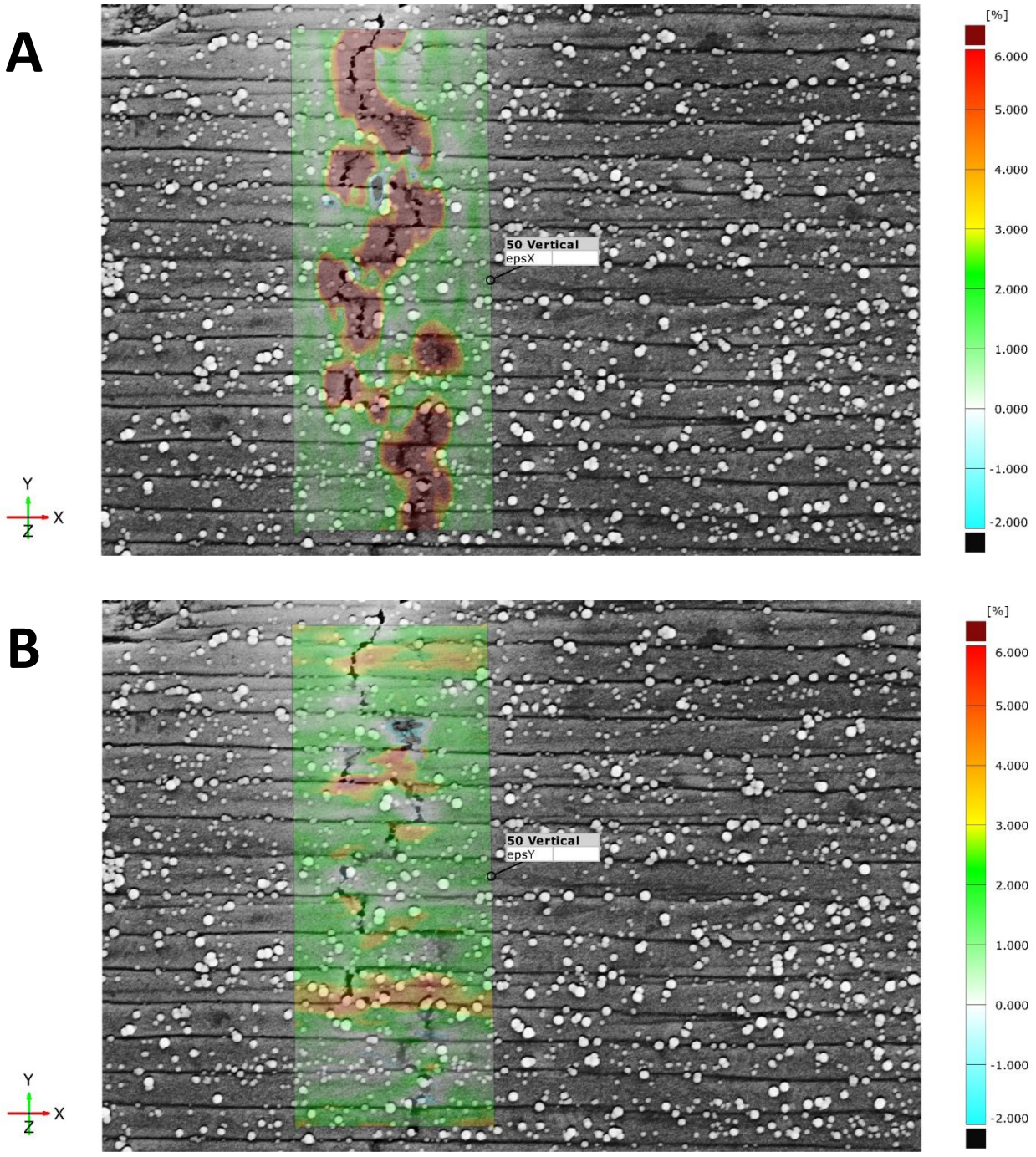

Figure 66: Images of DIC being performed on captured SEM images of the nacre architecture upon reversing the actuation to 120 microns. DIC strains are presented for both the (A) x-direction and (B) y-direction.

Furthering the reversal of the actuation to 100 microns (**Figure 67**), the strain in the y-direction undergoes a "trading places" scenario, where the strain in the upper portion of the nacre architecture is now seen intensifying, while the strain in the lower portion undergoes a relaxation (**Figure 67 B**). The tablets continue to reversibly slide here as well, which causes the area of concentrated strain in the x-direction around the tablet gaps to further recede (**Figure 67 A**). This trend continues when the actuation is reversed to 80 microns (**Figure 68**), the strain in the y-direction in the lower portion of the surface component increases, while the strain in the upper portion of the sample decreases (**Figure 68 B**). The strain in the x-direction is further reduced as the area of dominant strain around the tablet gaps further recedes (**Figure 68 A**). Upon reversing the actuation to 60 microns (**Figure 69**) the degree to which the reversible sliding mechanism has affected the strain in the nacre architecture caused by the bending experiment. The strain in the x-direction has now significantly reduced with the area of high concentrated strain around the tablet gaps now occupying a significantly smaller space (**Figure 69 A**). The strain in the y-direction has also relaxed quite significantly, with most of the locations of concentrated strain appearing to have been reduced.

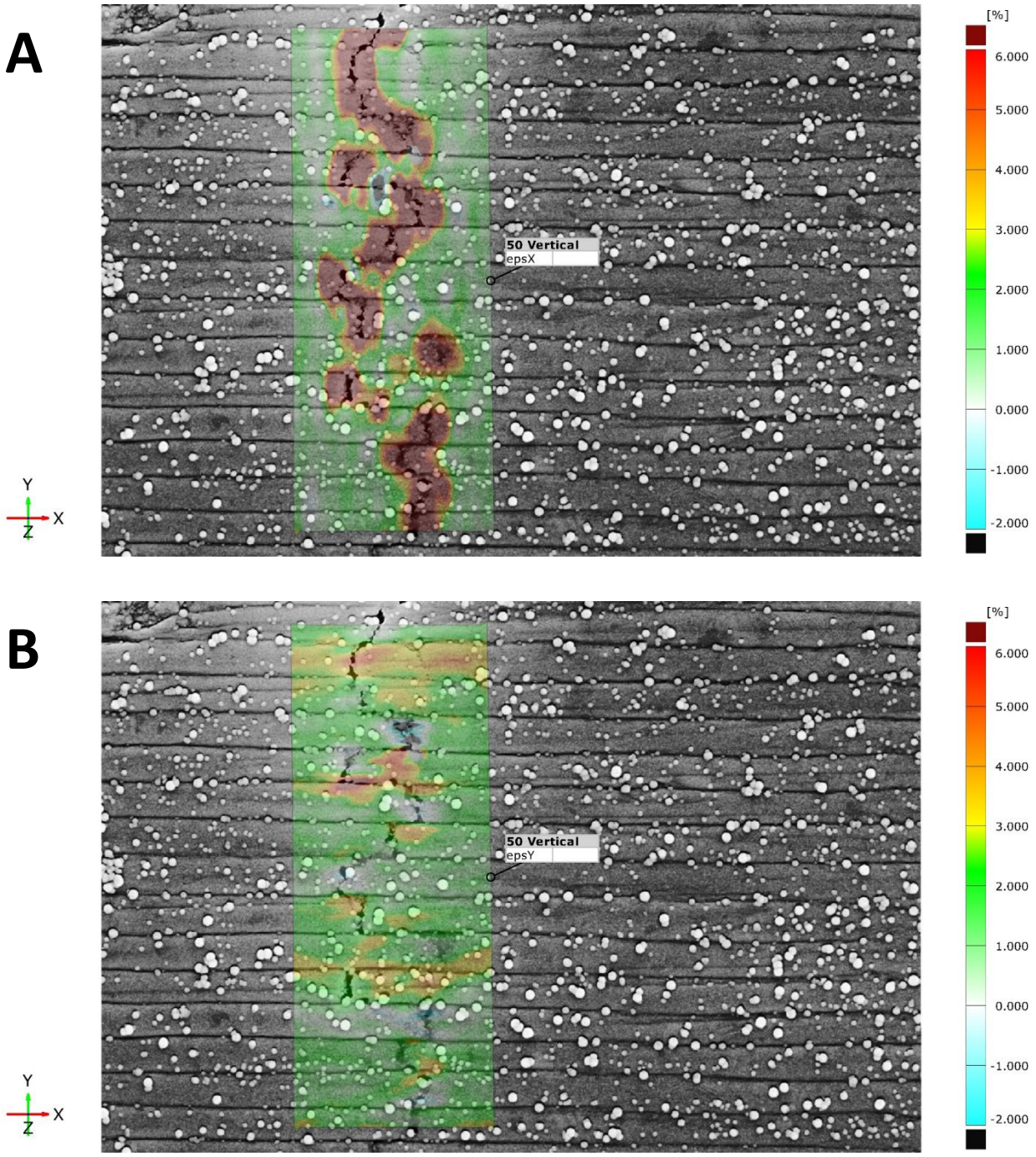

Figure 67: Images of DIC being performed on captured SEM images of the nacre architecture upon reversing the actuation to 100 microns. DIC strains are presented for both the (A) x-direction and (B) y-direction.

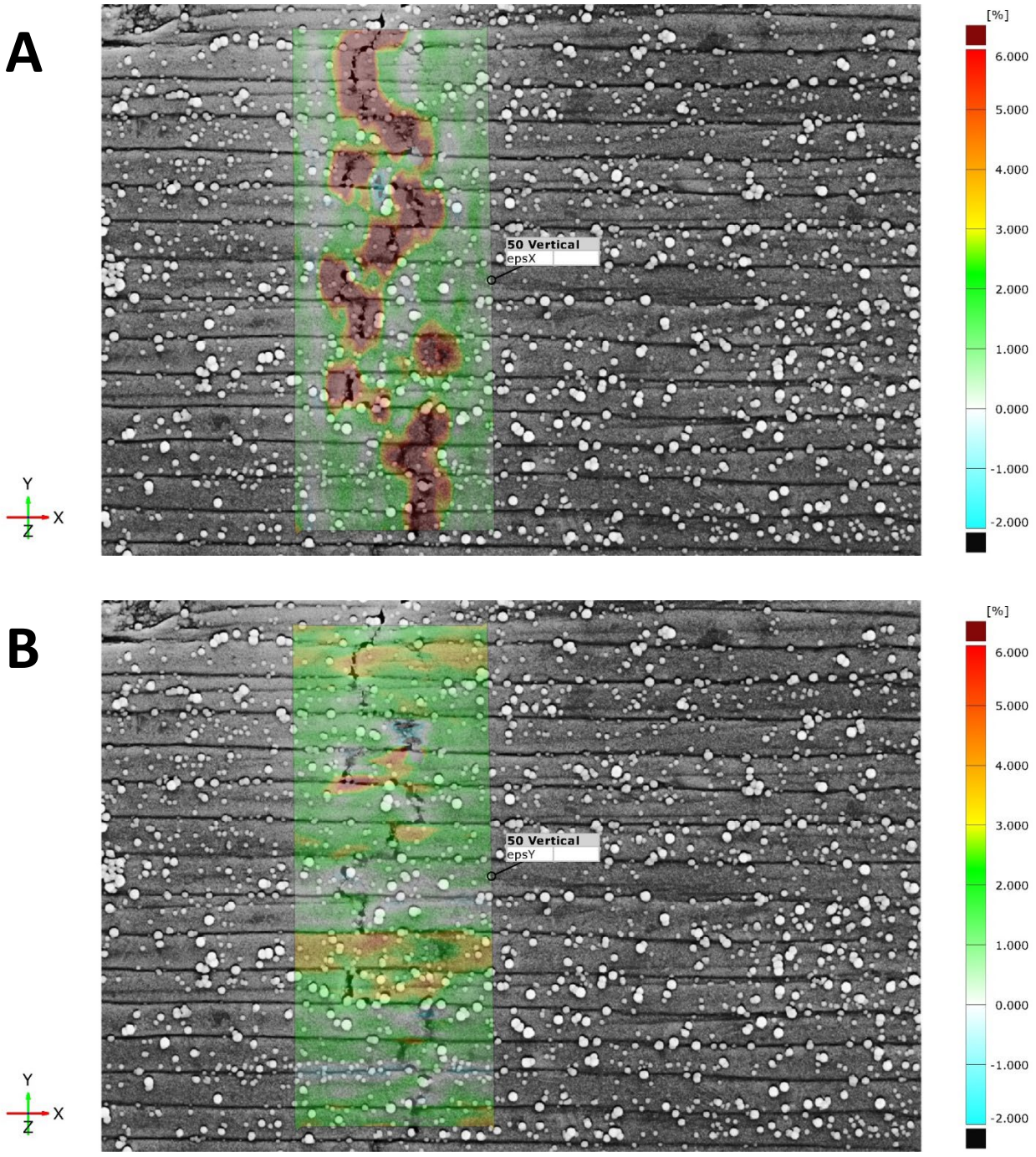

Figure 68: Images of DIC being performed on captured SEM images of the nacre architecture upon reversing the actuation to 80 microns. DIC strains are presented for both the (A) x-direction and (B) y-direction.

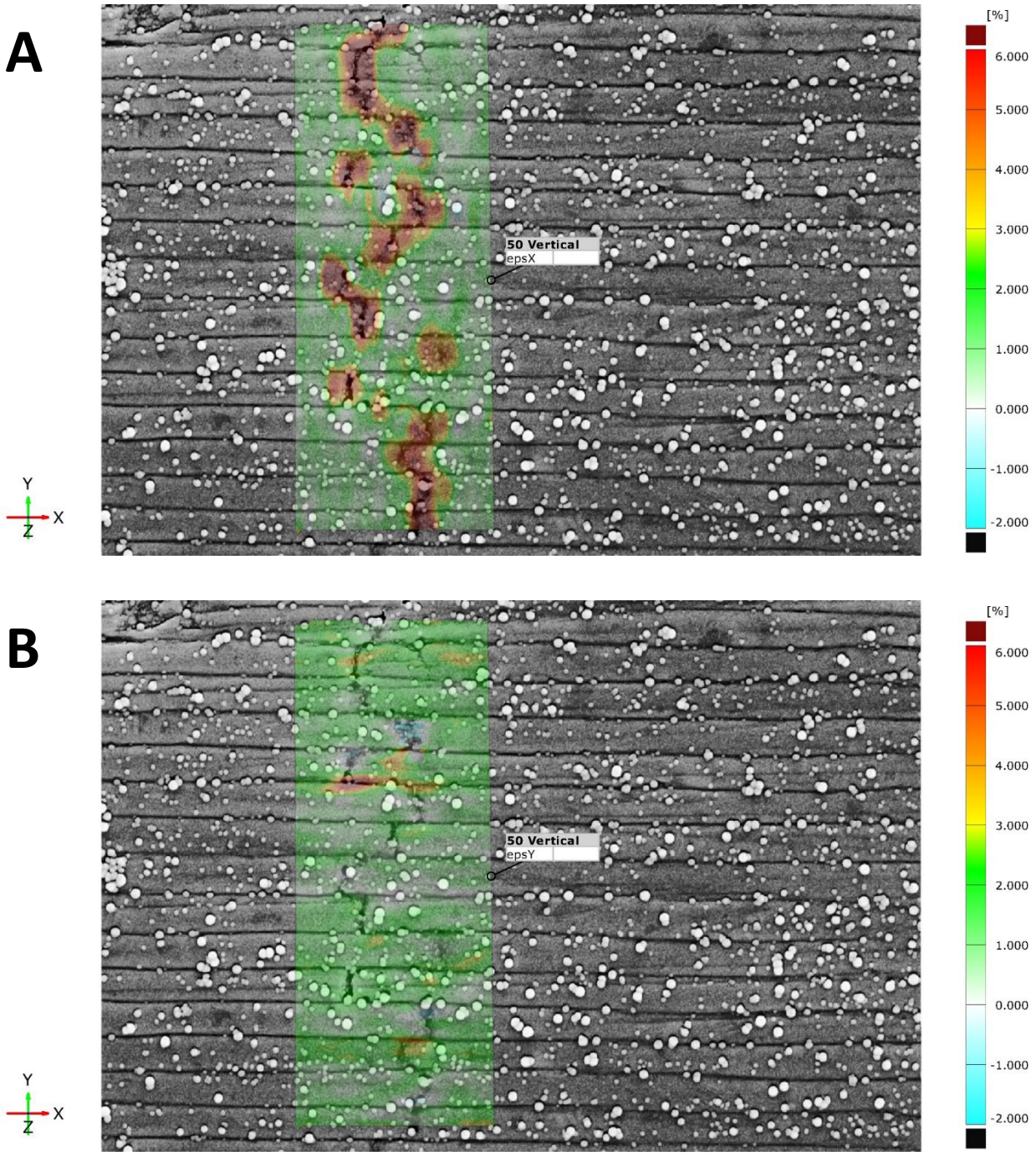

Figure 69: Images of DIC being performed on captured SEM images of the nacre architecture upon reversing the actuation to 60 microns. DIC strains are presented for both the (A) x-direction and (B) y-direction.

The strain in the nacre architecture continues to evolve after further reversing the actuation to 40 microns (**Figure 70**). Upon reaching the 40-micron stage of reversal the strain in the y-direction can be seen almost completely returning to its initial state in most areas (**Figure 70 B**). The areas of concentrated strain in the x-direction that are around the tablet gaps is also seen further receding as the reversible sliding mechanism continues to pull the tablets back together and close the gaps that were formed between them (**Figure 70 A**). When the actuation is reversed to 20 microns (**Figure 71**), the nacre architecture responds to the reversible sliding mechanism in an interesting way. After reaching this point in the reversible mechanism, the gaps between the tablets have now come very close to completely closing. The areas of high amounts of concentrated strain in the x-direction around the tablet gaps has receded extensively (**Figure 71 A**). The strain in the y-direction here however has undergone a sudden increase (**Figure 71 B**). The same areas around the horizontal tablet interfaces, where the strain in the y-direction had increased during the forward actuation, are now experiencing similar levels of strain. This increase in strain in the y-direction is indicative of the nanoasparities again coming in contact with one another, causing the tablets to have to overcome this mechanism once again before fully coming back together. Once the actuation has been returned to the point of initial contact, the results of the reversible sliding mechanism come fully into view (**Figure 72**). At this point, the gaps between the tablets have fully closed and the separations can no longer be measured. However, the surface component still shows residual strains for both the x-direction and the y-direction.

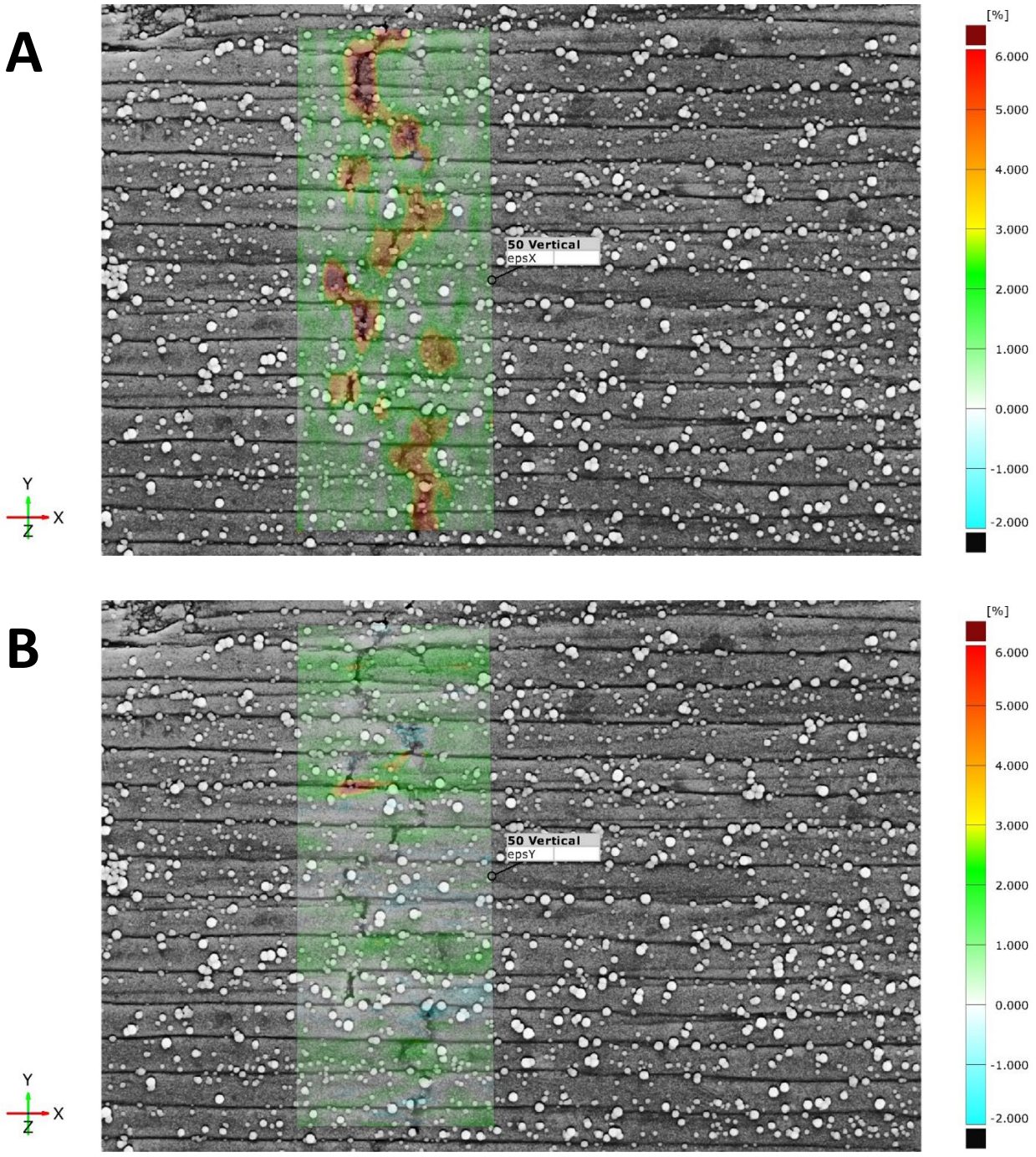

Figure 70: Images of DIC being performed on captured SEM images of the nacre architecture upon reversing the actuation to 40 microns. DIC strains are presented for both the (A) x-direction and (B) y-direction.

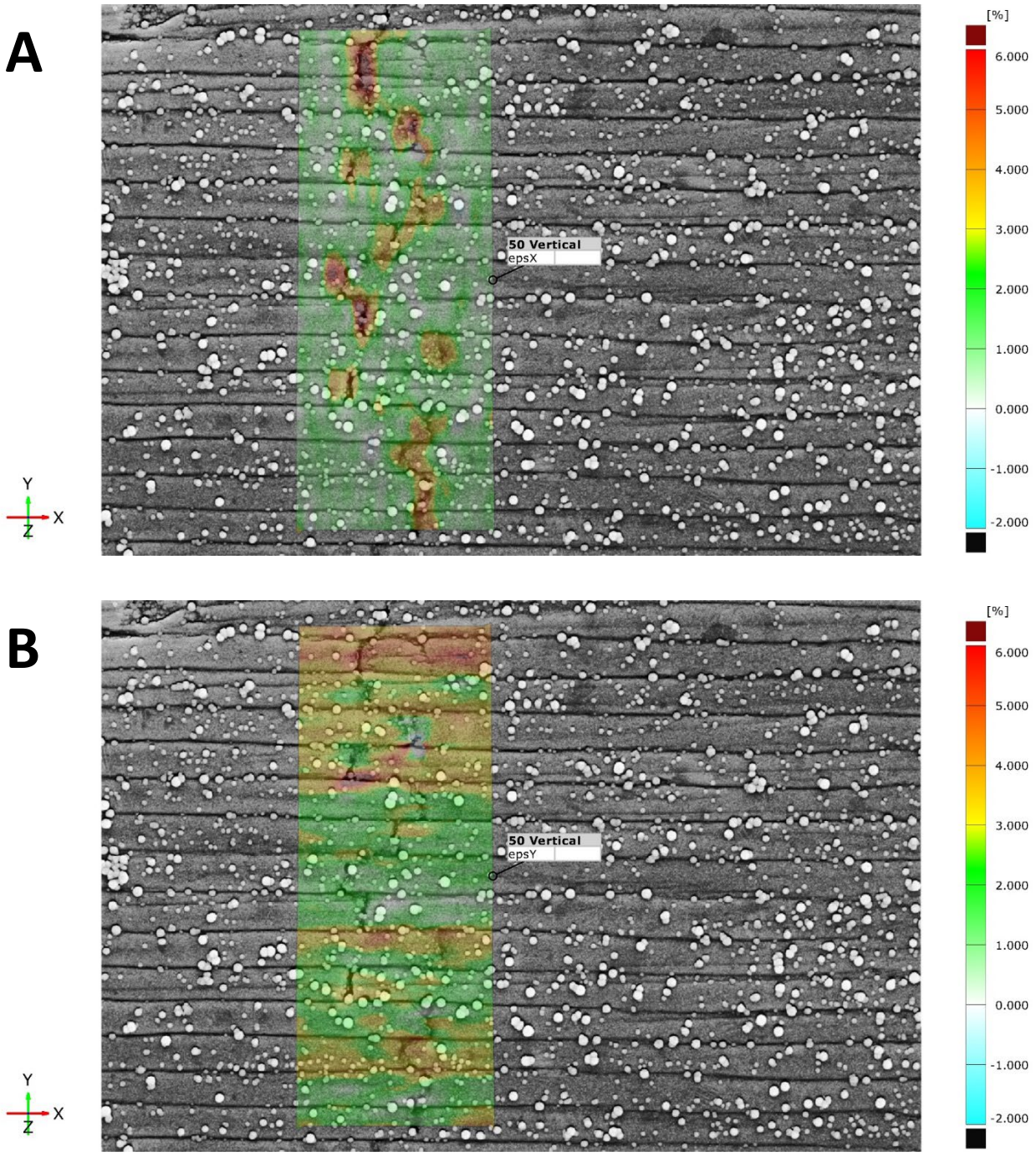

Figure 71: Images of DIC being performed on captured SEM images of the nacre architecture upon reversing the actuation to 20 microns. DIC strains are presented for both the (A) x-direction and (B) y-direction.

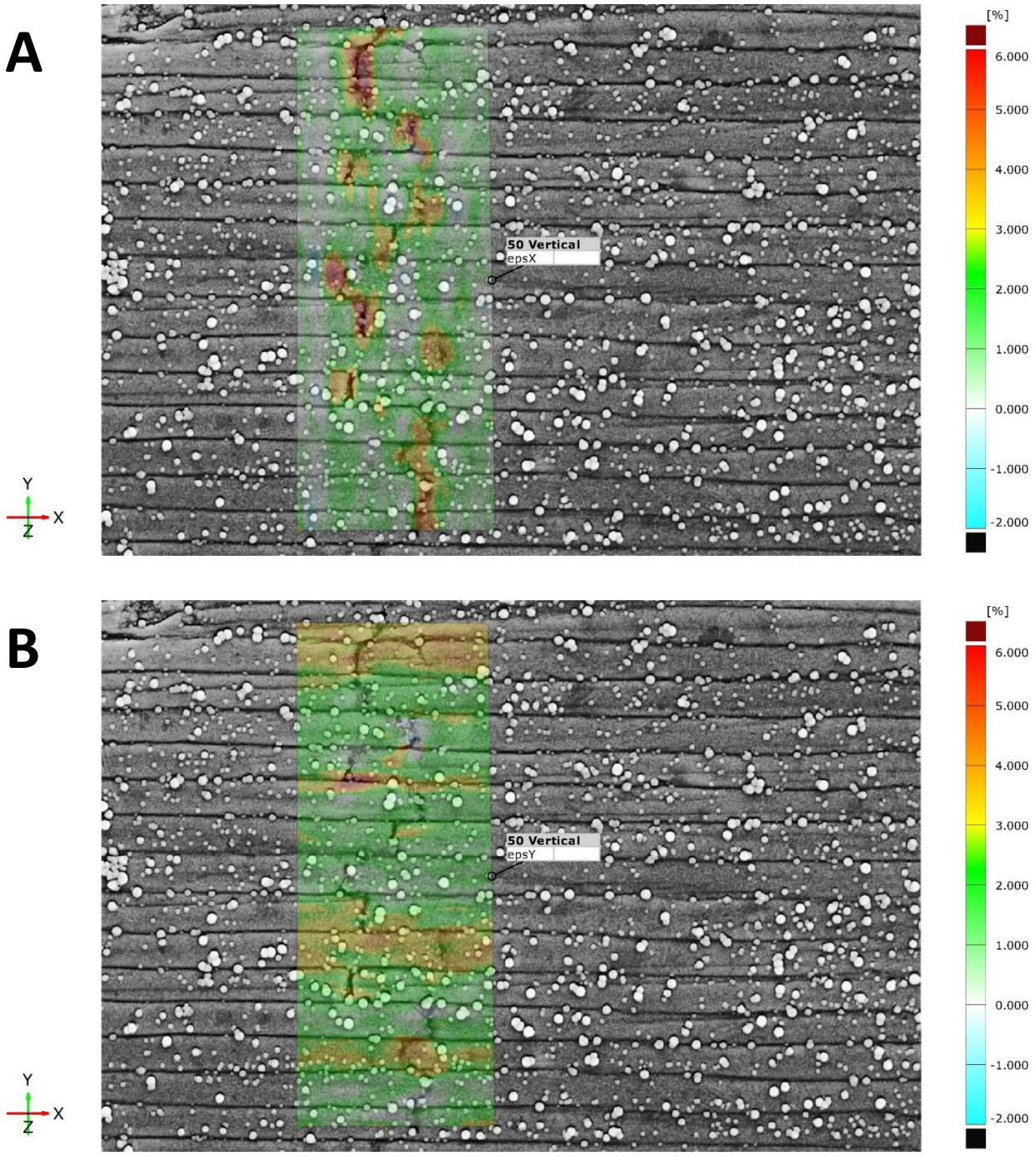

Figure 72: Images of DIC being performed on captured SEM images of the nacre architecture upon fully reversing the actuation that was applied. DIC strains are presented for both the (A) x-direction and (B) y-direction.

This residual strain in the abalone nacre architecture is indicative of a remodeling process that the tablet interfaces undergo as they reversibly slide back together. As the tablets slide apart from each other, the interactions between the nanoasperities on the surface of the tablets, the breaking of the mineral bridges, and in general the surface-to-surface contact between the tablets that are sliding causes nanoscale debris to accumulate both inside the tablet gaps as well as along the horizontal interfaces between the tablets. This accumulation of debris causes prevents the tablet interfaces from reforming in precisely the same manner as they had initially formed prior to the bending process. This remodeling process is likely the cause of the residual strain remaining in the nacre architecture even after the gaps between the tablets have completely closed and the reversible sliding mechanism is complete.

While the visual representation of the strains applied to the nacre architecture undergoing three-point bending deformation process is beneficial in understanding how the tablet structure responds to the applied bending, GOM Correlate provides a method of determining the strain applied to a specific area within the applied surface component. The GOM Correlate software provides a tool called deviation labels, with which a more precise measurement of the strain on the local level can be evaluated. Applying the deviation labels to specific parts of a surface component allow the strain at the selected point to be tracked through the various stages of deformation from image to image. These deviation labels could then be used to track the strain for each of the tablet gaps in the image from the initial undeformed state, through to maximum applied strain and all the way back down through the reversal process.

4.4.4 Analyzing Local Strains Derived from Digital Image Correlation

As previously stated, in order to further explore the sliding mechanism occurring in this area, a more focused measurement of the local strains was performed by applying deviation labels to the surface component that was applied to the images of the sample surface, as seen in **Figure 73**. A deviation label was placed on the surface component at tablet gap (or as near as possible) for each of the imaged tablet pairings. The strains in the x-direction for each of these tablet pairs was read and recorded for each of the successive stages of actuation. Then, the SEM images of these stages were analyzed using ImageJ as in previous experiments, in order to measure the tablet gap formed during both the forward and reverse actuation process. These measurements were then recorded to compare the measured tablet gaps at each tablet pair for each individual stage of actuation with the subsequent measured strain for said tablet pair.

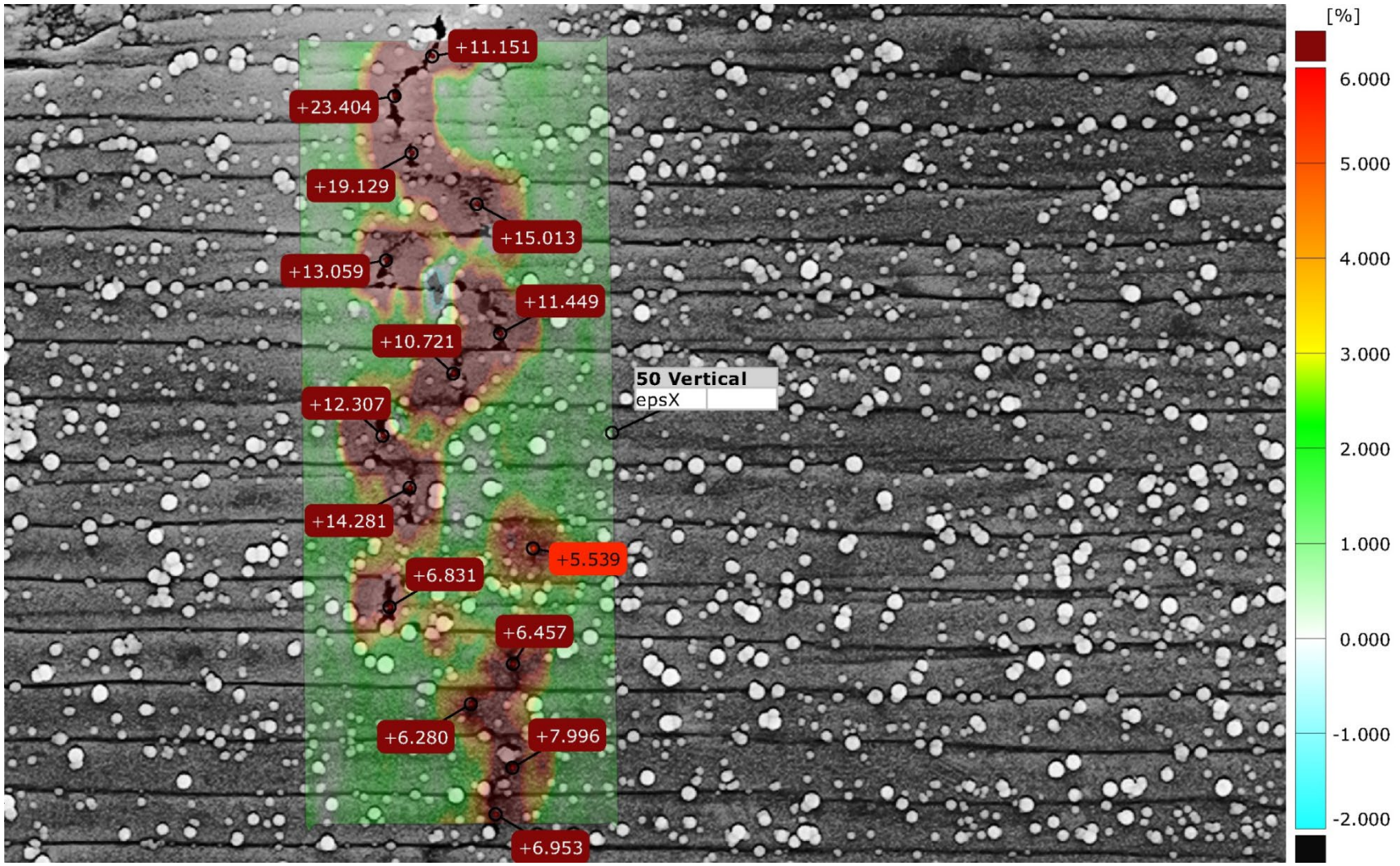

Figure 73: An image of nacre sample with an applied speckle pattern undergoing digital image correlation. The surface component has a set of deviation labels applied to the sample to get a precise measurement of the strain in the x-direction at the point at which the tablet gaps form.

After measurements of both the tablet gaps formed and the strains associated with those tablet gaps were recorded, a scatter plot of the strains against the tablet gaps was generated and displayed in **Figure 74**. The scatter plot was used to generate a line of best fit to model the relationship between the measured tablet gap and the strain on the local level generated by said tablet gap. The equation (**Equation 3**) for this line can be seen on the graph in **Figure 74**. Using this equation, an estimate of the local strain needed to overcome the reversible sliding mechanism by fracturing the biopolymer was made using the tablet gaps measured from the previous experiment shown in **Figure 20**, using the tablet gaps formed at the peak actuation of 300 microns during the three-point bending. The tablets that were the point of focus for this calculation were the last tablet to not recover the gap formed and the first tablet to fully recover its gap, highlighted in **Figure 21**. The gaps measured for these tablets were 169 nm and 132 nm respectively. **Equation 3** was then used to calculate what the local strains were at the point at which the biopolymer was fractured, and the tablet pair could no longer fully recover the gap formed between them. The estimated local strain calculated at this degree of tablet gap formation was found to be 54.28% and 42.66%, respectively. This 42.66% local strain is much greater than that of the 0.502% global strain that was calculated previously using the geometric equations for a bending beam, which shows that on a local level, the tablet sliding mechanism allows the nacre architecture to absorb a large amount of energy through the separation of the tablets and the formation of gaps that it can then recover, provided the biopolymer necessary for the reversible sliding mechanism has not been fractured.

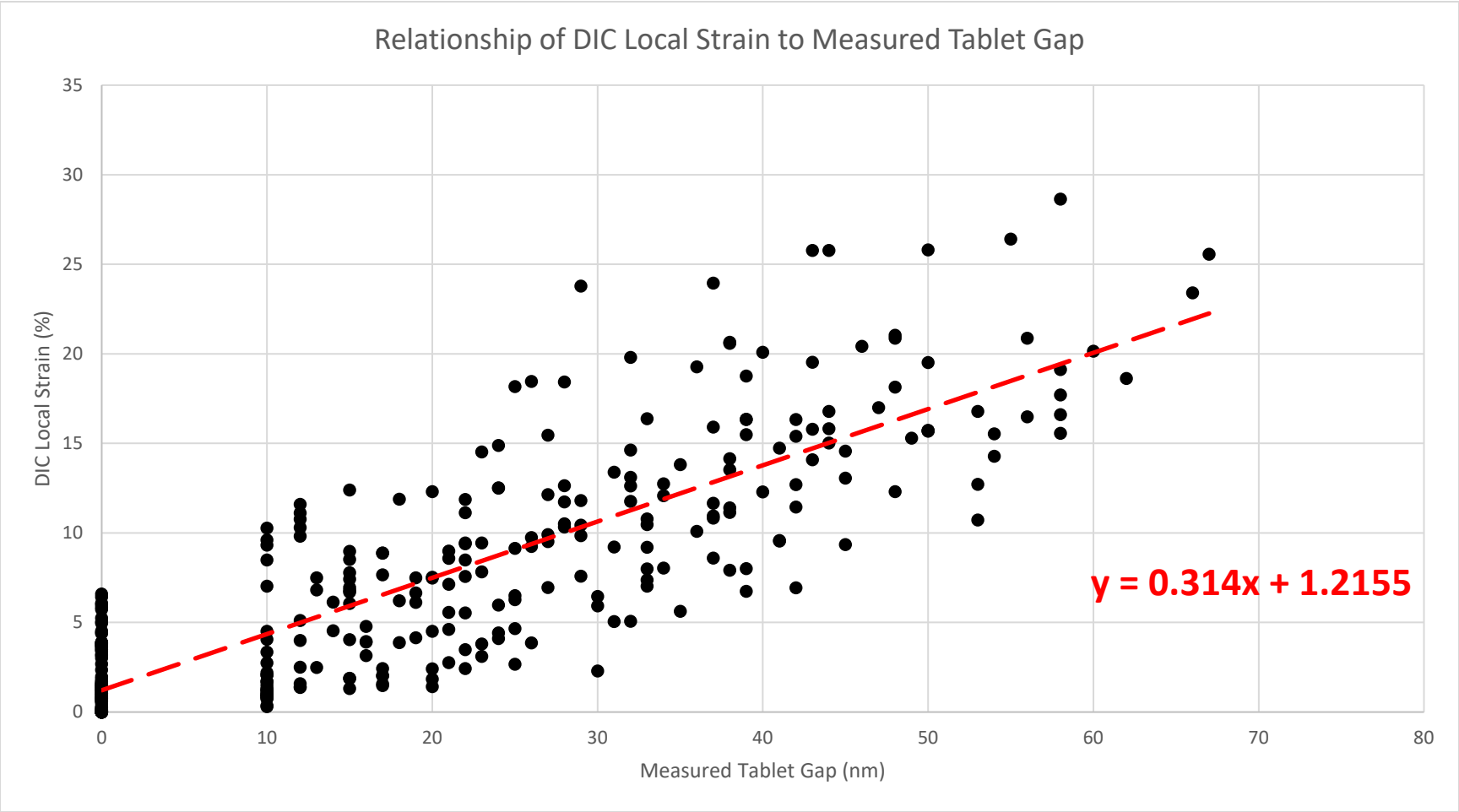

Figure 74: Graphical representation of the data obtained in the digital image correlation experiment. A comparison of the calculated strains and measured tablet gaps is made into a scatter plot, and a line of best fit trendline is generated. The equation for this line is presented on the graph.

5. Future Work

The research included in this dissertation is expected to advance the knowledge of the unique architecture of the nacre structure. In the reversible tablet sliding experiments, an estimate of the strain at which the biopolymer fractures, and the reversible sliding mechanism can no longer occur. The characterization of the widescale reversible sliding mechanism will aid in advancing the knowledge of the field as well as assist in the design of materials that are based off of the nacre structure. However, more work may still be performed in order to aid in advancing the knowledge of the nacre structure.

While in these experiments, the strains related to the widescale reversible sliding mechanism were explored, the associated stress of this mechanism was not evaluated. The relationship between stress and strain is important to understanding the widescale reversible sliding mechanism on a deeper level, especially on the local level. Due to the cost-effective nature of the testing apparatus, stress could not be measured through this testing method. The knowledge of the stresses being applied to the nacre architecture during the reversible sliding mechanism is important is important for understanding the mechanism to its fullest extent.

One other aspect that needs to be explored further is the reversible tablet sliding deformation mechanism's effect on the entire nacre structure. With the previous testing of the nacre architecture, observations of the tablet sliding were mere made on the outer free surface of the nacre beam. Here we see tablets sliding apart from one another, but little is known of how these mechanisms behave within the nacre structure as a whole. One testing method that may assist in providing this information is nano x-ray computed tomography (Nano- X-Ray CT).

In nano-CT, much like regular x-ray CT, an x-ray beam is focused on the surface of a sample from different angles, thus generating a series of 2D x-ray images. These images are processed to generate a 3D model of the structure. This method has been used on concrete in a micro-CT to test the effects of the deformation process on the internal microstructure of the solid. The team was able to track the formation of microcracks in a concrete beam during a three-point bending experiment [46]. Use of this method in a nano-CT may allow us to further understand the deformation mechanism as well as the recovery mechanism in the nacre tablet structure.

The nacre architecture is an incredibly unique structure, and its fascinating properties are the reason why so much research has been produced with the express goal of furthering the knowledge and understanding of how this material functions. However, there are still many more secrets yet to be revealed, but with the ever expanding research being performed these secrets come closer to the light.

References

[1] Thorkelsson, K., Bai, P., & Xu, T. (2015). Self-assembly and applications of anisotropic nanomaterials: A review. *Nano Today*, *10*(1), 48–66.

[2] Xu, Z., Lu, D., Ma, L., Lu, C., Xi, X., Zhang, G., … Wu, D. (2019). Hierarchically ordered carbon tube-sheet superstructure via template-directed self-assembly of polyimide. *Chemical Engineering Journal*, *364*, 201–207.

[3] Byun, M., Park, T. W., & Park, W. I. (2020). Hierarchically ordered hybrid nanostructures via spontaneous self-assembly of block copolymer blends. *Thin Solid Films*, *701*, 137928.

[4] Xia, D.-H., Pan, C., Qin, Z., Fan, B., Song, S., Jin, W., & Hu, W. (2020). Covalent surface modification of LY12 aluminum alloy surface by self-assembly dodecyl phosphate film towards corrosion protection. *Progress in Organic Coatings*, *143*, 105638.

[5] Ong, W.-J., Tan, L.-L., Chai, S.-P., Yong, S.-T., & Mohamed, A. R. (2015). Surface charge modification via protonation of graphitic carbon nitride (g-C3N4) for electrostatic self-assembly construction of 2D/2D reduced graphene oxide (rGO)/g-C3N4 nanostructures toward enhanced photocatalytic reduction of carbon dioxide to methane. *Nano Energy*, *13*, 757–770.

[6] Ge, D., Li, Y., Yang, L., Fan, Z., Liu, C., & Zhang, X. (2011). Improved self-assembly through UV/ozone surface-modification of colloidal spheres. *Thin Solid Films*, *519*(15), 5203–5207.

[7] Novikau, I. S., Sánchez, P. A., & Kantorovich, S. S. (2020). The influence of an applied magnetic field on the self-assembly of magnetic nanogels. *Journal of Molecular Liquids*, 112902.

[8] Xu, H., Zhang, C., Yao, J., Pang, S., Zhou, X., & Cui, G. (2018). Graphene-wrapped iron carbide nanoparticles as Pt-free counter electrode towards dye-sensitized solar cells via magnetic field induced self-assembly. *Journal of Photochemistry and Photobiology A: Chemistry*, *355*, 48–54.

[9] Li, Z., Wang, J., Li, Y., Liu, X., & Yuan, Q. (2018). Self-assembled DNA nanomaterials with highly programmed structures and functions. *Materials Chemistry Frontiers*, *2*(3), 423–436.

[10] Ma, K., Harris, A. W., & Cha, J. N. (2018). DNA assembled photoactive systems. *Current Opinion in Colloid & Interface Science*, *38*, 18–29.

[11] Li, H., Carter, J. D., & Labean, T. H. (2009). Nanofabrication by DNA self-assembly. *Materials Today*, *12*(5), 24–32.

[12] Nudelman, F. (2015). Nacre biomineralisation: A review on the mechanisms of crystal nucleation. *Seminars in Cell & Developmental Biology*, *46*, 2–10.

[13] Cartwright, J. H., & Checa, A. G. (2006). The dynamics of nacre self-assembly. *Journal of The Royal Society Interface*, *4*(14), 491–504.

[14] Sun, J., & Bhushan, B. (2012). Hierarchical structure and mechanical properties of nacre: a review. *RSC Advances*, *2*(20), 7617. doi: 10.1039/c2ra20218b

[15] Chen, K., Ding, J., Li, L., Shang, G., Yue, Y., & Guo, L. (2019). Amorphous Alumina Nanosheets/Polylactic Acid Artificial Nacre. *Matter*, *1*(5), 1385–1398.

[16] Evers, K., Porwal, H., Todd, R. I., & Grobert, N. (2019). MWCNT-coated alumina micro-platelets for nacre-like biomimetic composites. *Carbon*, *145*, 586–595.

[17] Falini, G., Albeck, S., Weiner, S., & Addadi, L. (1996). Control of Aragonite or Calcite Polymorphism by Mollusk Shell Macromolecules. *Science*, *271*(5245), 67–69.

[18] Heinemann, F., Launspach, M., Gries, K., & Fritz, M. (2011). Gastropod nacre: Structure, properties and growth — Biological, chemical and physical basics. *Biophysical Chemistry*, *153*(2-3), 126–153.

[19] Barthelat, F., & Espinosa, H. D. (2007). An Experimental Investigation of Deformation and Fracture of Nacre–Mother of Pearl. *Experimental Mechanics*, *47*(3), 311–324.

[20] Gilbert, P. U. P. A., Metzler, R. A., Zhou, D., Scholl, A., Doran, A., Young, A., … Coppersmith, S. N. (2008). Gradual Ordering in Red Abalone Nacre. *Journal of the American Chemical Society*, *130*(51), 17519–17527.

[21] Hou, W., & Feng, Q. (2003). Crystal orientation preference and formation mechanism of nacreous layer in mussel. *Journal of Crystal Growth*, *258*(3-4), 402–408.

[22] Evans, A. G., Suo, Z., Wang, R. Z., Aksay, I. A., He, M. Y., & Hutchinson, J. W. (2001). Model for the robust mechanical behavior of nacre. *Journal of Materials Research*, *16*(9), 2475–2484.

[23] López, M. I., & Meyers, M. A. (2016). The organic interlamellar layer in abalone nacre: Formation and mechanical response. *Materials Science and Engineering: C*, *58*, 7–13.

[24] Kumar, M. N. R. (2000). A review of chitin and chitosan applications. *Reactive and Functional Polymers*, *46*(1), 1–27.

[25] Aksay, I. A., Trau, M., Manne, S., Honma, I., Yao, N., Zhou, L., … Gruner, S. M. (1996). Biomimetic Pathways for Assembling Inorganic Thin Films. *Science*, *273*(5277), 892–898.

[26] Nudelman, F., Gotliv, B. A., Addadi, L., & Weiner, S. (2006). Mollusk shell formation: Mapping the distribution of organic matrix components underlying a single aragonitic tablet in nacre. *Journal of Structural Biology*, *153*(2), 176–187.

[27] Smith, B. L., Schäffer, T. E., Viani, M., Thompson, J. B., Frederick, N. A., Kindt, J., … Hansma, P. K. (1999). Molecular mechanistic origin of the toughness of natural adhesives, fibres and composites. *Nature*, *399*(6738), 761–763.

[28] Fritz, M., Belcher, A. M., Radmacher, M., Walters, D. A., Hansma, P. K., Stucky, G. D., … Mann, S. (1994). Flat pearls from biofabrication of organized composites on inorganic substrates. *Nature*, *371*(6492), 49–51.

[29] Rousseau, M., Lopez, E., Couté, A., Mascarel, G., Smith, D. C., Naslain, R., & Bourrat, X. (2005). Sheet nacre growth mechanism: a Voronoi model. *Journal of Structural Biology*, *149*(2), 149–157.

[30] Metzler, R. A., Abrecht, M., Olabisi, R. M., Ariosa, D., Johnson, C. J., Frazer, B. H., … Gilbert, P. U. P. A. (2007). Architecture of Columnar Nacre, and Implications for Its Formation Mechanism. *Physical Review Letters*, *98*(26).

[31] Currey, J. D., & Taylor, J. D. (1974). The mechanical behaviour of some molluscan hard tissues. Journal of Zoology, 173(3), 395-406.

[32] Mechanical properties of mother of pearl in tension. (1977). *Proceedings of the Royal Society of London. Series B. Biological Sciences*, *196*(1125), 443–463.

[33] Wang, R. Z., Suo, Z., Evans, A. G., Yao, N., & Aksay, I. A. (2001). Deformation mechanisms in nacre. *Journal of Materials Research*, *16*(9), 2485–2493.

[34] The mechanical design of nacre. (1988). *Proceedings of the Royal Society of London. Series B. Biological Sciences*, *234*(1277), 415–440.

[35] Bruet, B., Qi, H., Boyce, M., Panas, R., Tai, K., Frick, L., & Ortiz, C. (2005). Nanoscale Morphology and Indentation of Individual Nacre Tablets from the Gastropod Mollusc Trochus Niloticus. *Journal of Materials Research*, *20*(9), 2400–2419.

[36] Menig, R., Meyers, M., Meyers, M., & Vecchio, K. (2000). Quasi-static and dynamic mechanical response of Haliotis rufescens (abalone) shells. *Acta Materialia*, *48*(9), 2383–2398.

[37] Barthelat, F., Tang, H., Zavattieri, P., Li, C., & Espinosa, H. (2007). On the mechanics of mother-of-pearl: A key feature in the material hierarchical structure. *Journal of the Mechanics and Physics of Solids*, *55*(2), 306–337.

[38] Bonderer, L. J., Studart, A. R., & Gauckler, L. J. (2008). Bioinspired Design and Assembly of Platelet Reinforced Polymer Films. *Science*, *319*(5866), 1069–1073.

[39] Espinosa, H. D., Juster, A. L., Latourte, F. J., Loh, O. Y., Gregoire, D., & Zavattieri, P. D. (2011). Tablet-level origin of toughening in abalone shells and translation to synthetic composite materials. *Nature Communications*, *2*(1).

[40] Barthelat, F., Li, C.-M., Comi, C., & Espinosa, H. D. (2006). Mechanical properties of nacre constituents and their impact on mechanical performance. *Journal of Materials Research*, *21*(8), 1977–1986.

[41] Sumitomo, T., Kakisawa, H., Owaki, Y., & Kagawa, Y. (2008). In situ transmission electron microscopy observation of reversible deformation in nacre organic matrix. *Journal of Materials Research*, *23*(5), 1466–1471.

[42] Espinosa, H. D., Juster, A. L., Latourte, F. J., Loh, O. Y., Gregoire, D., & Zavattieri, P. D. (2011). Tablet-level origin of toughening in abalone shells and translation to synthetic composite materials. *Nature Communications*, *2*(1).

[43] Lin, A. Y.-M., Chen, P.-Y., & Meyers, M. A. (2008). The growth of nacre in the abalone shell. *Acta Biomaterialia*, *4*(1), 131–138.

[44] Berfield, T. A., Patel, J. K., Shimmin, R. G., Braun, P. V., Lambros, J., & Sottos, N. R. (2007). Micro- and Nanoscale Deformation Measurement of Surface and Internal Planes via Digital Image Correlation. *Experimental Mechanics*, *47*(1), 51–62.

[45] Gioacchino, F. D., & Fonseca, J. Q. D. (2012). Plastic Strain Mapping with Sub-micron Resolution Using Digital Image Correlation. *Experimental Mechanics*, *53*(5), 743–754.

[46] Skarżyński, Ł., & Tejchman, J. (2019). Experimental investigations of damage evolution in concrete during bending by continuous micro-CT scanning. Materials Characterization, 154, 40–52.

[47] ZEISS. (2021, June 18). Version (2020 Hotfix5). GOM Correlate. Retrieved from https://www.gom.com/en/products/gom-suite/gom-correlate-pro.

[48] Verho, T., Karppinen, P., Gröschel, A. H., & Ikkala, O. (2017). Imaging inelastic Fracture processes in Biomimetic nanocomposites AND Nacre by LASER speckle for Better Toughness. *Advanced Science, 5*(1), 1700635.

[49] Kammers, A. D., & Daly, S. (2013). Self-assembled nanoparticle surface patterning for improved digital image correlation in a scanning electron microscope. *Experimental Mechanics, 53*(8), 1333-1341.

[50] Mehdikhani, M., Aravand, M., Sabuncuoglu, B., Callens, M. G., Lomov, S. V., & Gorbatikh, L. (2016). Full-field strain measurements at the micro-scale in fiber-reinforced composites using digital image correlation. *Composite Structures, 140*, 192-201.

[51] Trilion Quality Systems. (2020). GOM Correlate Video Tutorial Chapter 3 (2D Evaluation of Surface Components). Retrieved November 16, 2021, from https://www.youtube.com/watch?v=5PICSny2n2g&t=238s.

[52] Speckle pattern application kit - isi-sys. (2019, January 23). Retrieved February 08, 2021, from http://www.isi-sys.com/speckle-pattern-application-kit/

[53] Dong, Y., & Pan, B. (2017). A review of speckle Pattern fabrication and assessment for digital Image Correlation. *Experimental Mechanics, 57*(8), 1161-1181. doi:10.1007/s11340-017-0283-1